

# **Techniques for Improving the Readout Sensitivity of Gravitational Wave Antennae**

by

Nicolás de Mateo Smith-Lefebvre

B.S., California Polytechnic State University, San Luis Obispo (2006)

Submitted to the Department of Physics  
in partial fulfillment of the requirements for the degree of

Doctor of Philosophy in Physics

at the

MASSACHUSETTS INSTITUTE OF TECHNOLOGY

June 2012

© Nicolás de Mateo Smith-Lefebvre, MMXII. All rights reserved.

The author hereby grants to MIT permission to reproduce and  
distribute publicly paper and electronic copies of this thesis document  
in whole or in part.

Author .....  
.....

Department of Physics  
May 11, 2012

Certified by .....  
.....  
Nergis Mavalvala  
Professor of Physics  
Thesis Supervisor

Certified by .....  
.....  
Peter Fritschel  
Senior Research Scientist  
Thesis Co-supervisor

Accepted by .....  
.....  
Krishna Rajagopal  
Professor of Physics  
Associate Department Head for Education



# **Techniques for Improving the Readout Sensitivity of Gravitational Wave Antennae**

by

Nicolás de Mateo Smith-Lefebvre

Submitted to the Department of Physics  
on May 11, 2012, in partial fulfillment of the  
requirements for the degree of  
Doctor of Philosophy in Physics

## **Abstract**

The detection of gravitational waves (GWs) from astrophysical sources shows promise as a new method to probe extremely energetic phenomena and test the strong field limit of the general theory of relativity. The era of the first generation of broadband interferometric GW antennae is now drawing to a close, and the construction of the second generation has begun. The Laser Interferometer Gravitational-wave Observatory (LIGO) in the United States is one component of a worldwide array of sites designed to collectively record and analyze these GW signals. In preparation for the next major phase of operation, named Advanced LIGO, an incremental upgrade and prototyping project known as Enhanced LIGO introduced several upgrades to the initial LIGO detectors. The addition of the output mode cleaner (OMC), a critically coupled optical cavity designed to filter undesired light from the output of the interferometer before the GW signal is sensed on a photodetector, was one of these upgrades.

This work describes several lessons learned as a result of the installation and commissioning of the OMC in Enhanced LIGO. The techniques described in this thesis include the development of a novel OMC alignment system designed to maximally transmit the GW signal in the presence of contamination that would confound a typical automatic alignment system, a design for a remotely controllable automatic mode matching system for the OMC, and prescriptions for reducing the presence of beam jitter noise associated with the OMC. The designs of each of the future GW detectors include the use of an OMC, thus the techniques described in this thesis will be directly applicable to achieving the maximum sensitivity of these detectors.

Thesis Supervisor: Nergis Mavalvala  
Title: Professor of Physics

Thesis Co-supervisor: Peter Fritschel  
Title: Senior Research Scientist



## Acknowledgments

This thesis would not have been possible without the many people in my life that I am lucky to know. I would like to express sincere thanks to my parents, who have supported my dreams and decisions since the beginning; to my advisor, Nergis, for making the interests of her students a priority, and for being a bottomless source of scientific input; to the rest of my thesis committee, John Belcher, Scott Hughes, and Peter Fritschel, for their helpful comments; to my friends and professors at Cal Poly, your influence has shaped me to be the physicist I am today; to Jeff, Kate, and Tobin, for being my brothers and sister in arms through the eLIGO odyssey; to Chris, Thomas, and Tim, for teaching me so much during my early time at MIT; to Sheila, Stephen, and Al Levine, for helping me take on the Part III general exam; to Daniel Sigg, who first introduced me to LIGO, and remains a source of guidance and inspiration; to Sam Waldman, for designing the OMC, and being an invaluable mentor; to Mike Landry and Keita Kawabe, for their leadership during my stay at Hanford; to all the scientists who worked on Enhanced LIGO, for making me feel part of a team, and their immense contributions to the project; to the LIGO Hanford staff, for putting up with me; to Corey (and Gomez and Gunner), for letting me crash, and for the wee dram; to everyone on the `statmechsocial` list, for being a source of friendship in a new and foreign environment; to Phil and Sarah, for making our home a welcome place to be, and for all the beers we've shared; to Aviv, for letting me turn bolts in his lab to procrastinate while writing my thesis; to Leo, for knowing GR (and Mathematica, and L<sup>A</sup>T<sub>E</sub>X) so that I didn't need to; and to Catherine, for filling my days with happiness and teaching me to enjoy life's small pleasures.

LIGO was constructed by the California Institute of Technology and Massachusetts Institute of Technology with funding from the National Science Foundation and operates under cooperative agreement PHY-0757058. This thesis has LIGO Document Number LIGO-P1200052.



# Contents

<b>1</b>	<b>Gravitational waves</b>	<b>15</b>
1.1	Gravity according to Einstein . . . . .	15
1.2	The general theory of relativity in the linearized regime . . . . .	16
1.3	The phase of a pulse of light in the presence of a gravitational wave .	17
1.4	Sources of gravitational waves . . . . .	18
<b>2</b>	<b>Gravitational wave antennae</b>	<b>21</b>
2.1	Experimental efforts to detect gravitational waves . . . . .	21
2.2	Measurement of optical phase . . . . .	22
2.3	Resonant optical cavity . . . . .	23
2.4	Pound-Drever-Hall reflection locking . . . . .	25
2.5	The Michelson interferometer . . . . .	26
2.6	Michelson with arm-cavities . . . . .	29
2.7	Power recycling . . . . .	30
2.8	Sensing and control of a power recycled Michelson interferometer with arm-cavities . . . . .	30
2.9	A static (DC) readout . . . . .	32
<b>3</b>	<b>The output mode cleaner</b>	<b>35</b>
3.1	Motivation for an OMC . . . . .	35
3.2	Optical and mechanical design of the OMC . . . . .	37
3.2.1	Cavity optics . . . . .	38
3.2.2	Sensors and auxiliary optics . . . . .	40

3.2.3	Suspension system . . . . .	42
3.2.4	Mode matching telescope . . . . .	43
3.2.5	Vibration isolation table . . . . .	43
3.3	Characterization of the H1 OMC . . . . .	43
3.3.1	Free spectral range . . . . .	45
3.3.2	Higher order mode spacing . . . . .	46
3.3.3	Cavity finesse . . . . .	47
3.3.4	Cavity losses . . . . .	48
3.3.5	PZT actuator response . . . . .	49
3.4	Optical feedback instability in the OMC . . . . .	50
3.5	OMC performance in Enhanced LIGO and prospects for future interferometers . . . . .	53
<b>4</b>	<b>Vector space model of optical systems</b>	<b>57</b>
4.1	Frequency components of a laser field . . . . .	58
4.2	The modal space . . . . .	60
4.3	The combined vector space . . . . .	63
4.4	Photodetection . . . . .	65
4.5	Vector space model of the output mode cleaner . . . . .	67
<b>5</b>	<b>Optimal alignment sensing of an output mode cleaner</b>	<b>71</b>
5.1	The alignment problem in a mode cleaner cavity . . . . .	72
5.2	“Beacon” alignment sensing . . . . .	75
5.3	Experimental Demonstration of Beacon Alignment Sensing . . . . .	75
5.4	Optimal alignment sensing of the signal sideband field . . . . .	77
5.5	Generalization of optimal signal-sideband alignment to other alignment sensors . . . . .	78
5.6	Optimal beacon performance in Enhanced LIGO . . . . .	78
5.7	Chapter Summary . . . . .	79

<b>6 Output mode cleaner mode matching feedback control</b>	<b>81</b>
6.1 A feedback control system for mode matching . . . . .	82
6.2 Mode matching sensors . . . . .	84
6.3 Mode matching actuators . . . . .	86
6.4 Chapter summary . . . . .	88
<b>7 Techniques for reducing output mode cleaner beam jitter noise</b>	<b>89</b>
7.1 The noise mechanism of beam jitter incident on a high finesse cavity . . . . .	90
7.2 Mechanical resonances of beam steering optics . . . . .	92
7.3 Magnetic field coupling and feed forward subtraction . . . . .	100
7.4 The relationship of alignment control and beam jitter . . . . .	101
7.5 Modification of the relative modal content of the carrier and audio sidebands . . . . .	103
<b>8 Conclusion</b>	<b>105</b>
<b>A Practical calculations using matrices based on the optical vector space model</b>	<b>109</b>
A.1 Collapsing a tensor of several indices into a 2D matrix . . . . .	109
A.2 Avoid decimal arithmetic bugs . . . . .	112
A.3 Define the free space propagator to have no phase rotation for the TEM <sub>00</sub> carrier. . . . .	112
A.4 Units . . . . .	113
A.5 Calculating signal to noise ratios . . . . .	113
<b>B Additional notes</b>	<b>115</b>
B.1 The control vector separation for alignment is the Gouy phase separation	115
B.2 Dither sensing is a measurement of a partial derivative . . . . .	118
B.3 Conventions for the coefficient of amplitude transmission and reflectivity of beamsplitters . . . . .	118
B.4 A resonant cavity as a mode cleaner . . . . .	120
B.5 The second order HOMs . . . . .	121

<b>C Common misconceptions about laser interferometer gravitational-wave antennae</b>	<b>125</b>
C.1 The sensitivity/bandwidth “trade off” . . . . .	125
C.2 Why LIGO has two arms . . . . .	128
C.3 With a DARM offset, is LIGO still a null measurement? . . . . .	128
<b>Abbreviation Glossary</b>	<b>131</b>

# List of Figures

2-1	Diagram of a resonant cavity and control system . . . . .	23
2-2	Diagram of a Michelson interferometer. . . . .	27
2-3	Diagram of a power-recycled Fabry-Perot Michelson interferometer. . . . .	31
3-1	Diagram showing the location of the OMC. . . . .	36
3-2	Photograph of the OMC. . . . .	38
3-3	Diagram of OMC cavity components . . . . .	39
3-4	Close up photograph of the OMC input coupler mirror. . . . .	39
3-5	Photograph of the OMC double pendulum suspension. . . . .	41
3-6	Photograph of a Tip Tilt optic. . . . .	42
3-7	Block diagram of OMC characterization setup. . . . .	44
3-8	Measurement of the OMC transmission profile. . . . .	48
3-9	Measurement of the OMC PZT actuator calibration. . . . .	50
3-10	Measurement of ring-up times of optical instability in the OMC. . . . .	51
3-11	Interferometer readout SNR gain from squeezing as a function of output losses. . . . .	54
4-1	Diagram of a quadrant photodiode . . . . .	66
4-2	Diagram of vector space model of the OMC . . . . .	68
5-1	Block diagram of dither alignment sensing. . . . .	73
5-2	Arrow diagram of dither alignment signals. . . . .	74
5-3	An instance of the noise performance of beacon alignment sensing. . . . .	76

6-1	Schematic diagram of the optical layout of a mode matching feedback control system. . . . .	83
7-1	Measurement of the bilinear coupling of beam jitter noise. . . . .	93
7-2	Comparison of vertical vibrational motion transmission of the Initial and Enhanced LIGO HAM chamber isolation systems. . . . .	94
7-3	Schematic of HAM6 optical layout. . . . .	95
7-4	The evolution of the passive Tip Tilt. . . . .	96
7-5	Measurement of HAM table motion coupling to beam motion. . . . .	97
7-6	Diagram of the Tip Tilt suspension with thick wires. . . . .	98
7-7	Measurement of interferometer sensitivity for different Tip Tilt designs.	98
7-8	Block diagram of the magnetometer feed forward system. . . . .	101
7-9	Measurement of the performance of the magnetometer feed forward system. . . . .	102
B-1	Diagram of the interaction of a beam with a beamsplitter. . . . .	119
B-2	Transverse intensity profile of the second order modes. . . . .	122
B-3	The effects of second order mode perturbations on the TEM <sub>00</sub> mode. . . . .	123
C-1	The dependence of shot noise on cavity finesse of a Fabry-Perot Michelson interferometer. . . . .	127

# List of Tables

3.1	Higher order mode frequency shifts in the OMC . . . . .	47
3.2	Measurements of the OMC intra-cavity losses. . . . .	49
6.1	Parameters used to calculate the sensitivity of the BPD. . . . .	85



# Chapter 1

## Gravitational waves

A story bordering on apocryphal states that Albert Einstein made two predictions about gravitational waves in 1916. First, that they exist, and second, that they were certainly too small for their effects to ever be directly measured in a detector. It is the hope of the author that in the coming years Einstein will be proved wrong for the second of these two predictions.

This chapter covers a very brief overview of the theory of gravitational waves.

### 1.1 Gravity according to Einstein

In 1915, Einstein described space-time as a four dimensional manifold which may be completely described by a metric tensor  $g$ . The space-time metric defines a co-variant interval between infinitesimally separated events as

$$ds^2 = g_{\mu\nu} dx^\mu dx^\nu, \quad (1.1)$$

where  $\mu$  and  $\nu$  are indices for the space and time coordinates, and  $g_{\mu\nu}$  are the elements of  $g$ . The trajectories of free particles are defined by geodesic paths in the manifold, which may be derived from the metric tensor [1, Chap. 3]. These trajectories of objects in the four dimensional manifold are the manifestation of the force of gravity in general relativity.



The metric satisfies the sourced field equation

$$G = \frac{8\pi G}{c^4} T, \quad (1.2)$$

where  $G$  is known as the Einstein tensor, a second-order differential operator acting on the metric tensor,  $G$  is Newton's constant,  $c$  is the speed of light, and  $T$  is the stress-energy tensor which holds information about all forms of energy in the space-time.

## 1.2 The general theory of relativity in the linearized regime

In the weak field limit of general relativity, the metric tensor  $g$  will be close to the Minkowski metric of special relativity [1, Chap. 7]. Far from sources of gravitational waves, the wave amplitudes will be quite small and thus

$$g_{\mu\nu} \approx \eta_{\mu\nu} + h_{\mu\nu}, \quad |h_{\mu\nu}| \ll 1. \quad (1.3)$$

where  $\eta_{\mu\nu}$  are the components of the Minkowski metric, and  $h_{\mu\nu}$  are small perturbations.

We are interested in wave-like solutions that will propagate in the absence of any source terms (although they may be created by sources), thus  $T = 0$ . For convenience we choose what is known as the *transverse traceless* gauge. Given these simplifications, Equation 1.2 becomes

$$\left( -\frac{1}{c^2} \frac{\partial^2}{\partial t^2} + \nabla^2 \right) h_{\mu\nu} = 0. \quad (1.4)$$

This is of course the wave equation in three dimensions, which has solutions of the form

$$h = A \exp(ik_\alpha x^\alpha). \quad (1.5)$$

Due to symmetries and chosen gauge conditions, a wave traveling in the  $z$  direction with amplitude  $\mathbf{A}$  has only two independent components [2, Chap. 9]

$$A_{xx} = -A_{yy} \equiv h_+,$$

$$A_{xy} = A_{yx} \equiv h_\times,$$

the rest being zero. Thus such a wave takes the form

$$\mathbf{h} \doteq \begin{bmatrix} 0 & 0 & 0 & 0 \\ 0 & h_+ & h_\times & 0 \\ 0 & h_\times & -h_+ & 0 \\ 0 & 0 & 0 & 0 \end{bmatrix} \cos(\omega[z/c - t]). \quad (1.6)$$

The two components represent two independent wave polarizations, ‘plus’ and ‘cross.’ Here we explore one of the physical observables of such a wave.

### 1.3 The phase of a pulse of light in the presence of a gravitational wave

Presume we have a device that can measure the phase of an electromagnetic wave. The device is not under the influence of any external forces apart from gravity. Suppose we send a pulse of light in a particular direction, we have arranged for the pulse to return to us with a system of mirrors and transceivers. The total phase measured (modulo  $2\pi$ ) of a light pulse with frequency  $f$  after traveling along a path  $S$  is<sup>1</sup>

$$\phi_{\text{round trip}} = 2\pi f \oint_S dt. \quad (1.7)$$

Along the path, the pulse follows a null trajectory ( $ds^2 = 0$ ) and furthermore, according to Equation 1.6, the metric does not mix time and spatial components

---

<sup>1</sup>The treatment given in this chapter assumes that the path taken by the light pulse is short compared to the wavelength of the gravitational wave, known as the ‘long wavelength approximation.’ A fully consistent relativistic treatment is given by Rakhmanov [3].



$(g_{0i} = g_{i0} = 0)$ , thus

$$c \, dt = \sqrt{g_{ij} \, dx^i \, dx^j}, \quad (1.8)$$

where  $i$  and  $j$  only include spatial components.

Let us consider a simple path made of two segments, propagation from the origin  $(0, 0, 0)$  to a point in the  $x$  direction which is  $L_x$  away  $(L_x, 0, 0)$ , and then back to the origin. The phase along this path is

$$\phi_{\text{round trip}}^{\text{x-path}} = \frac{2\pi f}{c} \left( \int_0^{L_x} - \int_{L_x}^0 \right) \sqrt{g_{xx}} \, dx \approx \frac{4\pi f}{c} L_x \left( 1 + \frac{h_+}{2} \right). \quad (1.9)$$

The same argument for a path along the  $y$  gives

$$\phi_{\text{round trip}}^{\text{y-path}} \approx \frac{4\pi f}{c} L_y \left( 1 - \frac{h_+}{2} \right). \quad (1.10)$$

Instead, we may choose a path along the line  $y = x$ , in this case integration is taken along  $u(\sigma) = (\sigma, \sigma, 0)$ . The phase obtained is

$$\phi_{\text{round trip}}^{\text{u-path}} \approx \frac{4\pi f}{c} L_u \left( 1 + \frac{h_\times}{2} \right). \quad (1.11)$$

Thus the effect of the  $h_+$  amplitude is to differentially stretch paths in the  $x$  and  $y$  directions, while  $h_\times$  stretches along axes  $45^\circ$  from  $x$  and  $y$ . The stretching effect is proportional to the unstretched length, and thus is manifested as a strain. The effect of a plus polarized wave on the apparent positions of a ring of masses, measured by an observer in the center, is shown in the form of a flip-book in the lower right corners of this thesis.

## 1.4 Sources of gravitational waves

Of the known physical forces, gravity is by far the most feeble. When Einstein first postulated the existence of gravitational waves, he thought their effects would never be detected.

According to General Relativity, the lowest mass-energy multipole moment that

may source gravitational radiation is the mass quadrupole. The lower moments, the mass-energy monopole and dipole are guaranteed constant by energy and momentum conservation, respectively [1, Section 7.5].

A system of two bodies in orbit is a splendid source of gravitational radiation. The first evidence of the existence of gravitational radiation came from the Hulse-Taylor pulsar system which showed the characteristic loss of orbital energy due to gravitational wave radiation damping [4]. The waves emitted by this system will have a discouragingly small amplitude of  $h \approx 10^{-26}$  when they reach Earth, not to mention a period of several hours.

A compact binary system such as the Hulse-Taylor binary in the final orbits before merger provides a more promising prospect for the creation of gravitational waves that may be measurable on Earth. In particular, the Hulse-Taylor binary system will decay in a time of order  $10^8$  years. The time scales of such collisions would lead to gravitational waves in the audio frequency band. Of the expected sources, the coalescence of black holes or neutron stars are the ones most likely to produce gravitational wave with enough magnitude to be detected on Earth with modern detectors [5]. Data taken from the LIGO and Virgo detectors have been analyzed and upper limits of these sources have been set [6, 7].

It is also possible that an aspherical spinning neutron star will produce waves large enough to be detected. Such waves would be largely monochromatic, with some modulation due to relative motion of the source and the Earth. Currently, the best limit on the gravitational radiation damping contribution of neutron star spin-down of the Crab[8] and Vela[9] pulsars are determined by the lack of gravitational radiation detected by LIGO and Virgo.

There are some transient gravitational wave sources for which no waveform models exist. An example of such a source would be the waves emitted by a supernova explosion. Searches for such unmodeled sources have yielded a strain sensitivity of  $\sim 10^{-21}/\sqrt{\text{Hz}}$  in the LIGO frequency band, but no waves have yet been detected [10].

We may one day discover a stationary, broadband source of gravitational radiation. Most cosmological model predict some level of stochastic gravitational wave



background [11, 12]. The information gained by detecting such waves will be extremely interesting because if they are of cosmological origin, they would have been created mere fractions of a second after the Big Bang. Most models predict, however, that such effects are out of range for currently conceived detectors.

Now we focus on the antennae used to detect gravitational radiation.

# Chapter 2

## Gravitational wave antennae

This chapter covers some of the essentials of laser interferometer gravitational wave antennae.<sup>1</sup> For further information, the author suggests the incredible introductory treatment by Saulson [14]. Some great resources on the details of the LIGO experiment are contained in the theses of Adhikari [15] and Ballmer [16], and more recently Fricke [17], Dooley [18] and Kissel [19].

### 2.1 Experimental efforts to detect gravitational waves

In 1960, Joseph Weber made the suggestion that an aluminum bar could be used as a gravitational wave antenna [20]. The idea being that as a burst of gravitational wave passes, it would induce a strain in the bar and excite the resonant mechanical modes of the bar. For reasons detailed elsewhere[21, 22], the scientific community was never able to verify Weber’s subsequent claims of detection[23] although various theories[24, 25] were developed to explain the enormous apparent flux of gravitational wave energy.

In the subsequent years following Weber’s pioneering work, resonant bar detectors have improved greatly. Modern bar detectors are cryogenically cooled, have much improved seismic isolation and make use of SQUIDS to readout the signal [26].

---

<sup>1</sup>The author likes the use of the word antenna to describe gravitational wave detectors. Mainly because these machines have a purpose beyond simply detecting waves, they are for receiving, and later analyzing, signals. Although they are not efficient gravitational wave transmitters [13].



Using light waves to measure gravitational perturbations was first pointed out by Pirani in 1956 [27]. It was not until 1971 that an early prototype interferometer was built in Malibu using an audio cassette recorder for data acquisition [28]. Shortly after that, a study done at MIT by R. Weiss identified almost all noise sources relevant for a kilometer length scale interferometer [29]. It is these broadband laser interferometer based gravitational wave antennae that provide the most compelling chance to directly measure these elusive waves.

In recent years, kilometer scale interferometers have been constructed and operated with the purpose of searching for gravitational waves. These are the American LIGO interferometers [30], the German-English GEO600 interferometer [31], and the Italian-French Virgo interferometer [32].

## 2.2 Measurement of optical phase

In Chapter 1 we introduced the idea that the waveform of a passing gravitational wave is imprinted on the phase of electromagnetic waves. The frequency of oscillation of a laser with a wavelength of  $1.064\mu\text{m}$  is  $2.8\times 10^{14}\text{Hz}$ . There is no technology, currently conceived, with which one can directly measure the phase of electromagnetic waves at optical frequencies. One may, however, convert the change of phase of the electromagnetic wave into a change of amplitude by means of the phenomenon of interference. This is achieved by superposing two electromagnetic waves and measuring the power of the resulting wave, which is straightforward with the use of a photodetector (PD).

A device which exploits interference to measure phase changes of light is referred to as an *interferometer*. Modern interferometers use one or multiple lasers as the source of light. Laser light is very well equipped for interferometry, is highly phase coherent compared to other light sources, and a laser beam can often approach the minimum beam divergence physically allowed. Types of interferometers include: Fabry-Perot, Michelson, Mach-Zehnder etc.

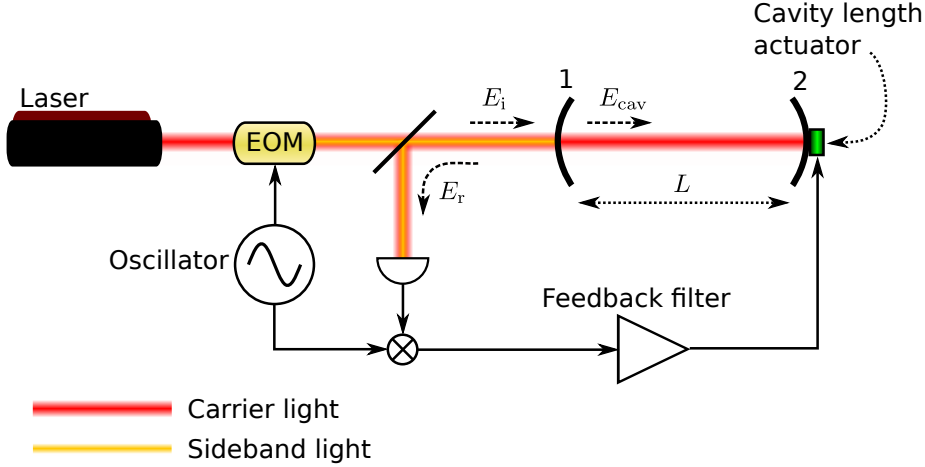


Figure 2-1: Diagram of a resonant cavity and control system. In this representation, the cavity is held on resonance by feeding back to the position of the end mirror. Alternatively, resonance can be achieved by feeding back to the laser frequency, causing the laser wavelength to follow the length of the cavity.

## 2.3 Resonant optical cavity

A resonant cavity, sometimes referred to as a Fabry-Perot (FP) cavity, is constructed with two partially transmitting mirrors placed in series. When light is incident on the front, or input, mirror, some of that light is transmitted into the cavity. As a steady state is approached, the light already in the cavity may interfere with new light which is being pumped through the input mirror. When the circulating field is in phase with the incident pumping field, *resonance* occurs. Assuming plane waves and a linear cavity, this happens when the length is equal to an integer number of half-wavelengths of the light [33].

We may consider the interference condition after steady state has been achieved as there being an intracavity field,  $E_{\text{cav}}$ , which is made up of some of the input light,  $E_i$  which has been transmitted, and some cavity light which has made a round trip path through the cavity. The arrangement of the fields may be seen in Figure 2-1.

$$E_{\text{cav}} = t_1 E_i + r_1 r_2 e^{i2kL} E_{\text{cav}}, \quad (2.1)$$

where  $r_j$  and  $t_j$  are the amplitude reflection and transmission coefficients of the cavity



mirrors, for  $j = \{1, 2\}$  with 1 being the label of the input mirror, and 2 being the label of the end mirror. This allows us to solve for the intra-cavity field

$$E_{\text{cav}} = \frac{t_1}{1 - r_1 r_2 e^{i2kL}} E_i. \quad (2.2)$$

As one can see, when  $2kL$  is close to a multiple of  $2\pi$ , the intracavity field is strongly enhanced. This circumstance is known as resonance. The reflected field is

$$E_r = -r_1 E_i + t_1 r_2 e^{i2kL} E_{\text{cav}} = \frac{-r_1 + (r_1^2 + t_1^2) e^{i2kL} r_2}{1 - r_1 r_2 e^{i2kL}} E_i. \quad (2.3)$$

Assuming no loss of the input mirror ( $r_1^2 + t_1^2 = 1$ ), the cavity field contains a factor of  $r_2 - r_1$  on resonance. Thus the sign of the reflected field on resonance depends on the relative magnitudes of the reflectivities of the cavity mirrors. In fact, when the reflectivities are equal, one has perfect impedance matching and no field is reflected. The case of  $r_2 > r_1$  is known as overcoupled, and the reflected field changes sign when passing through resonance. When  $r_2 < r_1$ , there is no sign change, and this is known as undercoupled. The case when no field is reflected ( $r_2 = r_1$ ) is known as critically coupled. The LIGO arm cavities (Section 2.6) are an example of strongly overcoupled cavities, while the output mode cleaner (Chapter 3) is a critically coupled cavity. Undercoupled cavities are more rare because the majority of the light does not penetrate the cavity and thus does not provide for a very sensitive measurement of the cavity.

The phase change on reflection is enhanced relative to the phase change inside the cavity. For a change of the intracavity phase  $\phi = kL$ , the phase of the reflected field will change as

$$\phi_r = 2 \tan^{-1} \left( \frac{2\mathcal{F}}{\pi} \phi \right), \quad (2.4)$$

where  $\mathcal{F}$  is known as the *cavity finesse* and has the approximate value  $\mathcal{F} \approx \pi \frac{\sqrt{r_1 r_2}}{1 - r_1 r_2}$  where the approximation is valid for  $\{r_1, r_2\} \approx 1$ . For large values of the finesse, the phase of the reflected field has a steep variation compared to the intracavity phase. A very typical cavity may have a finesse of a few hundred. Colloquially this can

be viewed as the light making several bounces in the cavity before exiting and thus experience an accumulated phase gain many times that of a single round trip.

## 2.4 Pound-Drever-Hall reflection locking

Pound-Drever-Hall (PDH) reflection locking is a powerful technique by which the resonance condition of a laser incident on an optical cavity may be controlled by use of a feedback control system [34]. In this control system, the error signal is a measurement of the detuning of the laser light from resonance. In the case of a fixed length cavity, this may be understood as a measurement of the fluctuations in the laser wavelength. We are instead concerned with a very stable laser source and a cavity which may change length due to external influences.<sup>2</sup> In this case, the error signal is better understood as a measurement of the length changes of the cavity.

As was shown in the previous section, the phase shift of the beam reflected from the resonant cavity is enhanced for fields resonant in the cavity. However, for fields not resonant in the cavity, there is nearly no phase shift of the reflected beam for a given length change. The PDH sensing technique exploits this fact by constructing an input beam with frequency components that are both resonant and non-resonant. By doing a relative phase measurement of the reflected fields, one may determine length changes of the cavity.

Preparation of the input beam for PDH is done by sending the beam through an optical modulator capable of phase modulation. This usually comes in the form of an *electro optic modulator* (EOM), which is an optical device that has a electronically variable optical path length. Applying a periodic electronic signal, usually at radio frequencies (RF), will induce a periodic phase modulation of the laser beam. As will be discussed in Section 4.1, the primary result of this phase modulation is to impose new optical fields separated in frequency from the original field by the RF modulation frequency. These new fields are usually referred to as *phase modulated sidebands*, the

---

<sup>2</sup>A gravitational wave changes the phase accumulated in the cavity, which is essentially interchangeable with the optical path length of the cavity.



central frequency component is referred to as the *carrier*. Figure 2-1 shows a typical arrangement of a PDH control system. The modulation frequency is chosen such that the sidebands are not resonant in the cavity, and thus do not experience a phase shift when the cavity changes length. Comparison of the constant sideband phase with the resonating carrier phase through interferometry yields a very sensitive cavity length measurement.

Because the modulator is varying the phase of the laser field, ideally there is no associated amplitude modulation. Mathematically this is represented by the phase sidebands having an imaginary amplitude when compared to the carrier, they have a  $90^\circ$  relative angle in the complex phasor plane. The arm-cavities are strongly overcoupled, thus when the carrier is exactly centered on resonance, the reflected field experiences a  $180^\circ$  phase shift. Thus the phase sidebands are still phase sidebands. When the carrier is slightly detuned from resonance, the relative angle between the carrier and sidebands changes and what were once pure phase sidebands now have some amount of amplitude component. Thus the power in the reflected beam now experiences a modulation. Demodulating the power recorded by a photodetector in reflection will provide the desired length error signal.

## 2.5 The Michelson interferometer

The pre-stabilized laser and input optics systems provide the LIGO interferometers with an extremely stable light source with which to measure phase perturbations. To provide a phase sensitivity necessary to detect gravitational waves it will be necessary to play a few tricks to hide our gravitational wave readout system from the noise still present on the input laser.

A Michelson interferometer (shown in Figure 2-2) is composed of a beamsplitter, which usually has a power reflectivity of 50%, and two highly reflecting mirrors in each arm. The laser field propagates down each arm, before reflecting back towards the beamsplitter. The two beams then interfere at the beamsplitter and the intensity of light at the reflection and transmission ports vary with the differential length change

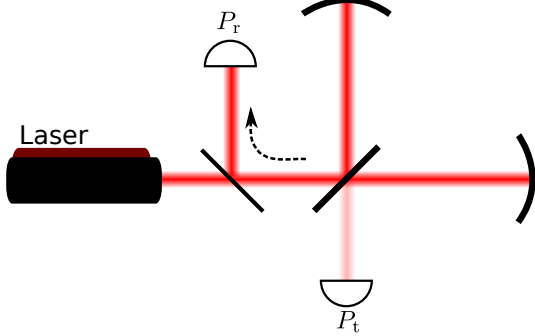


Figure 2-2: Diagram of Michelson interferometer. Photodetectors are arranged to measure the transmitted power,  $P_t$ , and the reflected power,  $P_r$ . The interferometer is operated near a dark fringe on transmission, and most of the light is directed to the reflection photodetector.

of the arms. The power measured exiting each port is:

$$\frac{P_t}{P_{\text{BS}}} = \left( \frac{r_1 + r_2}{2} \right)^2 \sin^2(kl_-) + \left( \frac{r_1 - r_2}{2} \right)^2 \cos^2(kl_-), \quad (2.5)$$

$$\frac{P_r}{P_{\text{BS}}} = \left( \frac{r_1 + r_2}{2} \right)^2 \cos^2(kl_-) + \left( \frac{r_1 - r_2}{2} \right)^2 \sin^2(kl_-), \quad (2.6)$$

where  $r_{1,2}$  are the amplitude reflectivities of the mirrors,  $k = 2\pi/\lambda$  is the wavenumber of the light,  $P_{\text{BS}}$  is the power incident on the beamsplitter, and  $l_-$  is the difference of the lengths of the two arms. Thus one may measure the power dependence at one or both ports to measure differential length changes. The power dependence at the transmission port is periodic with differential length changes of the interferometer. At first glance it might be desirable to make the “set point” of the interferometer be the place where the power varies most as a function of the differential length. In this case, halfway between the maximum and minimum of the fringe would have the greatest derivative and thus would maximize the signal measured for any given length change. This ignores, however the dependence of sensing noise on the interferometer set point. Shot noise is a fundamental source of measurement uncertainty due to the random arrival of photons on the photodetector. Generically, a photodetector which



measured a power  $P$  will measure an amplitude spectral density of shot noise of

$$N_{\text{shot}} = \sqrt{2 \frac{hc}{\lambda} P}. \quad (2.7)$$

In the case of the Michelson interferometer, for a measurement of the transmitted power  $P_t$ , and assuming  $r_1 = r_2 = 1$ , the amplitude spectral density of the shot noise is:

$$N_{\text{shot}} = \sqrt{2 \frac{hc}{\lambda} P_i \sin^2(kl_-)}. \quad (2.8)$$

For a static interferometer set point  $l_-$  with a small length variation  $\delta l$ , the resulting signal will be

$$S = \frac{\partial P_i}{\partial l_-}(l_-) \times \delta l = 2P_i \sin(kl_-) \cos(kl_-) \times k\delta l \quad (2.9)$$

We may then determine the signal to noise ratio (SNR) of measurements of the differential length change of the interferometer. The noise varies as  $|\sin(kl_-)|$  while the signal varies as  $\sin(kl_-) \cos(kl_-)$ , thus the SNR will vary as  $\cos(kl_-)$ . As one can see, the maximum of the magnitude of the signal to noise is achieved at  $kl_- = m\lambda$  for  $m \in \mathbb{Z}$ , which is (quite counter intuitively!) when no light is on the photodetector. In practice, some small amount of light will need to be on the photodetector so that the signal can overcome other sources of sensing noise. Though, as long as the offset remains small, the SNR approaches the maximum value. Applying this scheme of using a small static offset of the Michelson fringe to the initial LIGO detectors was one of the major upgrades performed in Enhanced LIGO. Other benefits of using this technique over a RF demodulation style technique is discussed in Section 2.9.

Using the analogy which treats the laser wavelength as a ruler with which one measures optical path length, there is an intuitive picture which shows why the correct arrangement of a Michelson interferometer may be made insensitive to fluctuations of your ruler. Because the beamsplitter directs the same laser source to each arm, it is obvious that fluctuations of the laser wavelength (our ruler) will be identical in both arms. This is a problem if one desires to measure the average length of the two arms, fluctuations in your ruler will directly cause fluctuations in your measurement. If,

instead, the differential arm length change is the desired measurement, ruler length fluctuations are suppressed. For these reasons, both amplitude and phase fluctuations of the laser light are common mode and thus suppressed when making a differential measurement of the arm lengths. This is covered quantitatively in Section 10.4 of Malik Rakhmanov’s thesis [35].

To maximize the differential arm phase difference of a gravitational wave, one should choose the angle between the Michelson arms to match the “shape” of the waves. As seen in Chapter 1, gravitational waves stretch and squish along perpendicular axes. Therefore the most common arrangement of a Michelson ( $90^\circ$ ) also happens to be the optimum for detecting gravitational waves.

## 2.6 Michelson with arm-cavities

One may exploit the common mode rejection of laser noise provided by the Michelson interferometer, while taking advantage of the high phase sensitivity of a resonant cavity, by joining the two designs. The LIGO detectors achieve this by converting both arms of the Michelson each into resonant cavities. This is heuristically similar to making a Michelson with much longer arms due to the phase gain of the arm cavities.

The resonance condition enforced by the control systems is that a half-odd integer number of wavelengths fit in the length of the cavity, or  $L = n\lambda/2$  for some large integer  $n$ . In terms of the optical frequency  $f$  this is  $L = nc/f$ . Thus if the control system holds the cavity on resonance by modifying the laser frequency,  $\delta f$ , and there is a length change  $\delta L$ ,

$$\begin{aligned}\delta L &= -\frac{nc}{f^2}\delta f, \\ \frac{\delta L}{L} &= -\frac{\delta f}{f}.\end{aligned}\tag{2.10}$$

When a laser is locked to a cavity via a control system, the cavity length fluctuations are directly linked to the frequency fluctuations of the laser. Thus one may stabilize the frequency noise of a laser by locking the laser to a cavity. Provided that the



length of the cavity is sufficiently stable, this may be used to reduce the frequency noise of the laser below its intrinsic level. Additionally, according to Equation 2.10, this becomes more effective as the cavity is made longer.

This shows a trick one may play once the effort has been spent to build two arm-cavities. We saw above that the common arm length of the interferometer may be difficult to measure due to laser frequency noise. So it is not practical to use the common arm mode as a gravitational wave sensor. To not let effectively half of one's interferometer go to waste, one may exploit this additional optical cavity as a stable length reference. This is known as the *common mode servo*.

## 2.7 Power recycling

Apart from the small fraction of light which is lost due to absorption or scattering, most of the light incident on a Michelson interferometer operating on the dark fringe is reflected back from the input port toward the laser. The solution to this very un-green situation is that the light can be directed back into the interferometer using a technique known as *power recycling*. The most straightforward way to understand power recycling is to consider the interferometer as a kind of mirror. If one places another mirror, called the power recycling mirror (PRM), between the laser and interferometer, the new system forms a resonant cavity. A careful choice of the reflectivity of the power recycling mirror makes this resonant cavity critically coupled, and thus a minimal amount of light is reflected back toward the laser. In the case of LIGO, the power incident on the beam splitter can be enhanced by a factor of around 50, which correspondingly decreases the shot noise as in Equation 2.8.

## 2.8 Sensing and control of a power recycled Michelson interferometer with arm-cavities

The optical setup of the full LIGO interferometer is quite a bit more complicated than that of a single cavity. To maintain the resonance condition of the entire interferom-

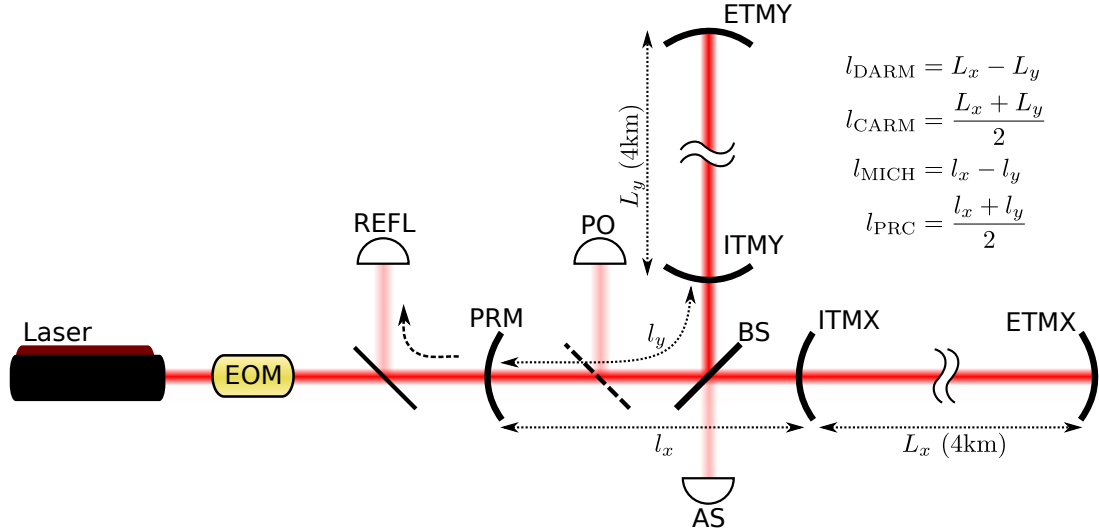


Figure 2-3: Diagram of a power-recycled Fabry-Perot Michelson interferometer. This is a simplified version of the optical configuration of the LIGO interferometer. Also shown are the definitions of the canonical length degrees of freedom.

eter, it is necessary to sense and control four independent length degrees of freedom. It so happens that the technique of PDH reflection locking is well adapted for sensing the length degrees of freedom of more complicated interferometers. Placing one's photodetectors at the correct ports of the interferometer can provide all needed information for length sensing. The canonical reference on the topic is Fritschel et al. [36], but we will provide a short summary.

As seen in Figure 2-3, the interferometer is composed of six primary mirrors. These are the *power recycling mirror* (PRM), the *beamsplitter* (BS) and the arm cavity optics, referred to as the *end test mass* (ETM) and *input test mass* (ITM), one for each arm, labeled X and Y. Only four degrees of freedom are relevant and measurable by their optical path length. In the case of LIGO, the degrees of freedom of all the mirrors are measured relative to the ITMs. The basis chosen to represent these lengths is shown in Figure 2-3. The length degrees of freedom are referred to as the *differential arm length* (DARM), the *common arm length* (CARM), the *power recycling cavity length* (PRC) and the *Michelson length* (MICH).

Due to the optical topology and location of the sensors, the different sensing ports provide information about the various degrees of freedom of the interferometer. As



in PDH, the light is phase modulated at RF frequencies before being injected into the interferometer and the length signal is encoded as an RF amplitude modulation of the photodetector power. Photodetectors are located at several output ports of the interferometer. The modulation can be in the cosine (in-phase, I) or sine (quadrature-phase, Q) quadratures. The length degree of freedom with most sensitivity to gravitational waves is DARM, which is the primary signal present at the antisymmetric (AS) port, though the AS port also has some contribution from MICH. MICH is the dominant contribution to the power recycling cavity pickoff (PO) port in the Q phase. The I phase of the PO port, and the reflection (REFL) port, both have a primary contribution from CARM, with a small contribution from PRC. This presents the difficult task of having two sensors which are nearly degenerate in the sensed degree of freedom. In LIGO this is solved due to the very high gain of the common mode servo. The common mode servo strongly suppresses the REFEL signal, creating a gain hierarchy with the PO-I signal. The signal which remains in PO-I is purely PRC.

The next generation of interferometers, including Advanced LIGO, will include an additional signal recycling mirror which sits between the BS and the AS port. This adds an additional length degree of freedom which further complicates the sensing and control [37].

## 2.9 A static (DC) readout

Prior to the beginning of Advanced LIGO, there was a incremental upgrade called Enhanced LIGO. One of the modifications performed during the Enhanced LIGO upgrade was to change the scheme for sensing the DARM degree of freedom. The DC power at the AS port has a quadratic dependence on DARM. Thus if the arm cavities are differentially detuned slightly (on the order of 10 picometers) from resonance, there will be a linear dependence of the DC power from DARM. An alternate picture of the scheme is that in the RF scheme, the RF sidebands are the local oscillator which beats against the gravitational wave sidebands to produce an RF signal, which

is a form of heterodyne detection. While in the DC case, the DARM offset produces a local oscillator at the same baseband frequency as the signal sidebands, which is a form of homodyne readout. A photodetector which measures this DC power at the AS port is an alternative sensor for reading out DARM. DC readout of DARM has been implemented on the GEO600 detector [38], the Caltech 40 meter prototype interferometer [39], and for Enhanced LIGO [40]. DC readout of DARM is also part of the baseline design for Advanced LIGO. A very thorough treatment of the subject can be found in Tobin Fricke’s PhD dissertation [17]. Here we will cover some of the benefits of such a scheme.

Light which resonates in the compound system composed of the arm cavities and the power recycling cavity experiences an effective cavity bandwidth which is much more narrow than the bandwidth of the arm cavities alone [35]. This narrow bandwidth acts as a effective low pass filter of the laser noise fluctuations on the light. In the LIGO interferometers, the carrier light is resonant in the coupled cavity system and experiences a filter with a corner frequency of approximately 1Hz. The RF sidebands do not resonate in the arm cavities and thus do not experience such dramatic filtering. The carrier light thus serves as a much quieter local oscillator than the RF sidebands. Thus switching to DC readout can reduce many laser noise couplings.

There is an intrinsic reduction in the shot noise when going from RF to DC readout. The total power on the detector is modulated at twice the frequency of the RF sidebands due to the beating of the upper and lower sidebands with each other. The RF demodulation of DARM preferentially samples the signal at the peaks of the RF modulation, leading to a shot noise contribution higher than the DC case by a factor of  $\sqrt{3/2}$ . There is a very nice treatment of this effect in Section 2.9 of Tobin Fricke’s dissertation [17].

An interferometer that employs DC readout is a more attractive candidate for the use of squeezed light injection to improve the interferometer sensitivity. By contrast to an RF readout scheme, an interferometer with DC readout only requires squeezing at audio frequencies, not audio and RF frequencies [41, 42].



One of the drawbacks of DC readout is that the audio frequency modulation of any of the optical fields present at the AS port can cause noise in the readout. To mitigate the existence of the fields not necessary for producing the signal, i.e. any fields that are not the local oscillator or the signal fields, one may utilize an output mode cleaner. The output mode cleaner acts as both a spatial and frequency filter of the fields detected at the AS port and will be described in detail in the following chapter.

# Chapter 3

## The output mode cleaner

One of the primary components of the Enhanced LIGO upgrade was the addition of an output mode cleaner or OMC [43]. This chapter describes the motivation for installing an OMC and some measurements of the performance of the OMC installed on the H1 interferometer at the LIGO Hanford Observatory.

### 3.1 Motivation for an OMC

The interferometer is supplied with a beam that has a very nearly pure Gaussian spatial profile thanks to the input mode cleaner. The input mode cleaner is a nearly critically coupled resonant optical cavity which filters the beam supplied by the laser before it is delivered to the interferometer input. The power recycling cavity builds up power and delivers it to the long arms. The arms further recycle the laser light and this large resonant field acts as the source field that gets modulated by a passing gravitational wave and pumps light into sidebands at the gravitational wave frequency. The gravitational wave signal on the PD comprises the beat note of these audio frequency sidebands with a strong coherent field. Although the beam delivered by the input mode cleaner is spatially very pure, the efficiency of coupling this beam to the final resonant mode of the arm cavity is not ideal. Components of the input light that are not matched to the mode of the arm cavity will not resonate and some of this unmatched light will exit the antisymmetric port along with the signal light. The



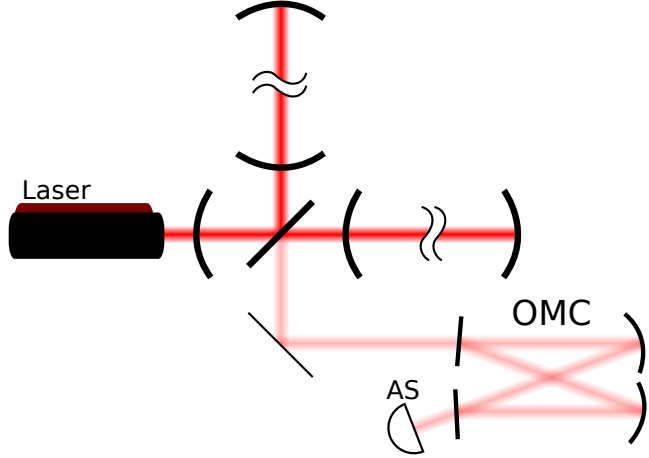


Figure 3-1: Diagram showing the location of the OMC. This diagram is not drawn to scale.

unmatched light at the antisymmetric port will exist as higher order modes (HOM) relative to the arm cavity mode and is often referred to as “junk light.” The presence of this light on a photodetector will contribute photon shot noise. Also, if the coupling is time dependent, the time variation of the junk light directly contaminate the signal with noise.

It is, therefore, desirable to be able to separate the junk light from the signal rich audio frequency fields originating in the arm cavities. A critically coupled resonant optical cavity is a natural spatial filter for light. When placed at the output of the interferometer between the AS port and the PD, as seen in Figure 3-1, we refer to such a cavity as the output mode cleaner (OMC).

It can be useful to point out that interferometers based on both RF and DC readout can benefit from an OMC. Both the GEO and Virgo interferometers have used OMCs in an RF readout configuration, and LIGO experimented with an OMC before using DC readout [44]. An OMC is especially important for a DC readout interferometer because any audio frequency modulation of fields that are not the local oscillator or signal will contaminate the readout. Because readout is performed at DC, all audio frequency interference of the fields will directly couple to the signal channel, as opposed to an RF heterodyne scheme where the signal is shifted away

from low frequency interference. An OMC may also be used to ensure that the light provided by the differential arm offset dominates the DC power present on the detection photodiode, otherwise DC power from other fields (such as the RF sidebands) will contribute to photon shot noise without increasing the signal strength.

Thus, for an interferometer that employs DC readout, the OMC should efficiently strip the HOM field components of the carrier field as well as the RF sidebands. This is achieved by creating a cavity with a narrow linewidth, capable of transmitting the desired (carrier) field, while filtering out higher frequencies. Ideally, being a critically coupled optical cavity, light incident on the OMC is totally transmitted on resonance. The normalized transmission of the off-resonant fields is given by

$$\frac{T}{T_0} = \frac{1}{1 + \frac{4}{\pi^2} \mathcal{F}^2 \sin^2 \phi}, \quad (3.1)$$

where  $\mathcal{F}$  is known as the *cavity finesse* (see also Section 3.3.3) and  $\phi$  is the detuning from resonance. In terms of a frequency detuning of  $\Delta f$  of the incident light,  $\phi = \pi \Delta f / \text{FSR}$ . The FSR is the frequency spacing of successive resonances, discussed in Section 3.3.1.

## 3.2 Optical and mechanical design of the OMC

Prior to Enhanced LIGO, experiments were performed using a OMC borrowed from the GEO600 interferometer to investigate the difficulties in using an OMC with LIGO. Noise introduced from jitter of the OMC input beam due to air currents and mechanical vibrations spoiled the sensitivity of the LIGO detector when the OMC was used. Consequently, one of the most obvious lessons learned from these investigations was the need to house the OMC in a low vibration environment. For Enhanced LIGO, it was decided that the OMC would be housed inside the vacuum system and would be isolated from vibrations of the environment through the use of a seismically isolated optics table as well as a suspension system to provide passive filtering of vibrations.



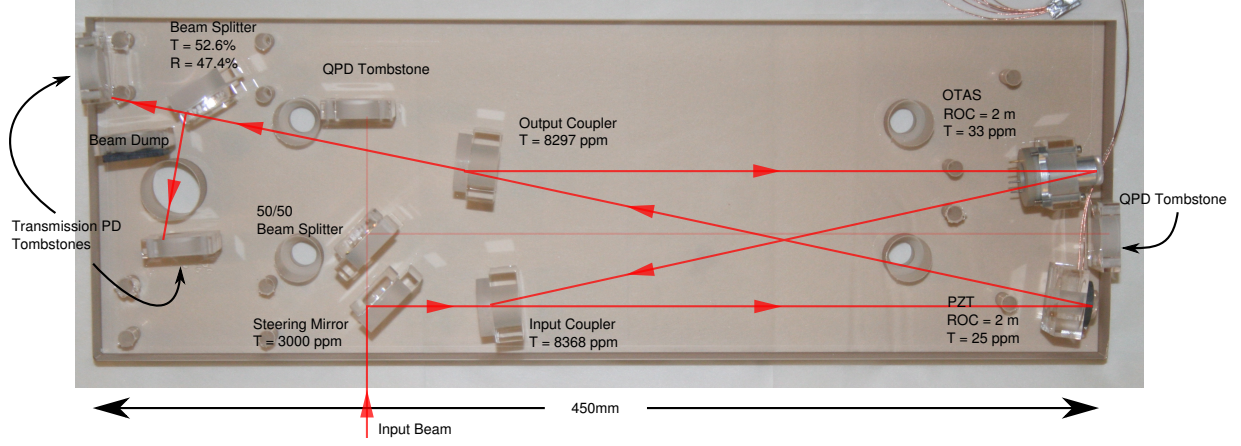


Figure 3-2: Photograph of the OMC. The strong red line shows the primary beam path. The light red line shows the QPD sample of the input beam. Only shown are the QPD and transmission PD tombstones, the actual photodetectors are not mounted in this photograph. Photograph credit to Sam Waldman.

### 3.2.1 Cavity optics

The design of the OMC was chosen to be a four mirror bow-tie cavity. This choice was made over that of a two mirror linear cavity so that there was spatial separation of the reflected beam. An even number of mirrors was chosen such that the horizontal and vertical HOMs would experience the same overall phase shift and thus experience nearly the same frequency offset from resonance, reducing the chances of an accidental HOM resonance.

A diagram of the OMC may be seen in Figure 3-3. The OMC optics are bonded with Vacseal epoxy onto custom designed fused silica optics mounts, called tombstones. The tombstones were then bonded to a slab of Corning ultra-low expansion (ULE) Glass<sup>1</sup> with UV cure epoxy from Optocast, which we will refer to as the *OMC breadboard*, pictured in Figure 3-2. Figure 3-4 shows the OMC input coupler mirror and tombstone, bonded to the breadboard. This arrangement fixed the cavity length to the desired value and was designed to be stable against thermal variation. The microscopic cavity length was controlled using a pair of actuators. A fast PZT between one of the optics and its tombstone acted as a low range (1/10 of a wavelength) high

---

<sup>1</sup>The dimensions of the OMC breadboard are 450mm × 150mm × 39mm

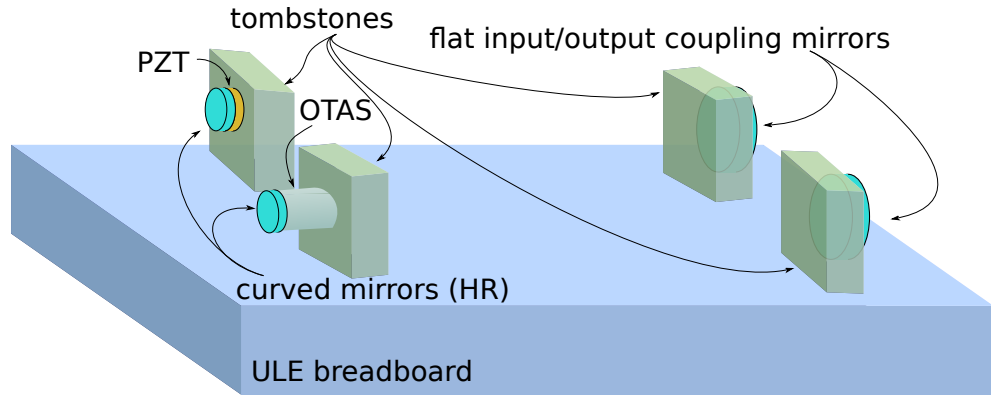


Figure 3-3: Diagram of OMC cavity components. Auxiliary optics and sensors are not shown. The tombstones have holes (not pictured) machined in them to allow the laser beam to pass through (see Figure 3-4 for a photograph of the input coupler and tombstone.)

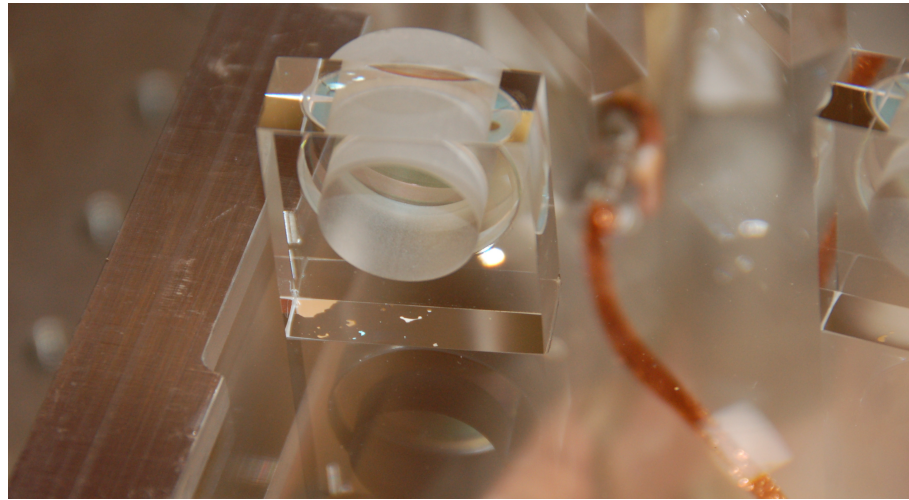


Figure 3-4: Close up photograph of the OMC input coupler mirror. The photograph is taken from the in-cavity side of the optic.



bandwidth (5kHz) length actuator. Long range (several wavelengths) actuation was provided by one cavity mirror situated at the end of an aluminum tube heated by a ceramic heating element, affectionately referred to as the OTAS.<sup>2</sup>

A mode cleaner cavity is purposefully designed such that HOMs do not occupy a degenerate resonance with the resonant  $\text{TEM}_{00}$  mode (see Section B.4 on how a mode cleaner acts as a filter of transverse modes). Cavities are commonly characterized by their stability  $g$ -parameter.<sup>3</sup> The Gouy phase shift,  $\eta$ , is the phase shift of a focused  $\text{TEM}_{00}$  beam relative to a plane electromagnetic wave. The round trip Gouy shift in the cavity is determined by the cavity geometry as

$$\cos(\eta) = g, \quad (3.2)$$

where the  $g$ -parameter is usually given by  $g = 1 - L/R$  for a linear cavity of length  $L$  and mirror radius of curvature  $R$  [45]. The OMC is not a linear cavity, the light travels the length of the cavity only once during a full round trip. To avoid confusion we will use the *perimeter*,  $p$ , to denote the full round trip length. One may substitute  $2L = p$  in most formulae for linear cavities. An extensive analysis was done by Sam Waldman to determine the optimal cavity geometry to minimize the transmission of off-resonant HOM and frequency components through the OMC [46]. The final design of the OMC was chosen to have a perimeter length of 1.042m, with 2m radius of curvature curved optics, giving a  $g$ -parameter of 0.7395 and a Gouy phase shift of  $0.235\pi$  radians. This implies that the fourth-order HOMs will accumulate almost  $\pi$  radians relative to the  $\text{TEM}_{00}$  mode and be somewhat close to resonance.

### 3.2.2 Sensors and auxiliary optics

The gravitational wave signal readout is derived from the OMC transmitted power. The light transmitted by the OMC is split by a near 50/50 beam splitter and detected on two photodiodes. Both the beam splitter and photodiodes are located on the OMC

---

<sup>2</sup>OMC Thermal Actuation System

<sup>3</sup>Asymmetric cavities are often given two  $g$ -parameters, one for each mirror (labeled 1 and 2) and  $g = \sqrt{g_1 g_2}$ .

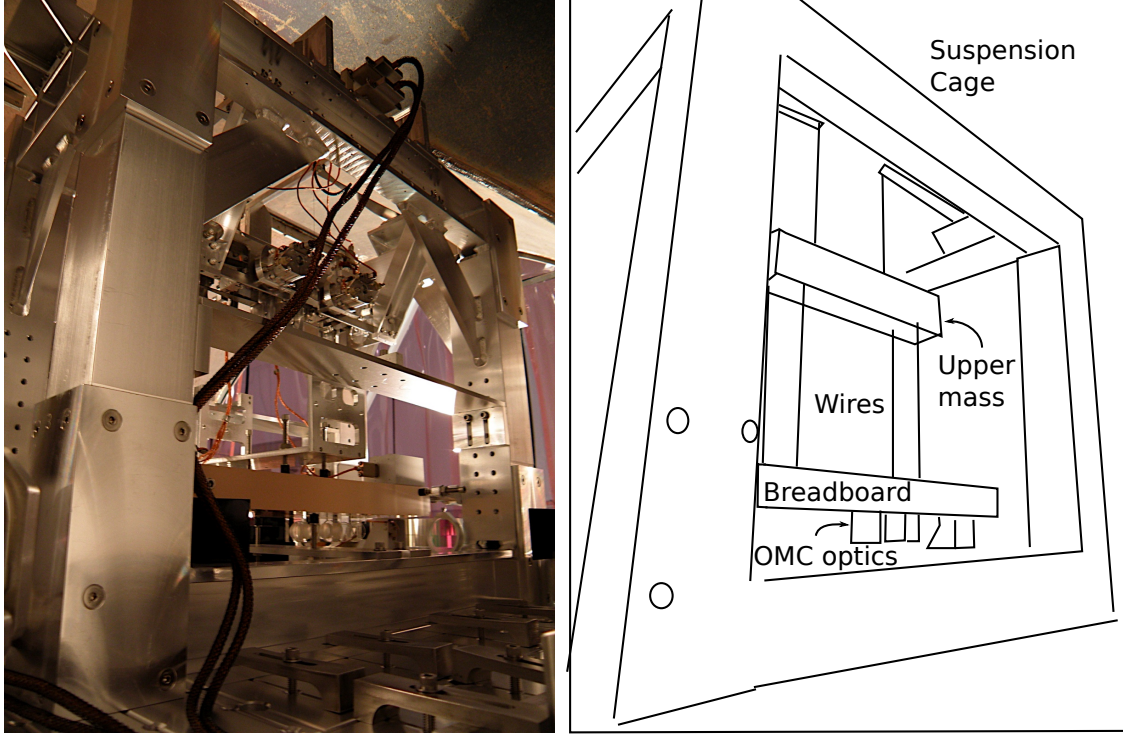


Figure 3-5: Photograph of the OMC double pendulum suspension. The line sketch shows the upper mass stage, which is obscured in the photograph by the coil actuators.

breadboard. The beamsplitter is glued to a tombstone similar to that of the cavity optics. The photodiodes were attached to tombstones via a sandwich of metal plates screwed together around the tombstone. This arrangement ensured that the OMC transmitted beam would not drift relative to the readout detectors.

A steering mirror on the OMC breadboard transmitted a small sample of the incoming beam allowing the input pointing to be analyzed by two quadrant photodiodes (QPDs). A 50/50 beam splitter distributed equal amounts of the input beam to the two QPDs. The QPDs were located at different distances from the beam splitter to allow both beam angle and lateral position to be measured. The location of all the OMC sensors can be seen in Figure 3-2.



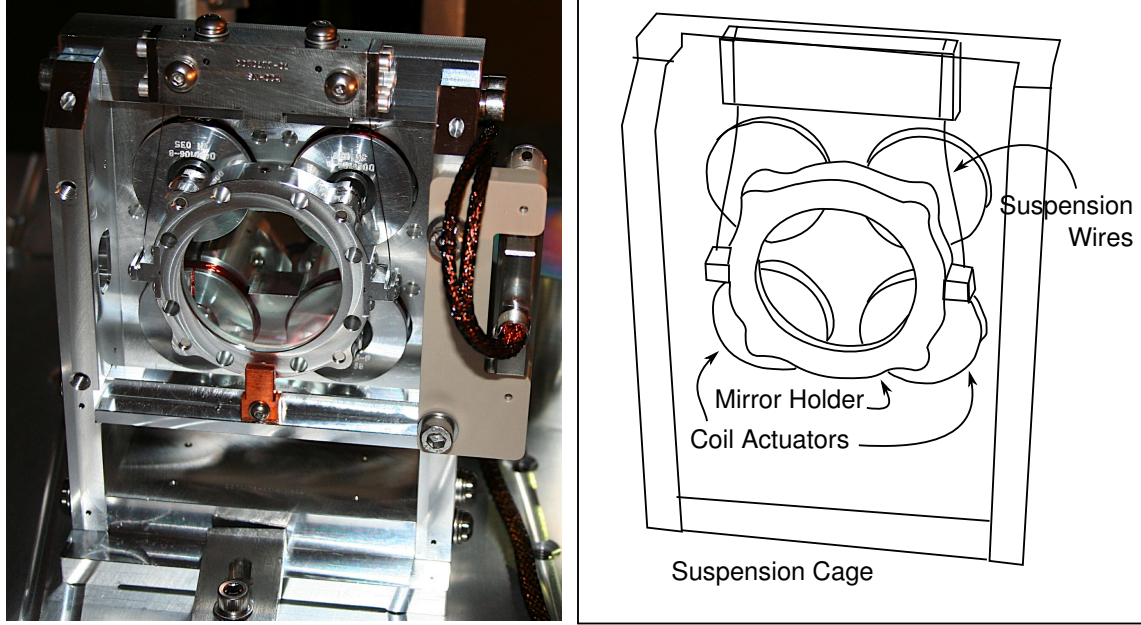


Figure 3-6: Photograph of a Tip Tilt optic. The original Tip Tilt design is shown, before being retrofitted with blade springs. Alignment actuation control is provided by coil actuators coupled to permanent magnets housed in the mirror holder.

### 3.2.3 Suspension system

The OMC breadboard was suspended from a two stage vibration isolation suspension, pictured in Figure 3-5. On the optics table was a large steel frame which housed the OMC. An upper mass stage was suspended from the frame by two pendulum wires attached to the ends of blade springs. The OMC breadboard was then suspended by four more wires attached to blade springs from the upper mass stage. Servo control provided feedback damping of the suspension eigenmodes. All actuation and sensing was performed on the intermediate stage, with actuation provided by electromagnetic coil actuators attached to the cage which applied forces to permanent magnets attached to the upper mass. The actuator module also housed the sensing system which consisted of LED shadow sensors which measured the position of protruding flags attached to the magnets used for actuation.

### 3.2.4 Mode matching telescope

The beam exiting the interferometer from the antisymmetric port was directed through a beam steering and mode matching telescope. The purpose of such a telescope is to correctly align and focus the beam exiting the interferometer to maximize the transmission of the gravitational wave signal through the OMC.

The steering optics were housed in a single pendulum suspension system. The suspension and optics were collectively referred to as *Tip-Tilt optics*,<sup>4</sup> one of which is pictured in Figure 3-6. The mounting and suspension of the beam steering optics underwent several modifications during the Enhanced LIGO project (see Chapter 7). The final configuration consisted of three highly reflective curved mirrors. Two suspended by a single pendulum stage, with vertical isolation provided by blade springs, and a coil-magnet/shadow sensor system similar to that used in the OMC suspension. The actuator system allowed feedback control of the optic angle for active beam alignment. The third was housed in a similar suspension system, but without any sensing or actuation capabilities.

### 3.2.5 Vibration isolation table

The Tip-Tilts and OMC suspension frame were all housed in a single vacuum chamber and situated on top of a actively controlled seismic isolation table, the HAM-ISI.<sup>5</sup> The HAM-ISI employed a single stage of passive vibration isolation, coupled with active feedback control using inertial sensors as the primary error signal. A thorough account of the HAM-ISI design and performance is given in Chapter 5 of Jeff Kissel's thesis [19].

## 3.3 Characterization of the H1 OMC

Figure 3-7 shows a diagram of the experimental setup used to measure several parameters of the OMC that was installed on the H1 LIGO interferometer in Hanford, WA.

---

<sup>4</sup>The Tip Tilts were designed by B. Slagmolen of the Australian National University[47].

<sup>5</sup>HAM chamber Internal Seismic Isolation system



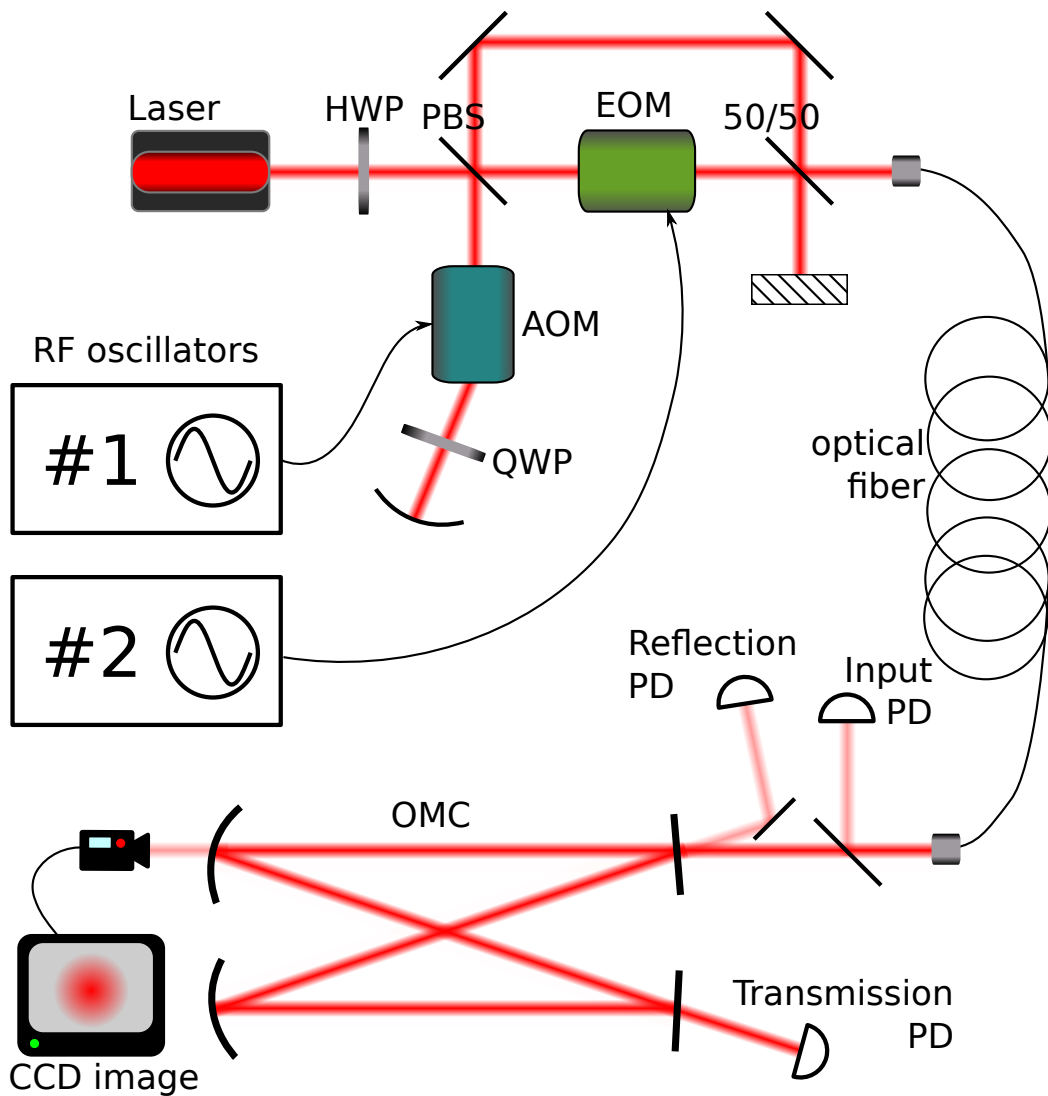


Figure 3-7: Block diagram of OMC characterization setup, also known as the OMC interrogator. The setup provides single mode laser light with RF sidebands for reflection locking, as well as a subcarrier with a tunable frequency.

These measurements were done prior to the installation of the OMC into the interferometer. The laser source is a Nd:YAG NPRO providing a 1064nm wavelength laser beam. The polarization is rotated by a half-wave plate (HWP). A polarizing beam splitter (PBS) sends some fraction of the light through an electro-optic modulator (EOM) which is driven at by RF oscillator #2. The fraction transmitted by the PBS is tuned by changing the angle of the HWP. The EOM introduces two RF sidebands which will be used for cavity length control. The other path of light is directed to an acousto-optic modulator (AOM). The light is double passed though the AOM and receives a frequency shift which is twice the frequency of RF oscillator #1. A quarter-wave plate (QWP) causes the polarization to rotate 90° after double passing, causing both paths to now be in the same polarization. The light from the two paths are recombined before being injected into an optical fiber. The frequency makeup of the combined beam includes the original carrier frequency, two RF sidebands and a frequency shifted subcarrier.

The light exiting the other end of the optical fiber is incident on the input coupling mirror of the OMC cavity. A small sample of the input beam is incident on a photodetector. The promptly reflected beam is detected on a photodetector where the photocurrent is demodulated at the frequency of RF oscillator #2 for a PDH style locking scheme. The frequency of oscillator #2 is chosen so that it is outside of the OMC resonance when the carrier is in resonance. This provides an error signal which is fed back to the frequency actuator of the laser. The control system is able to maintain resonance of the laser in the OMC. The laser transmitted through the OMC is detected on another photodetector. A very small sample of the light in the cavity is transmitted through one of the HR mirrors and detected by a CCD sensor.

### 3.3.1 Free spectral range

Resonance occurs in the cavity when the total round trip phase of the incident laser beam as it propagates through the cavity is an integer multiple of  $2\pi$ . In terms of the frequency of the laser beam, this occurs at multiples of what is called the *free spectral range* (FSR). The FSR is related to the round trip cavity perimeter  $p$  by  $\text{FSR} = c/p$ .



The technique used to measure the cavity FSR involved locking the laser frequency so the carrier was resonant in the OMC while varying the frequency of the subcarrier, causing it to pass through resonance, and measuring the OMC transmitted power. The OMC transmitted power will be maximized when the subcarrier is separated from the carrier by a multiple of the FSR.

The RF frequency generator was tuned to maximize the subcarrier transmission. The error was estimated to be the smallest frequency step that did not cause a noticeable change in transmission. The measured FSR is

$$\text{FSR} = 278.288 \pm 0.001\text{MHz}. \quad (3.3)$$

This corresponds to a cavity perimeter of 1.077m. The length differs from the design value, though the purpose of the design was that the fourth order modes are close to, but outside of resonance, as measured in the following section.

### 3.3.2 Higher order mode spacing

Similarly, the higher order mode frequency shift is measured by varying the subcarrier frequency until the subcarrier is resonant on a higher order mode of the OMC [48]. Coupling of the subcarrier beam into the HOMs is enhanced if slight misalignments are introduced on the input beam. The identity of the higher order mode is determined by the image recorded by the CCD camera.

The HOM field components experience an effective frequency shift relative to the  $\text{TEM}_{00}$  carrier field due to the Gouy phase shift. The effective frequency shift is given by

$$(m + n)\eta = \pi \frac{\Delta f}{\text{FSR}} \mod \pi \quad (3.4)$$

where  $m$  and  $n$  are the  $\text{TEM}_{mn}$  mode indices,  $\Delta f$  is the frequency shift, and  $\eta$  is the Gouy phase shift, which is related to the cavity  $g$ -parameter by Equation 3.2.

Table 3.1 shows the measurements for several higher order mode frequency shifts. Notice that the horizontal and vertical modes experience slightly different Gouy shifts

$m$	$n$	$\Delta f$	$\eta$	$g$
0	1	-489.60 MHz	$0.2407\pi$	0.7275
1	0	-489.12 MHz	$0.2424\pi$	0.7238
0	4	267.96 MHz	$0.2407\pi$	0.7274
4	0	269.60 MHz	$0.2422\pi$	0.7242

Table 3.1: Higher order mode frequency shifts in the OMC. The frequency shift measured by varying the subcarrier separation from the resonating carrier. The  $m$  index is the horizontal mode order. Negative frequency shifts were achieved by using the -1 diffraction order of the AOM.

in the cavity. This is due to the astigmatism introduced in the cavity by non-normal incidence on the cavity mirrors. One may use the measured  $g$ -parameters to estimate the radius of curvature of the curved optics of the OMC. If we take the average value of the measured  $g$ -parameter, this implies a radius of curvature of 1.96m, which is close to the specification of 2m.

These data were taken with the OMC at room temperature. It was later discovered that the HOM spacing varied with the temperature of the thermal length actuator [49]<sup>6</sup>. With high enough temperature, this would bring the fourth order modes in coincidence resonance with the TEM<sub>00</sub> mode! We postulated that this was due to a change in the effective radius of curvature of the OTAS mirror as the OTAS expanded. To mitigate this, the temperature was kept low during operation.

### 3.3.3 Cavity finesse

The frequency profile of the transmitted peak when the subcarrier is shifted through resonance may be used to determine the cavity finesse. The finesse is defined as the ratio of the spacing between resonances (the FSR) to the full width at half maximum (FWHM) of the resonance. In the experiment, a sawtooth wave was used to sweep the subcarrier offset frequency while the OMC transmission was monitored. These signals were digitized and recorded. The recorded transmission versus frequency shift data are shown in Figure 3-8. The curve fit model used was Equation 3.1 with

---

<sup>6</sup>Note that all ilog references may be viewed publically with username *reader* and password *readonly*.



$\phi = \pi\Delta f/\text{FSR}$  and an arbitrary scaling and offset. The fitting parameters return a cavity finesse of  $367 \pm 2$ .

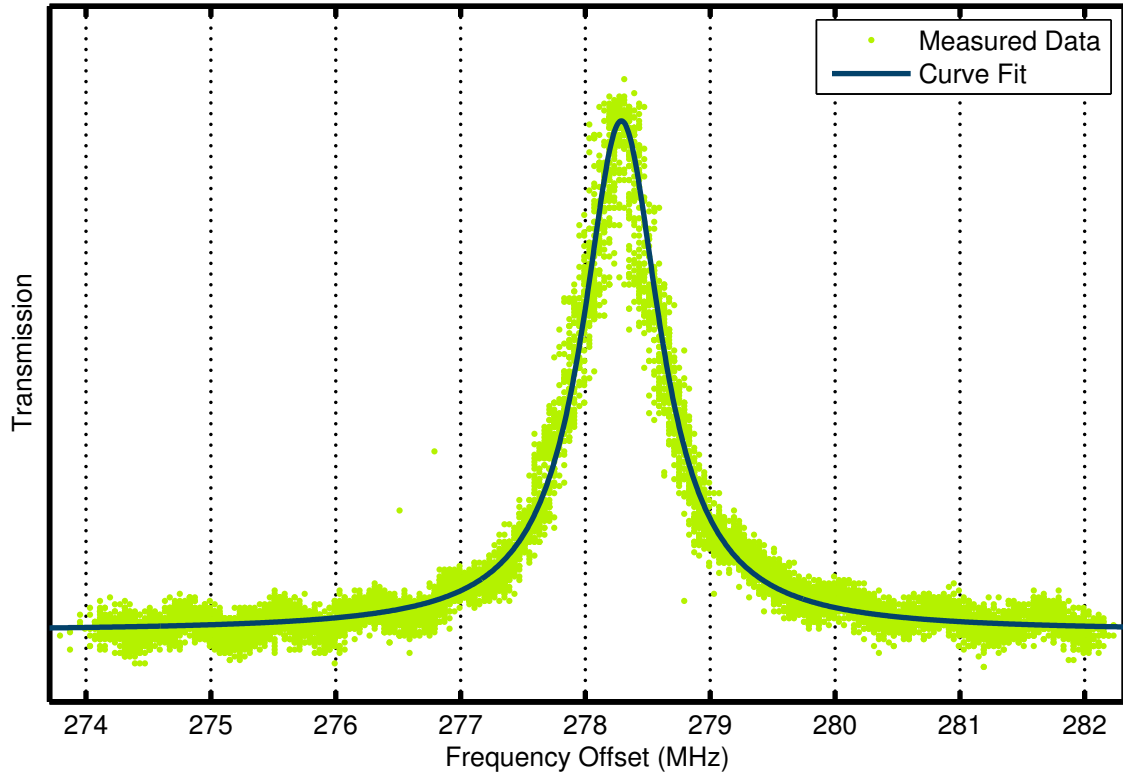


Figure 3-8: Measurement of the OMC transmission profile. The OMC is locked on the carrier, pictured is the transmission while varying frequency offset as the subcarrier passes through resonance. The width of the transmission peak is used to determine the cavity finesse. Fitted parameters give a finesse of  $367 \pm 2$ .

### 3.3.4 Cavity losses

The intra-cavity loss of the OMC was inferred by using three photodetectors; one measuring a sample of the input light, one measuring the reflected light, and one measuring the transmitted light, as seen in Figure 3-7. Both the reflection and transmission photodiodes were calibrated relative to the input diode. The calibration of the reflection diode was achieved by leaving the input and reflection diodes in place and blocking the beam inside the cavity. The relative power readings of the diodes were then recorded and the ratio gives the reflection calibration. One must also take

Input (V)	Reflection (V)	Transmission (V)	Transmission Efficiency
0.95	1.51	0.53	0.965
0.903	1.44	0.498	0.958

Table 3.2: Measurements of the OMC intra-cavity losses. All units are calibrated in Volts measured by the input PD.

into account the known transmission of the OMC input coupling mirror. This calibration is done without moving the beam to be used during the measurement and mitigates systematic errors due to variations in the sensitivity over the surface of the diodes. The transmission diode, however needed to be moved during calibration to measure the power incident on the cavity. The transmission diode was also calibrated relative to the input diode.

This technique measures the light incident on the cavity, reflected from the cavity, and transmitted by the cavity. Any incident light which is neither reflected nor transmitted is assumed to be absorbed and constitutes cavity losses. Table 3.2 shows the data taken to determine the cavity losses. The transmission efficiency is defined to be  $P_{\text{transmission}}/(P_{\text{input}} - P_{\text{reflection}})$ . The cavity transmission efficiency was measured to be approximately 96%.

In September 2010, during the Sixth LIGO Science run, it was discovered that the output efficiency of the H1 interferometer had somehow degraded to below 80%. After the end of the Science Run, this efficiency was determined to originate in the OMC. The cause of the degradation was that the position of the OTAS had become mechanically displaced. The reason of the displacement is not known but seems to have occurred simultaneously with a site wide power outage at the LIGO Hanford Observatory. The beam clearance of the OTAS was very tight and the displacement caused significant beam clipping, leading to losses in the OMC cavity [50].

### 3.3.5 PZT actuator response

The PZT length actuator of the OMC was calibrated by applying a voltage to the PZT to sweep the cavity through both carrier and subcarrier resonances. The sub-



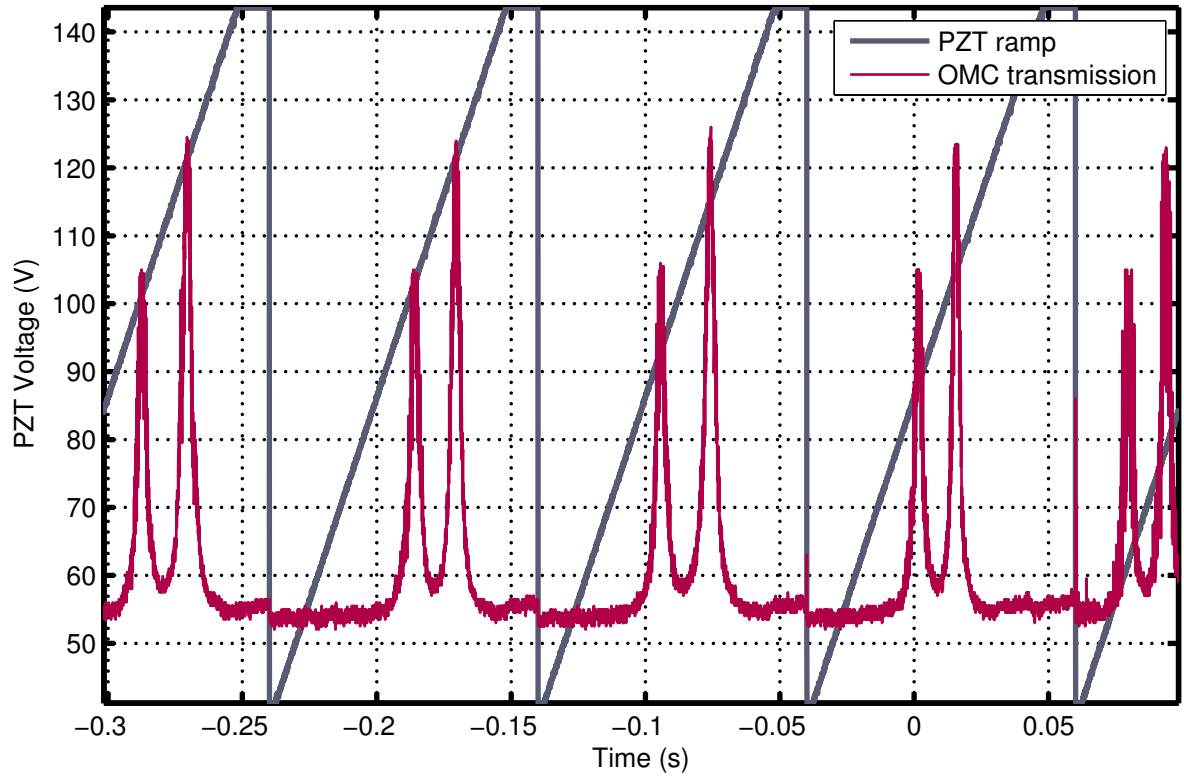


Figure 3-9: Measurement of the OMC PZT actuator calibration. Both the carrier and subcarrier can be seen passing through resonance.

carrier frequency offset was chosen to be close to one FSR separated from the carrier. The separation was 1FSR + 3.8MHz. In terms of a change in cavity length, this is 14.5nm, which is twice the distance moved by the mirror. Given the known frequency separation of the carrier and subcarrier, a determination of the voltage offset between resonances can be used to calibrate the PZT. The data taken are shown in Figure 3-9, and the mean offset of the central three ramps is 19.8V. Thus the PZT calibration is  $\frac{14.5\text{nm}}{2} \frac{1}{19.8\text{V}} = 0.37\text{nm/V}$ .

### 3.4 Optical feedback instability in the OMC

An issue arose during Enhanced LIGO which hindered the development of an automatic cavity locking system for the OMC. As the OMC was brought into resonance, some kind of dynamical instability would be activated and this would cause signals in

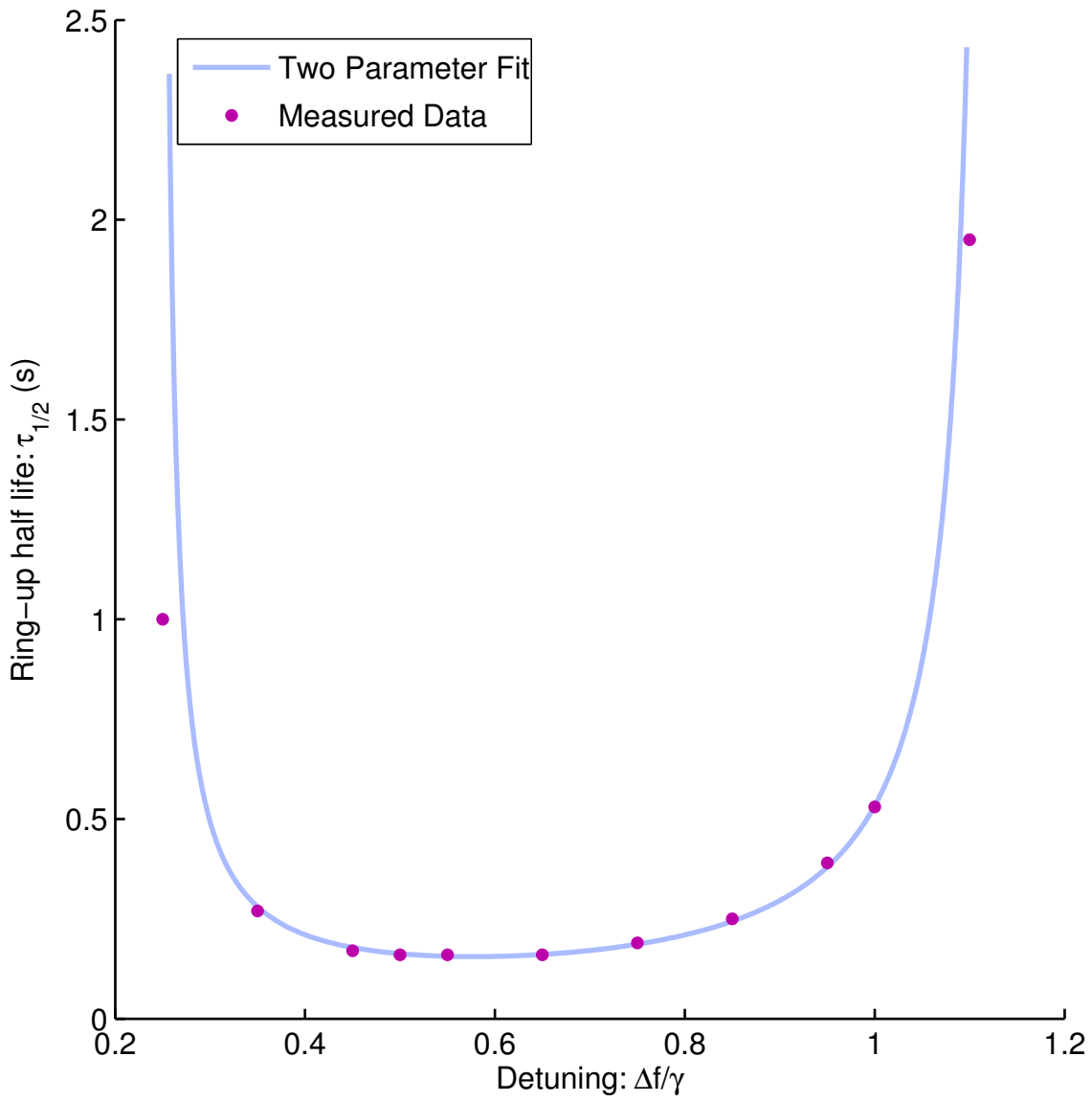


Figure 3-10: Measurement of ring-up times of optical instability in the OMC. The instability ring up time was measured for several values of the cavity detuning. Also plotted is a two-parameter curve fit to the data. Data collected by Tim Bodiya and Nicolas Smith-Lefebvre.



the transmitted power at kHz frequencies with amplitudes large enough to saturate the readout electronics. Because the locking servo was based on a transmission dither scheme, these instabilities would pollute the cavity length error signal and prevent locking. The instabilities would not be excited at the very peak of resonance, so for some fraction of the attempts, there would be a successful lock of the cavity. The result of this is that locking the OMC was the only step in the lock acquisition and low noise operation of Enhanced LIGO that was not fully automated during science data taking. The lack of an automatic OMC locking system probably had a detrimental effect on the overall duty cycle of the interferometers, but the magnitude of this effect would be difficult to determine.

The mechanism of the instability was never understood. It had the following characteristics:

- The strength of the instability depended on the circulating cavity power. for small power incident on the OMC (less than 1mW) there was no instability.
- The instability was not coupling through the PZT actuator. The instability remained even with the PZT leads were shorted.
- There was no instability when the cavity was centered on resonance.
- There was instability on either side of cavity resonance.

There was an attempt to quantify the behavior of this instability by investigating the dependence of the ring-up time of one of the unstable modes with a frequency of 1.1kHz. The OMC was locked detuned from resonance with approximately 9mW of power transmitted through the cavity. The data that were taken are shown in Figure 3-10 as the ring-up half life,  $\tau_{1/2}$ , as a function of cavity detuning,  $\Delta f/\gamma$ , where  $\gamma = \frac{1}{2} \frac{\text{FSR}}{\mathcal{F}}$  is the cavity linewidth.

Also shown in Figure 3-10 is a simple model of the ring-up time. The model comprises a exponential ring-up characterized by an anti-damping term which has

the following functional dependence on the detuning:

$$\Gamma(\Delta f) = \frac{2\Delta f/\gamma}{[1 + (\Delta f/\gamma)^2]^2}, \quad (3.5)$$

which is just the derivative of the cavity transmission profile (Equation 3.1) for small  $\Delta f$ . Explicitly, the ring-up half life is

$$\tau_{1/2} = \tau_0 \left( \frac{2\Delta f/\gamma}{[1 + (\Delta f/\gamma)^2]^2} - \Gamma_0 \right)^{-1}. \quad (3.6)$$

The best fit of the model to the data is given by  $\tau_0 = 33 \pm 6\text{ms}$  and  $\Gamma_0 = 0.438 \pm 0.001$ .

Perhaps the most interesting aspect about the model is what mechanism it rules out. An opto-mechanical parametric instability driven by radiation pressure would have a third factor of  $[1 + (\Delta f/\gamma)^2]$  in the denominator for Equation 3.5 [51]. A curve fit with a model consistent with a radiation pressure instability was also tried, but did not provide a good agreement with the data. So although it seems that the instability is somehow driven by the intra-cavity power, it is not consistent with radiation pressure.

Ultimately this did not pose a problem for the noise performance of the interferometer, because the OMC is always kept on resonance during normal operation, it is not operated detuned. However, it did remain a poorly understood feature of the system and because Advanced LIGO will use the same, or a similar OMC, it likely warrants further investigation.

### 3.5 OMC performance in Enhanced LIGO and prospects for future interferometers

The ultimate performance of the interferometer is affected by the OMC in several ways. The ability of the OMC to maximally transmit the gravitational wave signal directly affects the shot-noise limited SNR of the interferometer (this is covered in Section 5.1). Losses inside the OMC will limit the transmission, but these were shown



to be low (Section 3.3.4). A more subtle problem is to correctly match the incident beam to the resonant  $\text{TEM}_{00}$  mode of the OMC, any signal light which is not correctly matched will be rejected. From the point of the readout sensitivity, this is effectively a loss. The two most common forms of cavity mismatch are alignment (Chapter 5) and mode matching (Chapter 6). In addition to signal losses, the addition of an OMC can bring new noise couplings, perhaps the most important being the sensitivity to beam jitter (Chapter 7).

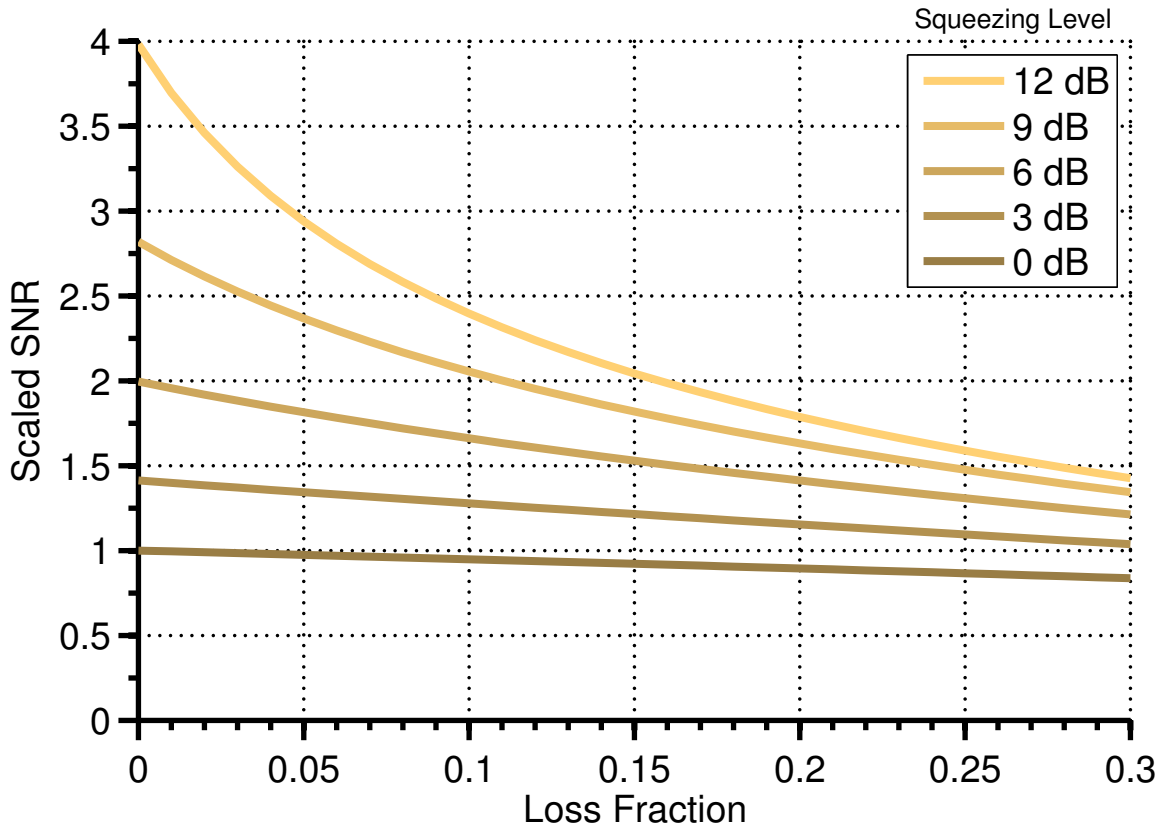


Figure 3-11: Interferometer readout SNR gain from squeezing as a function of output losses. Higher levels of squeezing lead to increased sensitivity to output losses, including those from the OMC.

An analysis of the readout sensitivity of the two Enhanced LIGO interferometers was performed by Fricke et al. [40]. This analysis showed that both interferometers performed at the expected level of sensitivity when all known output losses were taken into account. The OMCs thus provided the desired outcome of improving the ultimate

interferometer sensitivity. One of the major sources of loss for the H1 interferometer was mode mismatching, this was the motivation for the system proposed in Chapter 6.

The use of squeezed light to further enhance the readout sensitivity of laser interferometers has recently been demonstrated as both feasible and practical on full scale gravitational wave antennae [52, 53]. Output losses become even more important when the interferometer employs squeezed light injection. Figure 3-11 shows how losses in the readout chain can degrade the interferometer sensitivity for different levels of squeezed light injection. The prospects of squeezing for future interferometers certainly offer great promise for boosting interferometer sensitivity. Although, these benefits can only be fully exploited if the output losses are maintained at a minimal level. The performance of the OMC is central to realizing these goals.

The following chapter covers some theoretical background necessary for analyzing how the OMC interacts with the output beam of the interferometer.





# Chapter 4

## Vector space model of optical systems

This chapter describes a formalism that treats the laser field components propagating in an optical interferometer as a complex vector space where common optical components, such as mirrors and optical modulators are treated as operators in this space. This treatment allows the analysis of complicated optical paths, which include paths that loop onto themselves (as is the case of resonant cavities) to be reduced to a problem of matrix manipulation. This is a powerful technique that is used extensively in modeling the behavior of gravitational-wave interferometers [54–56], and is useful for some of the concepts discussed in later chapters.

At this point in the discussion, a bird's eye view of the technique is useful. In essence what this formalism provides is a significant abstraction and abbreviation of the effects of optical components (mirrors, modulators, etc.) on the field components that make up a laser beam. In the case of the transverse electric-magnetic (TEM) spatial modes of a laser field, a calculation of how a mirror, which is rotated about some axis perpendicular to the beam, redistributes energy from one field component to another may require complicated overlap integrals involving the Hermite-Gaussian profiles of the beam modes. Such a calculation is difficult to calculate and analytical solutions are intractable and unwieldy. The strength of this technique is that all of these complicated integrals are *baked in* to the linear operators which rep-



resent optical components, so to speak. All of the involved integral math is performed in the construction of the operators, and is hidden from view when the optical system as a whole is considered. What is left is just a problem of linear algebra.

## 4.1 Frequency components of a laser field

To get a flavor of the formalism, consider the simple example where we choose our vector space to just have three components that represent the amplitude of a carrier frequency field at frequency  $\omega_0$ , as well as two sideband fields separated in frequency by  $\pm\omega$ . Consider an electromagnetic wave propagating in the  $z$  direction, the electric field at  $z = 0$  may be written as

$$\begin{aligned}\vec{E}(t) &= A_0 e^{i\omega_0 t} \vec{x} + A_1 e^{i(\omega_0 + \omega)t} \vec{x} + A_{-1} e^{i(\omega_0 - \omega)t} \vec{x} \\ &= (A_0 + A_1 e^{i\omega t} + A_{-1} e^{-i\omega t}) e^{i\omega_0 t} \vec{x},\end{aligned}$$

where  $A_0$ ,  $A_1$  and  $A_{-1}$  are the carrier, first order upper sideband and first order lower sideband amplitudes respectively,  $k = \omega_0/c$  is the wave-number, and  $\vec{x}$  is the *geometrical* basis vector pointing along the axis of polarization. We are interested in the vector representation where this same propagating field is represented as<sup>1</sup>

$$|E\rangle \doteq \begin{bmatrix} A_0 \\ A_1 \\ A_{-1} \end{bmatrix}. \quad (4.1)$$

The basis vectors in this representation are given by the three periodically time varying components of the electric field, namely the carrier, upper and lower sidebands. It is important to emphasize that the vectors used in this formalism are in general not simple euclidean vectors, but rather abstract vectors representing different components of the electric field of an electromagnetic wave. The basis vectors are

---

<sup>1</sup>The use of  $\doteq$  in (4.1) is meant to convey that the expression on the right side is a representation of the vector on the left side in the chosen vector space. The right side of the equation is not written in terms of vectors and thus is not truly equal to the left side.

orthonormal, the inner product of two basis vectors is:

$$\langle r|s \rangle = \frac{1}{T} \int_{\text{many cycles}} dt (e^{i\omega_r t})^* e^{i\omega_s t} = \delta_{rs},$$

where  $\omega_r$  is the sideband frequency of the  $r$ th sideband, and  $T$  is the total integrated time, removed for normalization. This treatment is analogous to the formalism of quantum mechanics in which the quantum state of a system is defined by a vector in a space spanned by a set of orthonormal basis state vectors. In our formalism, the components of the laser field will take the place of the state vectors. We will use Dirac bra-ket notation because of this strong analogy.<sup>2</sup>

Now that we are familiar with using this vector space to represent the desired wave amplitudes, let us examine how we may use an operator to represent some optical component. An electro-optic modulator (EOM) can act as a phase modulator for a laser field when a voltage is applied. When a periodic signal is applied at frequency  $\omega$ , given an input field amplitude  $Ae^{i\omega_0 t}$  (ignoring the  $z$  dependence) the output amplitude is

$$Ae^{i\omega_0 t + i\Gamma \cos \omega t} \approx Ae^{i\omega_0 t} \left( 1 + \frac{i\Gamma}{2} e^{i\omega t} + \frac{i\Gamma}{2} e^{-i\omega t} \right), \quad (4.2)$$

where  $\Gamma$  is known as the modulation depth and is assumed to be small. One can show that in the example vector space we are considering, this EOM can be represented as the following operator

$$\Phi(\Gamma) \doteq \begin{bmatrix} 1 & \frac{i\Gamma}{2} & \frac{i\Gamma}{2} \\ \frac{i\Gamma}{2} & 1 & 0 \\ \frac{i\Gamma}{2} & 0 & 1 \end{bmatrix}. \quad (4.3)$$

It is then clear that the act of  $\Phi(\Gamma)$  operating on an input field constructed as the

---

<sup>2</sup>One significant difference between quantum mechanics and this formalism is that the quantum state vector of a system must always have unit length, to ensure the state has a probability of 1. The length of the vector in this formalism is just a field amplitude, and can take any value.



one used in (4.2) gives the desired output field:

$$|E_{output}\rangle = \Phi(\Gamma) |E_{input}\rangle \doteq \begin{bmatrix} 1 & \frac{i\Gamma}{2} & \frac{i\Gamma}{2} \\ \frac{i\Gamma}{2} & 1 & 0 \\ \frac{i\Gamma}{2} & 0 & 1 \end{bmatrix} \begin{bmatrix} A \\ 0 \\ 0 \end{bmatrix} = A \begin{bmatrix} 1 \\ \frac{i\Gamma}{2} \\ \frac{i\Gamma}{2} \end{bmatrix}. \quad (4.4)$$

So far, we have kept our example relatively simple. The vector space we have chosen represents only the first order sidebands generated on the carrier frequency. Also, we have only expanded the effect of phase modulation to terms linear in  $\Gamma$ . There is, however, no fundamental reason that the analysis cannot be extended to arbitrary precision. The number of components of the vector space can be expanded to account for an arbitrary number of higher order sidebands, and the matrix elements used for  $\Phi(\Gamma)$  can take their exact values. The general form of the phase modulation operator is:

$$\Phi(\Gamma) = \sum_{r,s=-\infty}^{\infty} |r\rangle i^{s-r} J_{s-r}(\Gamma) \langle s|, \quad (4.5)$$

where  $|r\rangle$  is the basis vector representing the  $r$ th order sideband component (which includes a  $e^{ir\omega t}$  time dependence), and  $J_k(x)$  is the Bessel function of the first kind.<sup>3</sup> The ability to calculate to arbitrary precision will continue to hold true when we expand the treatment to include other components of a propagating laser field, such as the transverse spatial modes. As long as the solutions are converging, the precision is only limited by the choice of when the vector space is truncated, i.e. to what order the calculation is taken.

## 4.2 The modal space

So far our example prescribes an elegant way to deal with optical components (e.g. the modulator) which transfer energy from one component of the electric field (the carrier) to other components (the sidebands). This type of approach is also applicable

---

<sup>3</sup>This can be shown using the so-called Jacobi-Anger identity,  $e^{ix \cos \theta} = \sum_{k=-\infty}^{\infty} i^k J_k(x) e^{ik\theta}$ . Also,  $J_{-k}(x) = (-1)^k J_k(x)$ , thus  $\Phi(\Gamma)$  is symmetric.

to the components of the electric field corresponding to the transverse spatial modes of the beam, as shown by Hefetz et al. [55].

When the paraxial approximation applies, it is possible to expand the electromagnetic field into a superposition of modes represented by a Gaussian function of the transverse coordinate, multiplied by polynomials. Common choices for the polynomial functions are the Hermite or Laguerre polynomials [33, Chap. 16]. This formalism associates the modal components with eigenmodes of what is described as the “perfectly aligned and undistorted optical path”. In other words, this formalism describes how the introduction of misalignments and beam distortions alter a laser beam propagating in the system by treating misalignments (or higher order beam distortions) as matrix elements which transfer energy between different spatial modes. The misalignments are generally treated as small, and thus, the operators of the optical components differ from the identity operator by small corrections. The misaligned solutions of beam propagation are thus treated as perturbations of the aligned solutions.

The treatment of modes in this formalism is slightly novel due to the fact that, normally, some fundamental Gaussian laser mode is defined to have a particular beam waist  $w_0$ , and a focused beam with a different beam waist can be written as a series of higher order components with the original beam waist  $w_0$ . In this formalism, the fundamental Gaussian mode may have a beam waist value that changes due to the presence of a lens, but the beam on both sides of the lens would be represented by the same modal state vector (modulo some phase rotation due to propagation). It is only the presence of misalignments and distortions that cause significant off-diagonal matrix elements.

Choosing the common Hermite-Gaussian basis, we can use basis vectors which are separable into the mode order of the beam along the  $x$  and  $y$  transverse axes of the beam. A general field vector can be decomposed in the modal space as

$$|E\rangle = \sum_{m,n=0}^{\infty} A_{mn} |mn\rangle \doteq \sum_{m,n=0}^{\infty} A_{mn} U_m(x, z) U_n(y, z) e^{-ikz}, \quad (4.6)$$



where  $U_m(x, z)$  is the  $m$ th 1-D Hermite-Gaussian mode (for example, as defined in Siegman [33].) The basis modes are also referred to as the Transverse Electric and Magnetic modes of order  $mn$  ( $\text{TEM}_{mn}$ ). The Hermite-Gaussian modes form a complete orthonormal set of basis functions, therefore the inner product is  $\langle mn|kl\rangle = \delta_{mk}\delta_{nl}$ .

In the modal space, a simple example operator would be a mirror that has been tilted by an angle  $\theta_x$  about the  $y$  axis. Due to the mirror misalignment, the phase of the beam at the plane of the mirror has been advanced on one side and retarded on the other side, relative to the aligned beam. This can be represented as a phase multiplication of  $\exp[-2ik\theta_x x]$ . Hefetz et al. [55] show that in the modal basis this is satisfied by the operator

$$\mathbf{M}(\Theta_x) = \exp \left[ -i2\Theta_x \sum_{m,n,k,l=0}^{\infty} |mn\rangle \delta_{nl} \left( \sqrt{k}\delta_{m[k-1]} + \sqrt{m}\delta_{m[k+1]} \right) \langle kl| \right], \quad (4.7)$$

where  $\delta_{mn}$  is the Kronecker delta; and  $\Theta_x = \theta_x \pi w(z)/\lambda$  is the normalized misalignment angle for beam width  $w(z)$  and wavelength  $\lambda$ . At the beam waist,  $\Theta_x$  is the ratio of the misalignment angle to the beam divergence angle. One can see that the  $k$  index is connected to the  $m$  index when they differ by one mode number, this will provide the correct transfer of energy from the  $\text{TEM}_{00}$  mode to the  $\text{TEM}_{10}$  mode as discussed above. We can use a matrix representation with three components representing the  $\text{TEM}_{00}$ ,  $\text{TEM}_{10}$  and  $\text{TEM}_{01}$  amplitudes, explicitly for field  $|E\rangle$ :

$$|E\rangle \doteq \begin{bmatrix} \langle 00|E\rangle \\ \langle 10|E\rangle \\ \langle 01|E\rangle \end{bmatrix} \quad (4.8)$$

In this representation,

$$\mathbf{M}(\Theta_x) \doteq \exp \left( -i \begin{bmatrix} 0 & 2\Theta_x & 0 \\ 2\Theta_x & 0 & 0 \\ 0 & 0 & 0 \end{bmatrix} \right) \approx \begin{bmatrix} 1 - 2\Theta_x^2 & -i2\Theta_x & 0 \\ -i2\Theta_x & 1 - 2\Theta_x^2 & 0 \\ 0 & 0 & 1 \end{bmatrix}. \quad (4.9)$$

The last approximation being valid for small  $\Theta_x$ .<sup>4</sup> So for small misalignments, the effect of rotating a mirror is to take energy from the TEM<sub>00</sub> component of the field, and transfer it to the TEM<sub>10</sub> component, the opposite also being true when the initial field already has a non-zero TEM<sub>10</sub> component. It is also useful to note that the resulting TEM<sub>10</sub> field has a quadrature which is rotated by  $\pi/2$  with respect to the initial TEM<sub>00</sub> field. Or in other words, the amplitude of the TEM<sub>10</sub> field is in the *phase direction* relative to the TEM<sub>00</sub> amplitude.

### 4.3 The combined vector space

To treat the general problem of laser fields propagating through an optical system, it will be useful to consider both frequency and modal components simultaneously. This combination was covered in detail by Sigg and Mavalvala [56].

Mathematically, the combined space is a tensor product of the spaces discussed above. The resulting basis vectors will be labeled by four indices, two from the modal space, one from the frequency space, and for completeness, a final index to represent the polarization. We can use the following notation for the basis vectors:

$$|mn; r; p\rangle = |mn\rangle_{\text{modal}} \otimes |r\rangle_{\text{frequency}} \otimes |p\rangle_{\text{polarization}}. \quad (4.10)$$

It is understood that the electric field represented by one of these basis vectors is

$$|mn; r; p\rangle \doteq e^{[i(\omega_0 + \omega_r)t]} U_{mn} \vec{\epsilon}_p,$$

where  $\omega_r$  is some mapping from the index  $r$  to a set of frequencies;  $U_{mn}$  is shorthand for  $U_m(x, z) \times U_n(y, z)$ ; and  $\vec{\epsilon}_p$  for  $p \in \{1, 2\}$  are the polarization unit vectors in the  $x$  and  $y$  direction, respectively. Note that this treatment handles sidebands slightly different from how they are handled elsewhere. For example, Sigg and Mavalvala [56] treat radio frequency modulation sidebands differently from audio frequency sidebands, and also only treat audio frequency sidebands which are regularly spaced. Using

---

<sup>4</sup>Note that  $\theta_x$  being small is also required by the paraxial approximation.



the treatment outlined here in which all sidebands are treated in the same way and may have arbitrary spacing, we are able to more simply investigate cross modulation products of several modulation sidebands, as well as situations where signal detection frequencies are comparable to modulation frequencies. This is accompanied by the sacrifice of potentially having many more matrix elements.

An example of an operator in the combined space is the free space propagation operator:

$$\mathsf{P}(\Delta z, \eta) = \sum_{\substack{mnkl \\ rs \\ pq}} |mn; r; p\rangle \delta_{mk} \delta_{nl} \delta_{rs} \delta_{pq} \exp \left[ i(m+n+1)\eta - i \frac{\omega_0 + \omega_r}{c} \Delta z \right] \langle kl; s; q|, \quad (4.11)$$

using parameters

$$\begin{aligned} \Delta z &= z_{\text{end}} - z_{\text{start}} \\ \eta &= \arctan \left( \frac{(z_{\text{end}} - z_0)\lambda}{\pi w_0^2} \right) - \arctan \left( \frac{(z_{\text{start}} - z_0)\lambda}{\pi w_0^2} \right) \end{aligned}$$

for starting and ending positions  $z_{\text{start}}$  and  $z_{\text{end}}$ , where  $z_0$  is the position of the beam waist,  $w_0$  is the beam radius at the waist, and  $\eta$  is the Gouy phase shift. As one can see by the presence of the Kronecker deltas in (4.11), all the components of the input field are directly propagated to the output field without mixing. There is, however a phase shift which depends on the transverse mode order (the Gouy shift) and the wavelength ( $\omega_r/c$ ).

More complicated operators exist which simultaneously mix mode and frequency components. One example is that of a mirror which is dithered at a given frequency in angle. It is in a sense a combination of the misaligned mirror operator in Section 4.2 and the phase modulation operator in Section 4.1. This operator is derived by Sigg and Mavalvala [56].

## 4.4 Photodetection

A photodetector is a device which is sensitive to the power in the laser field. This is typically a photodiode which converts the laser power into an electric current. In terms of the electric field we may write the time averaged power incident on a photodiode as

$$\bar{P} = \frac{\epsilon_0 c}{2} \int \frac{dt}{T} \int dA |E|^2 = \frac{\epsilon_0 c}{2} \langle E | E \rangle. \quad (4.12)$$

This fits nicely into our formalism because one can view the average power detected at a photodiode as the squared-norm of the state vector of the laser field. Often, however, one may use a photodetector to measure certain frequency components of the power, as well as information about the spatial distribution of the beam. Here we outline how to treat such signals in this formalism.

The time dependent components of the laser power can be thought of as the mixing of different frequency components of the electric field. To achieve this in the vector space formalism, we must use an operator which has matrix elements connecting different frequency components. For demodulation at frequency  $\omega_d$ , the operator takes the form:

$$D(\omega_d) = \sum_{rs} |r\rangle [\delta(\omega_r, \omega_s - \omega_d) + \delta(\omega_r, \omega_s + \omega_d)] \langle s|, \quad (4.13)$$

where we use a delta function defined as

$$\delta(\alpha, \beta) = \begin{cases} 0 & \text{if } \alpha \neq \beta, \\ 1 & \text{if } \alpha = \beta. \end{cases} \quad (4.14)$$

Note that there is a special case where  $\omega_d = 0$  where  $D(\omega_d)$  is the identity operator, which does not follow from Equation 4.13 and must be handled separately. Photodetectors are sometimes split into many segments, such as is the case with a so called quadrant photo-detector (QPD). In the case of a QPD, the face of the photodetector is split into four equal segments as seen in figure 4-1. Different linear combinations of the photocurrents of these segments can yield different information



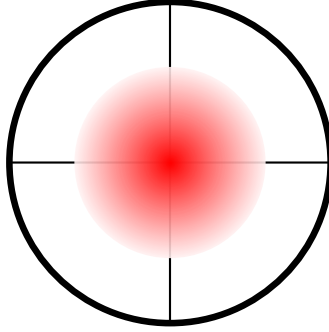


Figure 4-1: Diagram of a quadrant photodiode. The beam is pictured centered on the diode. As the beam is displaced vertically, more photocurrent will be measured by the top two segments than the bottom two. Subtracting the bottom photocurrents from the top ones will provide a measurement of the vertical beam position.

about the laser beam. For example, the vertical displacement of a beam can be determined by subtracting current of the top segments from the bottom segments.

The shape and linear combination of the photodiode segments is treated in the literature[55] as a pupil function  $p(x, y)$ , where the photodiode measures a signal

$$S = \frac{\epsilon_0 c}{2} \int dt \iint_{\text{PD area}} E^\dagger(x, y) p(x, y) E(x, y) dx dy, \quad (4.15)$$

so for example for a photodetector split along the  $y$  axis,  $p(x, y) = 1$  for  $x > 0$  and  $-1$  for  $x < 0$ .

In the language of transverse spatial modes, a split photodetector is measuring the mixing of the  $\text{TEM}_{00}$  mode with the  $\text{TEM}_{10}$  mode.<sup>5</sup> So in order to model this in the vector space framework, we will need to generalize the demodulation operator to have matrix elements between spatial modes as well as frequency components. So we may expand the demodulation operator to include spatial components. The spatial matrix elements of the demodulation operator are:

$$\langle mn | \mathbf{D}(\Omega) | kl \rangle = \iint_{\text{PD area}} U_{mn}^\dagger(x, y) p(x, y) U_{kl}(x, y) dx dy, \quad (4.16)$$

---

<sup>5</sup>More precisely, it measures the mixing of all even modes to odd modes and vice versa, with the primary contribution coming from the modes which differ by one mode order.

where the “variable”  $\Omega$  is just supposed to contain all the information of the pupil function.<sup>6</sup>

The frequency, spatial, and polarization parts of the demodulation operator are combined simply with a tensor product,

$$\mathbf{D}(\Omega, \omega_d) = \mathbf{D}(\Omega)_{\text{modal}} \otimes \mathbf{D}(\omega_d)_{\text{frequency}} \otimes \mathbf{I}_{\text{polarization}}, \quad (4.17)$$

where  $\mathbf{I}$  is the identity operator.

Once the demodulation operator is constructed, the signal amplitude at frequency  $\omega_d$  measured by the photodetector with segmentation  $\Omega$  is

$$S = \frac{\epsilon_0 c}{2} \langle E | \mathbf{D}(\Omega, \omega_d) | E \rangle. \quad (4.18)$$

In terms of the quantum mechanical analogy, the signal measured on a photodetector is just the expectation value of its demodulation operator.

## 4.5 Vector space model of the output mode cleaner

The true utility of this formalism arises when the optical system contains paths that branch and loop onto themselves, as is the case with resonant cavities. The fact that the operators can simultaneously handle the transverse modes and frequency components reduces much of the complexity of the problem through abstraction. In figure 4-2 we see a schematic diagram of a four mirror ring cavity. Every interaction of the laser field is handled by an operator. This includes transmission through an optic, reflection from an optic, and propagation through free space.

We may write down an expression for the field inside the cavity as follows

$$|E\rangle_{\text{cavity}} = \mathbf{T}_1 |E\rangle_{\text{input}} + \mathbf{G} |E\rangle_{\text{cavity}}. \quad (4.19)$$

Here,  $\mathbf{G}$  is the operator representing one full round trip through the cavity, starting

---

<sup>6</sup> $\Omega$  does not represent an angular frequency in this case.



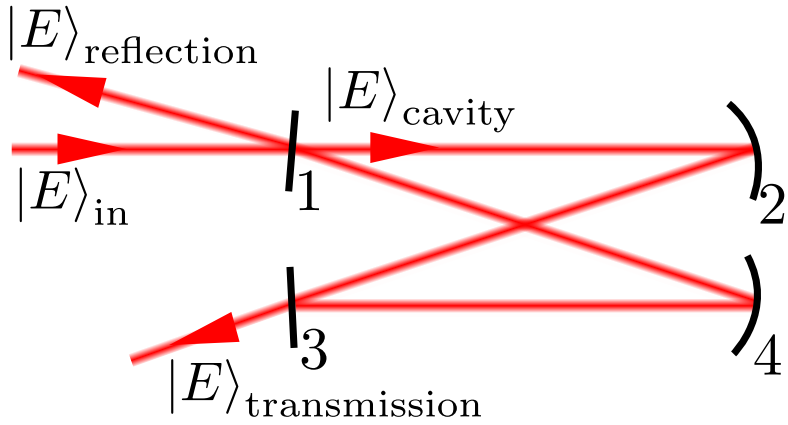


Figure 4-2: Diagram of vector space model of the OMC

with the propagation from mirror 1 to mirror 2,  $\mathbf{T}_1$  is the operator for transmission through mirror 1, and  $|E\rangle_{\text{cavity}}$ , is the cavity field due to the previous round trip of the light. When the system has reached a stationary state,  $|E\rangle_{\text{cavity}} = |E\rangle_{\text{cavity}}^*$ .<sup>7</sup> In this case we may solve for the field in the cavity:

$$|E\rangle_{\text{cavity}} = (\mathbf{I} - \mathbf{G})^{-1} \mathbf{T}_1 |E\rangle_{\text{input}}. \quad (4.20)$$

The round trip operator is

$$\mathbf{G} = \mathbf{P}_{1 \rightarrow 2} \mathbf{M}_2 \mathbf{P}_{2 \rightarrow 3} \mathbf{M}_3 \mathbf{P}_{3 \rightarrow 4} \mathbf{M}_4 \mathbf{P}_{4 \rightarrow 1} \mathbf{M}_1, \quad (4.21)$$

where  $\mathbf{P}_{j \rightarrow j+1}$  is the free space propagation operator from mirror  $j$  to  $j + 1$ , and  $\mathbf{M}_k$  is the reflection operator for mirror  $k$ .

By definition, the mirror operators are all diagonal when the system is aligned. Also the propagation operators are diagonal by construction. The diagonal matrix elements of  $\mathbf{G}$  vary in their phase from one field component to the next. Thus one can see that when these matrix elements have a phase close to an integer multiple of  $2\pi$ , the cavity field of those components will be enhanced. This is of course just the

---

<sup>7</sup>Note that this does not only include fields static in time, but also any periodically changing fields that are represented in our vector space.

expected resonance behavior. As the length of the cavity is changed (which modifies the propagation operators) different field components will come in and out of resonance. This includes both frequency components and higher order mode components, indeed different frequency components of different higher order mode components as well!

The following chapters build on the concepts introduced here.





# Chapter 5

## Optimal alignment sensing of an output mode cleaner

One surprise that arose from the Enhanced LIGO project was the difficulty of OMC alignment. During the project, it was learned that the very reason to desire an OMC, e.g. the presence of higher order mode (HOM) junk light, is also a source of contamination for a system to correctly align the laser beam into the OMC. This chapter describes what ultimately became the solution to that problem.

A critically coupled optical cavity can attenuate the HOM content of a laser beam. Such cavities also act as temporal filters for reducing laser amplitude and phase noise for frequencies above the cavity linewidth. When such mode cleaner filter cavities are placed at the output (readout) port of an optical system, deriving error signals to control the length and alignment of the Output Mode Cleaner (OMC) cavity poses a particular challenge. The signal-rich optical field may be weak compared to the HOM components.

In this chapter we describe a solution to the problem of aligning the OMC cavity. Though we consider the LIGO optical readout here, our scheme applies to any optical system where a signal is encoded as an amplitude modulation of a laser field, and the spatial mode of the signal-induced modulation sideband differs from that of the DC carrier field. In the case of LIGO, the signal is a gravitational wave induced modulation of the optical field, typically at frequencies 10 Hz to 10 kHz shifted from



the carrier.

## 5.1 The alignment problem in a mode cleaner cavity

Fig. 5-1 shows a schematic representation of the readout system we consider. The laser beam incident on the OMC comprises a carrier field and signal sideband fields which must be aligned to the OMC cavity. In the absence of technical noise sources, an automatic alignment system should maintain the cavity alignment that maximizes the SNR of the detected signal with respect to the photon shot noise. In general the carrier and sideband fields do not occupy the same spatial modes and their transmission through the OMC varies differently as a function of the input alignment.

As a simple example, consider a beam reflected from an over-coupled Fabry-Perot cavity (OC). The OC is held slightly offset from resonance such that periodic length excitations cause amplitude modulation that can be detected on a photodetector. Consider the case of a static misalignment of the input carrier field. The reflected carrier field will also be misaligned, while the signal field, being generated inside the OC, will be in the same spatial mode as the OC. Thus the carrier and signal fields will have a relative misalignment. In this example, the cause of the alignment mismatch is a misalignment of the input field to the OC. However, in more complicated cases, such as in the case of a LIGO detector composed of multiple, coupled cavities, the source of extra modal content may not be so easily removed.

Consider a carrier field with transmitted amplitude  $c$  and amplitude modulated upper and lower signal sidebands fields with transmitted amplitudes  $s$ . The shot noise limited SNR of the signal when measured on a photodetector is proportional to

$$SNR \propto \frac{cs}{\sqrt{c^2 + 2s^2}} \approx s. \quad (5.1)$$

Here we have made the following simplifying assumptions: the carrier field amplitude is much greater than that of the signal field, the signal fields are pure amplitude mod-

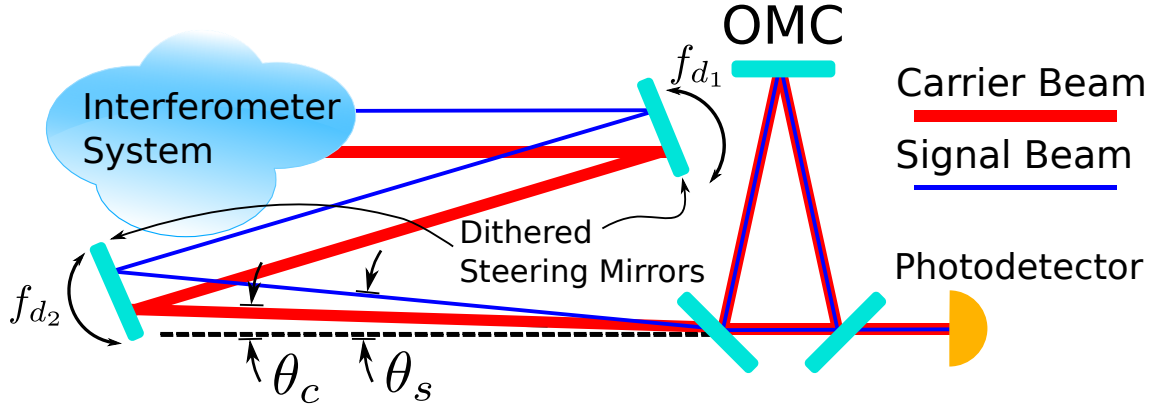


Figure 5-1: A signal is encoded by interferometry (or any other means) as an amplitude modulation of a laser beam. The beam is then steered by two mirrors which are dithered in angle before passing through a mode cleaner cavity. Alignment signals can be derived by demodulation of the transmitted photocurrent. The misalignment has been grossly exaggerated in the figure.

ulation, and that there is perfect spatial overlap of the carrier and the sidebands after transmission through the OMC. We see that the alignment system that maximizes optical SNR of fields detected after transmission through an OMC simply maximizes the amplitude transmission of the *signal field* through the OMC. In considering SNR, this chapter only considers shot noise. Another important noise source involved with OMC alignment is beam jitter noise, described in Chapter 7.

To leading order, typical alignment schemes sense the  $\text{TEM}_{01}$  and  $\text{TEM}_{10}$  modes of the carrier field measured in the the OMC eigenmode basis[57]. The presence of these modes is interpreted as a misalignment. In this chapter we will show how to modify a common alignment technique to be sensitive to signal field misalignments, and thus allow one to maximize the SNR of the signal.

Consider a single alignment degree of freedom where misalignments of the carrier and the signal fields are represented by one set of misalignment angles  $\theta_c$  and  $\theta_s$ . Dither alignment sensing is commonly achieved by mechano-optical modulation of an angular degree of freedom, e.g by driving steering mirrors that direct the beam into the OMC, as shown in Fig. 5-1. Each mirror is dithered in angle with constant amplitude at a given frequency to modulate the input pointing into the cavity.

Figure 5-2 shows the frequency content of the field transmitted through the OMC.



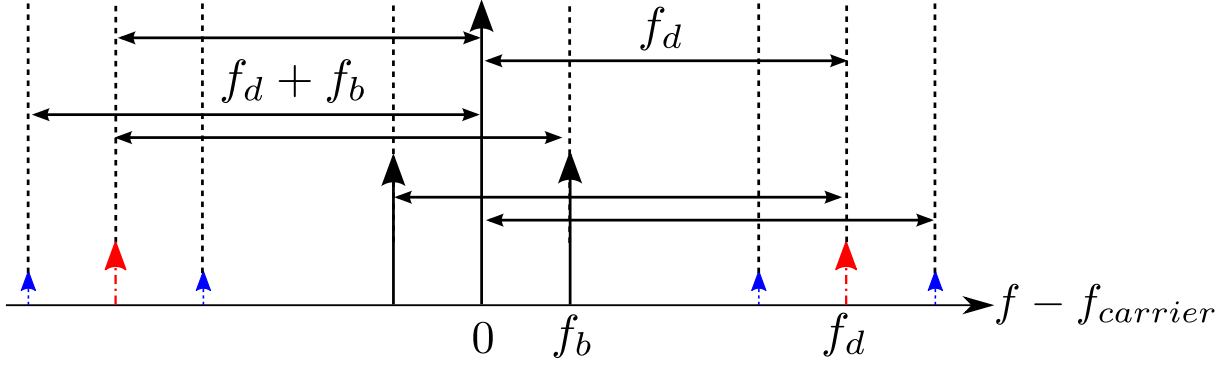


Figure 5-2: Arrow diagram showing electric fields after transmission through the OMC. In the figure,  $f_d$  is the angular dither frequency,  $f_b$  is the beacon modulation frequency.

The carrier field is separated in frequency from two amplitude modulated signal sideband fields at  $\pm f_b$ . The dithering steering mirror produce two sidebands at  $\pm f_d$ , with a field amplitude proportional to  $\theta_c$  (alternatively, the TEM<sub>01</sub> mode amplitude [56, 57]). The signal field also has dither sidebands proportional to  $\theta_s$ . The demodulated signal is made of products of field amplitudes separated by the demodulation frequency.

We will use the notation  $P(f)$  to represent the OMC transmitted photocurrent demodulated at the frequency  $f$ . We define the standard dither alignment signal as

$$S_{standard} = P(f_d) \propto 2c^2\theta_c + 4s^2\theta_s \approx 2c^2\theta_c, \quad (5.2)$$

where  $c$  is the carrier field amplitude,  $s$  is the signal field amplitude. For the case where the carrier power is much greater than the signal field power ( $c^2 \gg s^2$ ), the demodulated alignment signal is sensitive only to misalignments of the carrier field.

*In this scheme the error signal is nulled at an alignment where the total transmitted cavity power is maximized.* We will refer to this as the *standard dither scheme*.

## 5.2 “Beacon” alignment sensing

To better sense the alignment of the signal field one may create a large amplitude modulation of the signal, say by modulating the length of the signal cavity. This modulation creates a frequency tag of the spatial mode of the signal field. We refer to this as a “beacon” modulation, and  $f_b$  is the modulation frequency.

As in the standard dither scheme, steering mirrors are used to dither the angle of the beam. The desired error signal in this scheme is produced by demodulating the transmitted power at  $f_d + f_b$  or  $f_d - f_b$ , or the sum of these signals. We define the beacon alignment signal as

$$S_{\text{beacon}} = P(f_d + f_b) \propto 2sc\theta_c + 2cs\theta_s. \quad (5.3)$$

When this error signal is nulled, the SNR is improved in comparison to standard dither, but sensitivity to the carrier field remains, so the SNR will not be maximized. Because the beacon modulation is small,  $S_{\text{beacon}}$  will have a higher relative noise level than the standard dither approach.<sup>1</sup>

## 5.3 Experimental Demonstration of Beacon Alignment Sensing

The beacon alignment scheme was compared directly to a standard dither scheme using the OMC cavity at the output of the 4 km LIGO Interferometer at Hanford (H1). The readout was arranged as in Fig. 5-1. The angular dither frequencies were between 1.5 and 2.5 kHz, while the beacon modulation was a 10 Hz excitation of the differential arm length.

The differential arm length of the interferometer is sensed as an amplitude modulation at the output port. The static carrier at the antisymmetric port is generated by an offset of the differential arm length. The OMC filters the spatial and frequency

---

<sup>1</sup>This is a statement about the noise in the alignment signal itself, however *using* this as the alignment error signal will improve the SNR of the gravitational-wave channel.



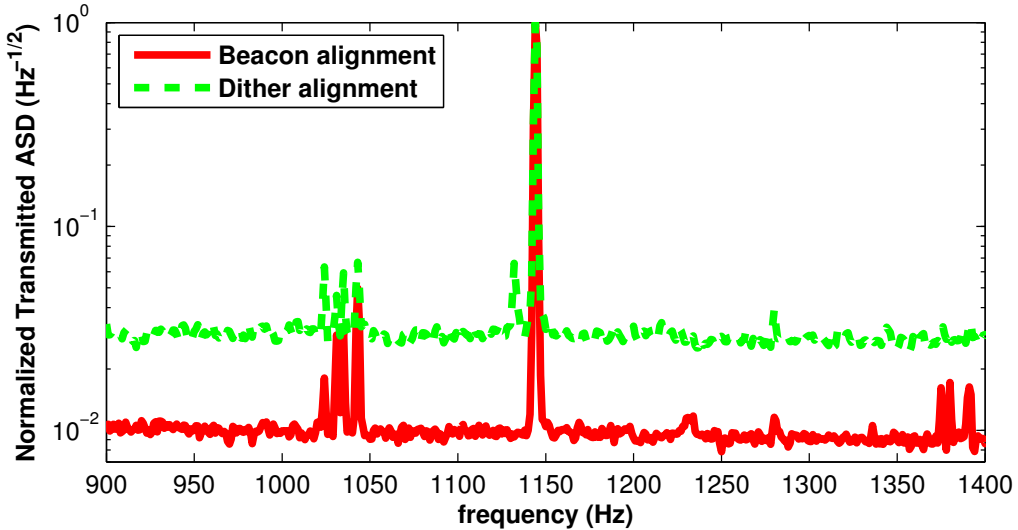


Figure 5-3: The noise amplitude spectral density of the LIGO H1 detector using two types of alignment schemes. The curves are normalized to a calibration line at 1144 Hz. The small line structures are resonances of the suspension wires supporting the mirrors. The beacon scheme shows an SNR improvement of about a factor of 3.

content of the beam before the beam is split equally and detected on two photodetectors. The LIGO interferometers are examples of optical systems where a beacon based alignment system performs significantly better than a standard dither scheme.

Fig. 5-3 shows the amplitude spectral density of the transmission of the OMC of the H1 interferometer. The plot is centered on an injected calibration signal at 1144 Hz and the curves are normalized to the peak height of this line. The calibration line is surrounded by primarily shot noise. The dashed green curve shows the performance using dither sensing, while the solid red curve shows beacon sensing. The SNR of the calibration line is improved by about a factor of 3.1 by using a beacon scheme. A factor of 2.4 is due to an increase of signal strength and the remaining factor of 1.3 is due to a reduction in the total transmitted power, and hence the shot noise. We propose that the poor performance of the standard technique is due to excess HOMs in addition to the TEM<sub>01</sub> mode associated with misalignment.

## 5.4 Optimal alignment sensing of the signal sideband field

It is possible to combine the standard dither signal with the beacon signal to produce a signal which is sensitive to signal field misalignments only. We also make use of the DC transmitted power,  $P_{DC} = P(0) \approx c^2$ , and the beacon modulation amplitude,  $P(f_b) \approx 2cs$ . An optimal alignment signal can be constructed as follows:

$$\begin{aligned} S_{optimal} &= S_{beacon} - \frac{P(f_b)}{2P_{DC}} S_{standard} \\ &\propto 2cs\theta_s + 2sc\theta_c - \frac{2cs}{2c^2} (2c^2\theta_c) \\ &\propto 2cs\theta_s. \end{aligned} \tag{5.4}$$

An alternative (though mathematically equivalent) technique would be to just make a dither servo which maximizes the optical SNR directly. This may be a more desirable approach depending on how signals are read out and if digital processing is possible. In this approach, the SNR should be calculated in real time and demodulated at the dither frequency to provide the error signal.

As above, if the beacon amplitude on the photodetector is  $P(f_b)$  and the DC power is  $P_{DC}$ , the optical SNR is

$$SNR = \frac{P(f_b)}{\sqrt{P_{DC}}}. \tag{5.5}$$

Any dither sensing scheme is essentially measuring the partial derivative of a signal with respect to the dithered degree of freedom (See Section B.2) [58]. Thus, a dither servo which maximizes the SNR will measure a signal proportional to

$$\frac{\partial}{\partial\theta} \left( \frac{P(f_b)}{\sqrt{P_{DC}}} \right) = \frac{1}{\sqrt{P_{DC}}} \left( \frac{\partial P(f_b)}{\partial\theta} - \frac{P(f_b)}{2P_{DC}} \frac{\partial P_{DC}}{\partial\theta} \right), \tag{5.6}$$

which is equivalent to (5.4) up to constant factors. This also shows that this signal is nulled at maximum SNR.



In gravitational-wave detectors, the OMC transmission is often held constant by a control system. If  $f_d$  is within the control bandwidth, but  $f_b$  is not, then the carrier alignment sidebands will be suppressed. Sufficient suppression makes the beacon scheme approximately equivalent to the optimal scheme. This was the configuration used by both the L1 and H1 interferometers in the sixth LIGO science run [40], discussed in Section 5.6.

## 5.5 Generalization of optimal signal-sideband alignment to other alignment sensors

The technique of using a beacon modulation to sense misalignment of the signal field can be generalized to other types of alignment sensors, for example: split quadrant photodetectors detecting light picked off the beam entering the OMC or split quadrant detectors in reflection of the OMC coupled with frequency or length dithered sidebands, also known as wavefront sensors.

We define the standard carrier alignment signal as  $G_{standard}$ . We also define another signal, demodulated  $f_b$  away from the standard signal, as  $G_{beacon}$ .  $P_{DC}$  and  $P(f_b)$  are defined as in (5.4). The generalized signal is:

$$G_{optimal} = G_{beacon} - \frac{P(f_b)}{2P_{DC}} G_{standard}. \quad (5.7)$$

We emphasize that the  $G$  signals are derived from the alignment sensor, while the  $P$  signals are derived from the OMC transmission.

## 5.6 Optimal beacon performance in Enhanced LIGO

The optimal beacon alignment scheme was employed in Enhanced LIGO by using low frequency angular dithers on the Tip Tilt optics. The angular dithers had a magnitude on the order of microradians, and frequencies of 1-5Hz. The beacon signal was produced by exciting the elastic drum-head vibrational mode of one of the end mir-

rors.<sup>2</sup> The frequency of the mode was 9225 Hz and it was excited to give an effective cavity length modulation of  $2.1 \times 10^{-14}$  m. On the OMC transmission photodetector, this was a relative intensity noise (RIN) of  $2 \times 10^{-5}$ .

Data were taken to directly compare the performance of the optimal beacon to a standard dither alignment scheme under typical conditions in Enhanced LIGO [59]. The data show that while using standard dither, the interferometer had a signal transmission of 95% when compared to the optimal dither scheme. From this we may estimate the ratio of the magnitude of the misalignment of the carrier field with respect to the signal field. The transmission efficiency may be written as

$$\epsilon = 1 - \alpha^2, \quad (5.8)$$

where  $\alpha$  is the ratio of the amplitude of the misalignment mode to the TEM<sub>00</sub> mode. In the case of  $\epsilon = 95\%$ ,  $\alpha = 0.23$ .

The standard dither signal simply chooses a local maximum of the transmitted power. This can sometimes be quite far from the optimal signal location if there are significant side lobes on the beam, as seen in Section 5.3. The measurement given in this section was first optimized with the optimal beacon alignment, then handed over to the standard dither scheme. This allowed the standard dither scheme to choose a local maximum which happened to be fairly close to the true signal maximum.

## 5.7 Chapter Summary

To summarize, we have introduced the concept of using a beacon as a strong modulation close to signal frequencies to generate alignment signals that lead to increased SNR compared to the standard dither scheme. The beacon scheme demonstrates a factor of 3 improvement in SNR for the LIGO H1 detector. Finally, we propose a detection scheme to give optimum SNR when used to align an OMC or filter cavity.

The following chapter discusses mode matching, which is the next order problem,

---

<sup>2</sup>First proposed by M. Evans.



after alignment, of coupling the output light of an interferometer into an OMC.

# Chapter 6

## Output mode cleaner mode matching feedback control

In interferometers such as LIGO, the power circulating in the resonant optical cavities can reach levels where even small levels of absorption induce deformations and refraction index changes due to deposition of thermal energy [60]. The effects of thermal lenses can be mitigated using compensation techniques that induce a negative thermal lens by heating the optics with a ring pattern, though some mode deformation remains [61].

Thermal distortions of the resonant mode of the interferometer cause a reduction of the coupling efficiency of the laser source to the interferometer mode. To mitigate the effect of input efficiency there have been efforts to adaptively modify the mode of the input beam using optical elements with variable focusing power. Coupled with a sensor to measure the amount of modal mismatch of the input beam, one may construct a servo to optimize the input mode matching and maximize the coupling efficiency [62–64].

A similar situation arises if the readout chain of the interferometer includes an output mode cleaner (OMC). The OMC is located between the interferometer and the photodetector measuring the gravitational wave signal, as shown in Figure 6-1. Here again, as the resonant mode of the interferometer is modified due to thermal lensing, the coupling efficiency of the output beam to the OMC degrades. In the



recently completed Enhanced LIGO phase of the Laser Interferometer Gravitational-wave Observatory, for example, the mode matching efficiency of the interferometer output beam to the OMC was found to vary between 89%, and 93%, due to changes in the thermal state alone [65]. Because the final gravitational wave signal is measured after transmission through the OMC, a reduction of transmission efficiency of the signal field through the OMC will result in a reduction of the signal-to-noise ratio (SNR). Degradation of the SNR is greatly amplified when the interferometer employs squeezed light injection [52].

In addition to mode mismatch due to a variable thermal state of the interferometer, there are other practical reasons to desire a remote controlled mode matching solution. When the OMC was first introduced to the LIGO interferometers, during the Enhanced LIGO phase [40], it was found that accurately setting up a mode matching telescope in a large vacuum system is a difficult and onerous process. Beam profiling equipment is usually not designed for low contamination environments and air currents present while the vacuum system is open make working with suspended optics and cavities complicated.

This chapter proposes a mode matching servo system for the *output* of the interferometer, similar to schemes proposed for the beam located at the input of the interferometer [62, 64]. It should provide a more tractable solution to OMC mode matching for upcoming second-generation gravitational wave detectors such as Advanced LIGO and its partner observatories, not only by allowing a softer requirement on exact placement of telescope components, but more importantly, by allowing for a mode matching solution that adapts to the thermal state of the interferometer.

## 6.1 A feedback control system for mode matching

The goal of the control system is to correct for deviations of the beam incident on the OMC from the  $\text{TEM}_{00}$  mode as defined by the basis of resonating modes of the OMC. In the case of mode matching, we are generally concerned with the  $\text{TEM}_{20}$  and  $\text{TEM}_{02}$  modes in the Hermite Gaussian basis. In this basis, the  $\text{TEM}_{20} + \text{TEM}_{02}$

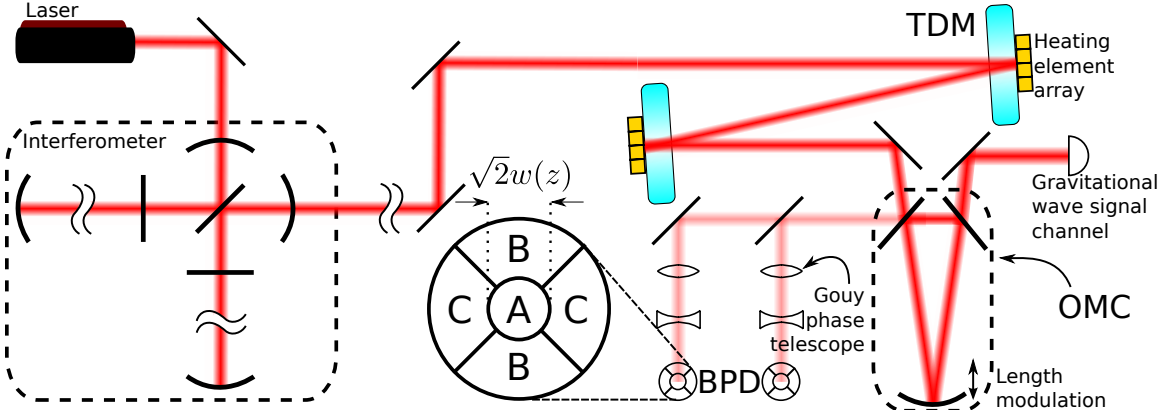


Figure 6-1: Schematic diagram of the optical layout of a mode matching feedback control system. Abbreviations are explained in the text. Also shown is the segmentation of the bull’s-eye photodetector. The spherical mode mismatch signal combination is A-B-C. The astigmatic signal combination is B-C.

mode represents a spherical mode mismatch, which we refer to as the *bull’s-eye mode*, while the  $\text{TEM}_{20} - \text{TEM}_{02}$  mode represents astigmatism [55]. The  $\text{TEM}_{11}$  mode represents astigmatism where the ellipse is oriented  $45^\circ$  from vertical, and can also be controlled with further subdivision of actuator and sensor segments, though this is not discussed in this chapter. Collectively, we refer to these modes as *second-order modes*, visualizations of these modes may be seen in Appendix B.5. In addition, each of these modes is composed of a real and imaginary quadrature. For the bull’s-eye mode, the two quadratures correspond to changes of the beam waist size and beam waist position along the optic axis, respectively. It is, therefore, useful to regard the control system in terms of its sensitivity to and actuation of the degrees of freedom composed of the complex amplitudes of the various second-order modes.

The sensors considered here can only measure a single quadrature of a given mode. In order to measure both quadratures, it is necessary to use two sensors. The complex phase rotation of higher order modes with respect to the  $\text{TEM}_{00}$  mode is proportional to the mode order due to the Gouy phase shift. Thus, in order to rotate the quadrature of the second-order modes by the optimal  $90^\circ$ , one must separate the sensors by  $45^\circ$  in Gouy phase (See Appendix B.1). A similar argument holds for the actuators.



A schematic diagram of the sensing and actuation system is shown in Figure 6-1. The control system consists of two actuators, two sensors and the resonant optical cavity. The actuators are focusing elements with variable focal length; astigmatism control is provided with the ability to induce differing focusing power in the vertical and horizontal directions. The laser beam is directed through both actuators and then incident on the input of the cavity. The cavity is critically coupled so the correctly matched light is transmitted maximally through the OMC. The cavity length is held on resonance by a separate control system. The reflected light is directed onto the two mode matching sensors, with Gouy phase telescopes to get good separation of sensed mode quadratures.

## 6.2 Mode matching sensors

The sensors are annular segmented photodetectors, also known as bull's-eye photodetectors (BPDs) [64]. A schematic of the BPD is shown as a part of Figure 6-1. The mode mismatch is sensed using a heterodyne detection scheme. Detection of the bull's-eye mode is done by subtracting the photocurrent of the central segment from those of the outer segments.

BPDs have been used in a variant of the Pound-Drever-Hall (PDH) scheme where the optical local oscillator was provided by radio frequency (RF) sidebands induced on the input beam by a frontal modulation scheme [64]. We propose to use an alternative scheme similar to ones used in alignment sensing. Such a scheme uses the sidebands induced by length modulation of the cavity for use in a dither servo for length control [66]. In Enhanced LIGO, the OMC length modulation frequency was approximately 12kHz. These sidebands leak out of the cavity from the reflected port and occupy only the  $\text{TEM}_{00}$  mode of the cavity. This provides a good local oscillator which mixes with the second-order modes due to the segmented photodetector. The error signal from the BPD is demodulated at the cavity length modulation frequency which provides a signal proportional to the mixing of the  $\text{TEM}_{00}$  cavity mode with the rejected second-order modes of the input beam. By contrast to PDH, the demodulation occurs at

Symbol	Value
$\mathcal{F}$	370
$k$	$2\pi/(1064\text{nm})$
$\delta z$	5pm
$P_c$	100mW
$P_{RF}$	500mW

Table 6.1: Parameters used to calculate the sensitivity of the BPD.

audio frequencies rather than RF.

The signal on the BPD, measured in power at the OMC length modulation frequency, is [56, 67]

$$S = \sqrt{2} \left( \frac{2}{e} \right) \left( \frac{2\mathcal{F}}{\pi} \right) (k\delta z) P_c \alpha, \quad (6.1)$$

where  $e$  the base of the natural logarithm,  $k$  is the wave number of the laser light,  $\delta z$  is the amplitude of the OMC length modulation,  $\mathcal{F}$  is the OMC cavity finesse,  $P_c$  is the power in the resonant carrier field incident on the OMC, and  $\alpha$  is the ratio of amplitudes of the bull's-eye mode to the TEM<sub>00</sub> mode incident on the OMC. Equation (6.1) assumes that the sensor is located with the optimal Gouy phase shift for the given mode mismatch.

In Advanced LIGO, the DC optical power on the BPD sensor will likely be dominated by RF sidebands exiting the interferometer which are rejected by the OMC. These RF sidebands provide sensing of auxiliary degrees of freedom of the interferometer, but are not relevant for the OMC sensing. The shot noise is then

$$N = \sqrt{2\hbar ckP_{RF}}, \quad (6.2)$$

where  $P_{RF}$  is the optical power of the RF sidebands,  $\hbar$  is the reduced Planck constant, and  $c$  is the speed of light in vacuum.

Using values from Table 6.1, we get a shot noise limited SNR of

$$SNR = \frac{S}{N} \sqrt{T} = 1.6 \times 10^6 \alpha \sqrt{\frac{T}{1\text{s}}}, \quad (6.3)$$



where  $T$  is the measurement integration time. For a 0.1% mode mismatch,  $\alpha$  takes a value of approximately 0.03. This amount of mode mismatch would have a shot noise limited SNR of approximately 500 with a  $10^{-4}$ s integration time. This value is sufficiently high that only a fraction of the OMC reflected power will be necessary in practice.

This design would optimize the transmission of the central optical carrier frequency through the OMC. In practice, the sensitivity to gravitational-waves depends on the transmission of audio signal sidebands which in principle could occupy differing spatial modes. The amount of mismatch of the carrier and audio sidebands that will be present in an interferometer is difficult to predict. As discussed in Chapter 5, in the first generation of LIGO, automatic alignment systems were developed which optimally sensed the audio sideband mode because the mismatch proved a problem for traditional alignment systems [40, 68]. Similar mismatch of the bull's-eye mode would contaminate a mode matching servo such as that described here. A solution would involve using the modulation product of the OMC length modulation sidebands with audio sidebands induced in the interferometer arms. These induced sidebands are commonly referred to as the beacon sidebands. This would give a corresponding reduction of SNR by the modulation depth of the beacon sidebands.

### 6.3 Mode matching actuators

While Arain et al. provide an array of optical elements which can provide a variable focusing power [62], for our OMC mode matching servo we propose the use of a design by Canuel et al. for use in mode matching control of the Virgo input optics system [69]. Canuel et al. propose a thermally deformable mirror (TDM) comprising a highly reflective (HR) mirror placed in reverse from the usual orientation, such that the beam passes through the anti-reflective surface and mirror substrate before reflection of the HR surface. An array of electronically resistive elements are bonded to the HR surface of the optic. Passing current through these resistive elements heats the optic and allows control of the transverse spatial variation of the optical path

length, which can be used to induce a thermal lens. A fine enough array of elements allows for heating patterns that can control the spherical and astigmatic lens powers separately. Canuel et al. report on an early prototype made from a BK7 substrate which can provide a variable focusing power with a range of  $0.032\text{m}^{-1}$ (diopters). The design of Canuel et al. has certain beneficial features which make it suitable for this application: it is vacuum compatible, it is low noise due to the low thermal time constant, and it is simple to modify existing suspended steering mirror designs to accommodate the heating elements. The control bandwidth will be limited by the thermal time constant of these actuators, which should be adequate given that the effects being corrected occur either at thermal time scales or are constant in time.

We may quantify the effect of a perturbation of the focusing power of an optical component by how much of a pure  $\text{TEM}_{00}$  mode is transferred to the bull's-eye mode for small variations in the focusing power. We will assume a system which is well mode matched in the absence of perturbation. Given an optical element with additional focusing power  $d_{\text{mm}}$ , the resulting mode mismatch amplitude is

$$a_{\text{bull's-eye}} = -i \frac{kw^2(z)}{4} d_{\text{mm}} \times a_{00} \equiv -i D a_{00}, \quad (6.4)$$

where  $k$  is the wave number of the laser beam,  $w(z)$  is the beam width radius measured at the optic position,  $a_{00}$  is the  $\text{TEM}_{00}$  mode amplitude, and  $a_{\text{bull's-eye}}$  is the bull's-eye mode amplitude [67].  $D$  can be interpreted as the beam-normalized focusing power, with  $d_{\text{mm}} = (d_v + d_h)/\sqrt{2}$ , where  $d_h$  and  $d_v$  are the focusing powers in the horizontal and vertical directions, respectively. To account for the astigmatic mode, one may define  $d_{\text{ast}} = (d_v - d_h)/\sqrt{2}$  and use a similar equation to that of Equation (6.4).

The light which is not in the  $\text{TEM}_{00}$  mode is rejected by the OMC, thus for the regime where  $D$  is small, the mode matching efficiency of the OMC is

$$\epsilon \approx 1 - D^2. \quad (6.5)$$

Assuming a design similar to that of Canuel et al. can provide 0.05 diopters focusing power, and a beam width radius of 2mm on the mirror, such an actuator would be



able to compensate a single quadrature of mode mismatch of up to approximately 10%. It should be noted that the actuation range depends quadratically on the beam size so larger values should be readily achievable.

## 6.4 Chapter summary

In summary we have provided a conceptual design for a mode matching control system to be used in interferometric gravitational-wave detectors that make use of an OMC. We have shown that segmented photodetectors and deformable mirror actuators originally conceived for the controlling mode matching *into* the interferometer are also well suited for solving the *output* mode matching problem. Moreover, we have adapted a modulation scheme designed to control the alignment of the interferometer output mode to the OMC to also yield high SNR mode matching error signals. Together, this has allowed us to propose a remotely controllable mode matching servo system. The necessity of having such a system was recognized during the commissioning and operation of the Enhanced LIGO detectors, and it will be an important tool for optimizing and maintaining the sensitivity of future gravitational wave detectors, including those of Advanced LIGO and Virgo.

The following chapter covers beam jitter noise, one of the most important sources of noise related to the use of an output mode cleaner in the readout chain of an interferometer.

# Chapter 7

## Techniques for reducing output mode cleaner beam jitter noise

When using an OMC in the readout of an interferometer, probably the most important new source of noise to arise is beam jitter. A related form of beam jitter noise also exists in the arm cavities of an interferometer [70]. Fluctuations of the output beam are, however, not generally an issue with an interferometer that does not use an OMC, so long as the beam apertures are always sufficient to prevent beam clipping.

An OMC may perform very well as a spatial filter for unwanted higher order modes, but simultaneously it becomes very sensitive to pointing fluctuations of the input beam. The GEO600 OMC which was tested by LIGO was placed outside of vacuum, and beam jitter noise ruined the sensitivity in most of the measurement band. It was for this reason that the Enhanced LIGO OMC was placed in vacuum [44]. Even with this improvement, much time and effort was spent by the commissioning teams in Enhanced LIGO to locate and remove sources of beam jitter noise. This Chapter will cover much of what was learned regarding beam jitter noise during the commissioning of Enhanced LIGO.



## 7.1 The noise mechanism of beam jitter incident on a high finesse cavity

Motion of the beam incident on a high finesse cavity alters the overlap of said beam with the resonant mode of the cavity. This leads to fluctuations in the amount of light which can couple into the cavity and consequently, power fluctuations of the transmitted beam. The power fluctuation can spoil the measurement of the intrinsic amplitude modulation of the beam if the measurement and fluctuations occur at the same frequencies.

For a beam incident on the cavity which has a lateral (perpendicular to the direction of propagation) and angular misalignment, constrained to a plane, we have the following expression for the power transmitted through the cavity

$$P \approx P_0 \left( 1 - \left( \frac{\Delta x}{w_0} \right)^2 - \left( \frac{\theta}{\theta_d} \right)^2 \right), \quad (7.1)$$

where  $P_0$  is the power transmitted of the aligned beam,  $\Delta x$  is the beam waist displacement,  $\theta$  is the beam waist tilt,  $w_0$  is the beam waist radius, and  $\theta_d$  is the divergence angle of the beam. The approximation holds while both the angular and lateral misalignments are small.

Equation 7.1 shows that beam misalignments couple to the transmitted power quadratically. This leads to a few relevant consequences. The coupling of beam jitter to transmitted power is nonlinear, thus frequency components of the beam motion may be mixed together, producing new frequencies in the transmitted power. Also, the linear coupling coefficient of beam jitter to power fluctuations is proportional to the DC beam misalignment. This causes the direct linear coupling of frequency components of beam jitter to power fluctuations to vary as the DC pointing error varies.

Steering optics in the beam path leading to the cavity which are vibrating may transfer vibrations to the laser beam and produce beam jitter noise. Let us investigate beam jitter coupling of an optic in the modal picture. We will work in a basis of only

the  $\text{TEM}_{00}$  and  $\text{TEM}_{01}$  modes. Let's assume we have a beam which is dominantly in the  $\text{TEM}_{00}$  mode as measured in the basis of our cavity, with some small amplitude of  $\text{TEM}_{01}$  mode. In other words, we begin with a beam which is slightly misaligned.

$$|E\rangle_{\text{input}} = E_0 (|00\rangle + \alpha |01\rangle). \quad (7.2)$$

The misalignment,  $\alpha$  may be due to another steering mirror upstream, or a misalignment of the beam source relative to our cavity axis, the precise origin is not critical for this discussion.

Now we will assume this beam is incident on a steering mirror before it finally enters the cavity. This steering mirror also has a slight misalignment,  $\theta$ . Equation 4.9 shows the matrix representing the operator of a mirror which has been tilted from nominal alignment. The beam incident on the cavity is then

$$|E\rangle_{\text{incident}} = \mathbf{M}(\Theta) |E\rangle_{\text{input}}, \quad (7.3)$$

where, as before,  $\Theta = \frac{\theta \pi w(z)}{\lambda}$ , while  $w(z)$  is the beam width radius at the mirror, and  $\lambda$  is the laser wavelength. Because the cavity has a high finesse, when the cavity is resonant on the  $\text{TEM}_{00}$  mode, only that mode is transmitted. Thus, for the field transmitted by the cavity

$$E_t = t_{\text{cavity}} \langle 00 | \mathbf{M}(\Theta) | E \rangle_{\text{input}} = t_{\text{cavity}} E_0 \left( 1 - i \frac{2\pi w(z)}{\lambda} \theta \alpha \right), \quad (7.4)$$

where  $t_{\text{cavity}}$  is the amplitude transmission of the cavity. This causes a power fluctuation on transmission

$$P = E_t^* E_t = P_0 \left( 1 + \frac{4\pi w(z)}{\lambda} \theta \text{Im}(\alpha) \right), \quad (7.5)$$

where  $P_0 = |t_{\text{cavity}} E_0|^2$ . To first order, only the imaginary part of  $\alpha$  contributes to beam jitter noise of our mirror because it represents an error in alignment *angle*, not position, at the location of the steering mirror  $\mathbf{M}$ .



One interesting consequence of Equation 7.5 is that for a given mirror, the strength of beam jitter coupling is proportional to  $w(z)$ , the size of the beam on the optic. Thus one technique for reducing beam jitter coupling is to design one's optical path in such a way that beams are smaller on optics that may produce significant beam jitter. This of course also reduces their efficiency as an alignment control mirror.

Furthermore, we again see a nonlinear coupling in the form of mixing of the incident misalignment,  $\alpha$ , and the jitter of the steering mirror,  $\theta$ . We may suppose that the input alignment has both a DC component and possibly some low frequency (a few to several Hz) wandering motion. If this is coupled with high frequency (i.e. frequencies in the detection band) jitter of the steering mirror, the mixing of frequencies can cause noise in the power transmission at and around the jitter frequency of the steering optic.

With the introduction of the OMC in Enhanced LIGO, bilinear beam jitter coupling became a much more prominent source of noise. Figure 7-1 shows how low frequency beam motion mixes with high frequency jitter to produce broad sidebands around beam jitter peaks. This is similar to how beam jitter was discussed by Fricke et al. [40].

The bilinear nature of beam jitter can be exploited when trying to determine the source of noise peaks in the OMC transmitted spectrum. If one injects a low frequency modulation into the angular control of a steering mirror in the path leading to the OMC, any peaks that originate from beam jitter will produce corresponding sidebands, separated by the central peak frequency by the injected modulation frequency. This can be used to quickly identify noise peaks as originating from beam jitter, though it does not determine the exact mechanism causing the beam jitter.

## 7.2 Mechanical resonances of beam steering optics

When the Enhanced LIGO interferometers were first performing at a sensitivity comparable to the state of the interferometers in the S5 science run, there were large glaring peaks in the sensitivity spectrum. It was determined fairly quickly that these

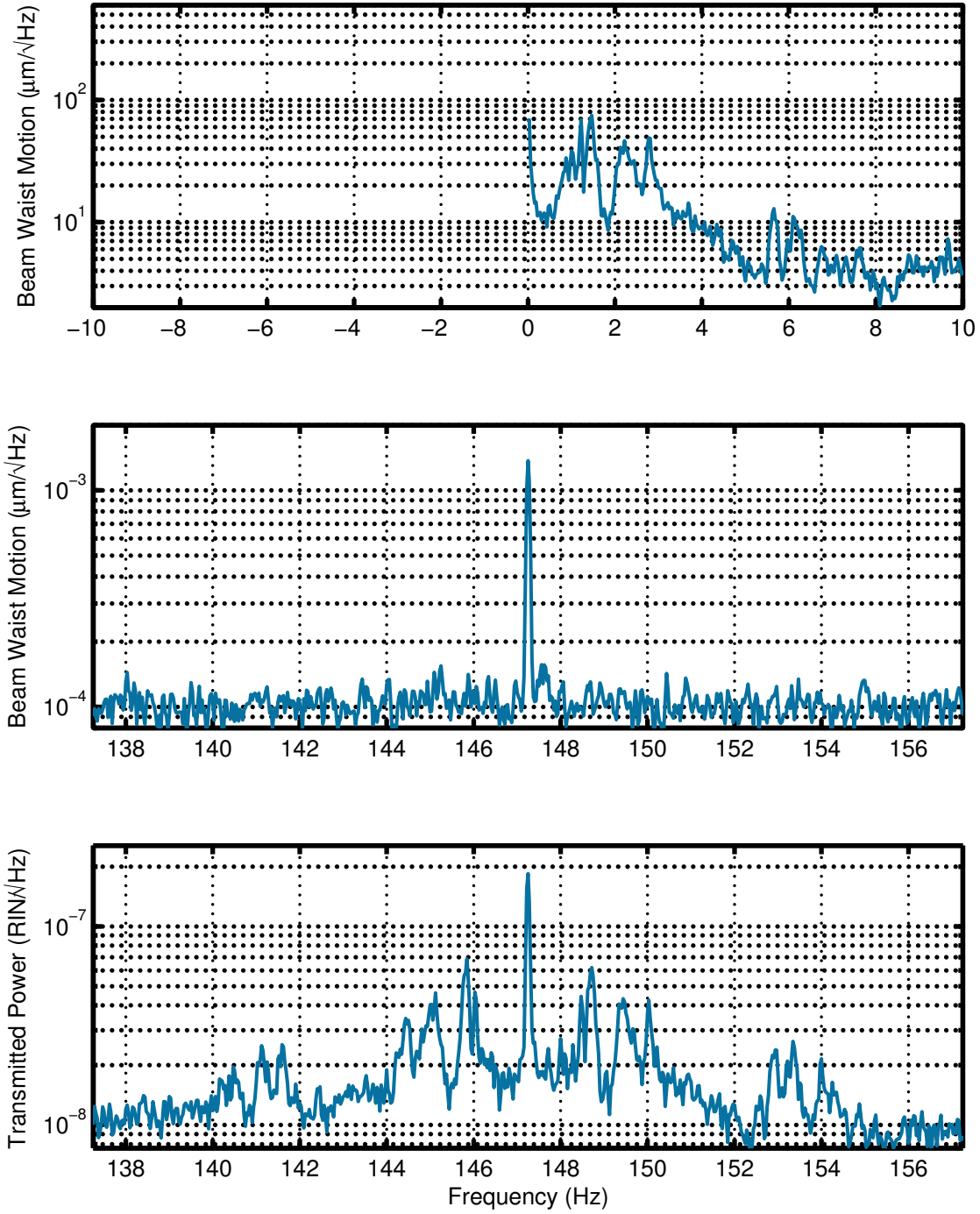


Figure 7-1: Measurement of the bilinear coupling of beam jitter noise. The top panel shows low frequency beam motion measured by the OMC input QPDs. Shown in the center panel is an audio frequency beam jitter peak, this peak was shown to arise from a vacuum scroll pump outside of the HAM6 chamber [71]. The bottom panel shows how the low frequency motion has been imparted as sidebands on a central beam jitter peak in the OMC transmitted light.



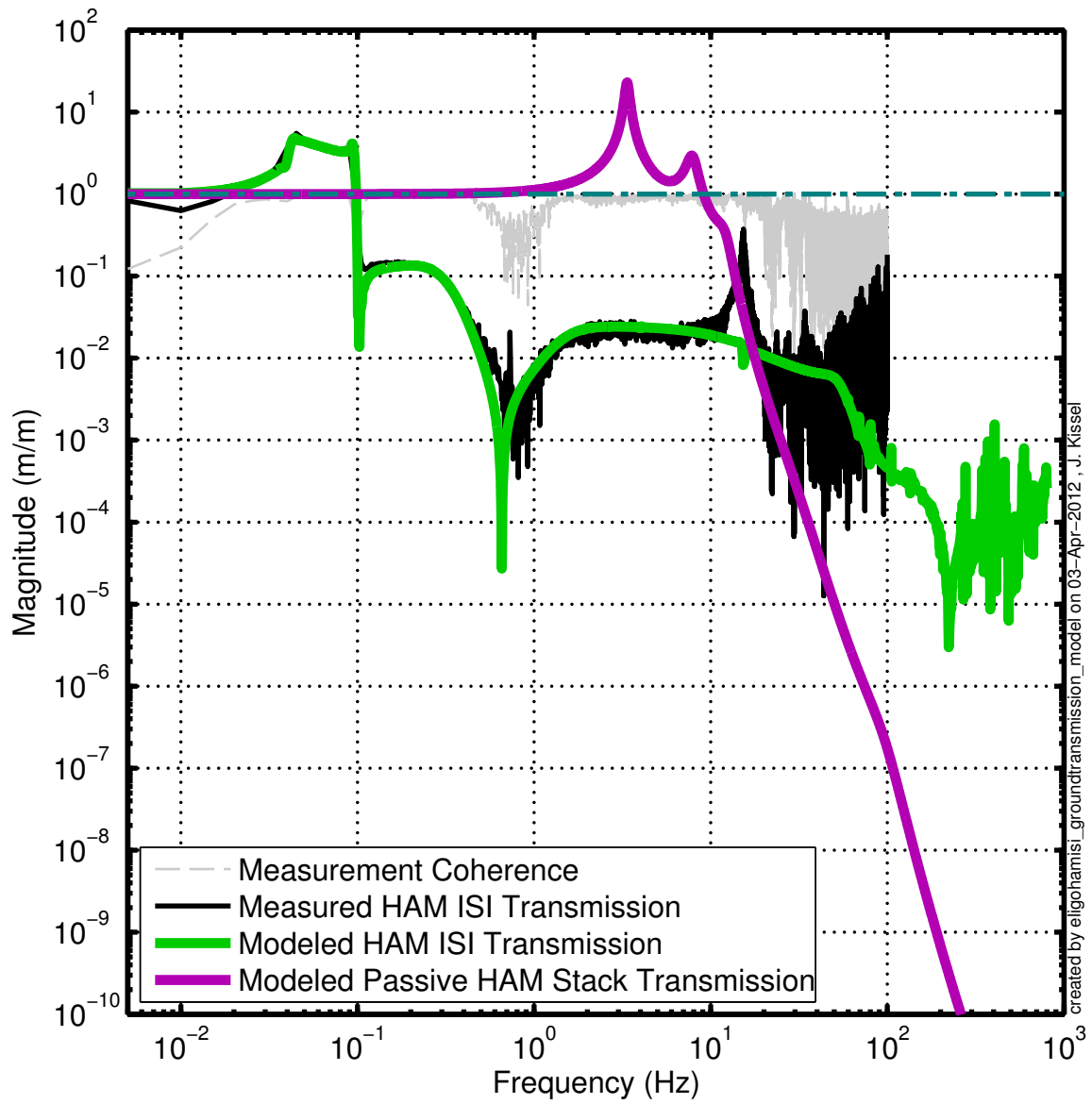


Figure 7-2: Comparison of vertical vibrational motion transmission of the Initial and Enhanced LIGO HAM chamber isolation systems. While the low frequency isolation of the HAM ISI is far superior to that of the old passive stack, in the most sensitive region of the interferometer (100-200Hz), the HAM ISI transmits a few orders of magnitude greater than the passive system. The high frequency behavior of the HAM ISI model (green curve) represents true resonant structure and is not a result of measurement noise. Credit and appreciation for this figure goes to Jeff Kissel.

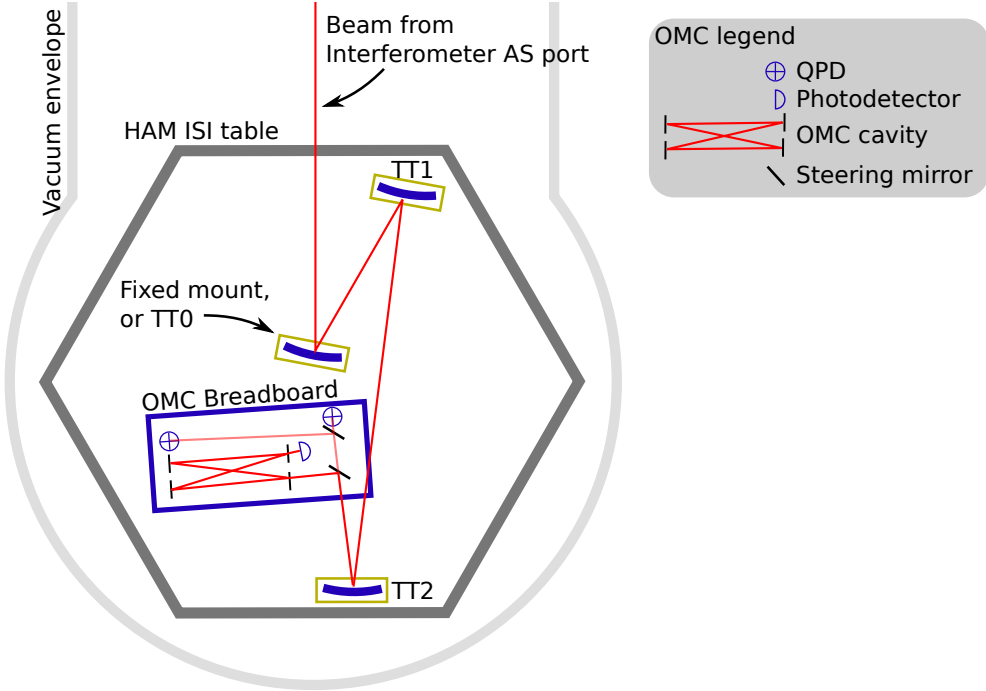


Figure 7-3: Schematic of HAM6 optical layout. The beam which exits the interferometer antisymmetric port is directed by three steering mirrors onto the OMC. The first steering mirror was originally a fixed post, and changed later to a passive suspended Tip Tilt optic. The second and third Tip Tilts were known used for active beam steering control. A small fraction of the light incident on the OMC transmits through a highly reflective steering mirror and is sensed by two quadrant photodetectors.

were due beam jitter, but the mechanism causing the jitter was unknown.

The Enhanced LIGO upgrade introduced several modifications to the readout chain of the interferometer. As discussed in Chapter 3, with the introduction of the in-vacuum OMC, it was necessary to use new beam steering and mode matching optics to couple the beam exiting the interferometer to the OMC cavity. A diagram of the optical layout is shown in Figure 7-3. These steering optics, as well as the OMC, were all housed in a single vacuum chamber on top of the prototype HAM ISI platform which is planned to be used copiously in Advanced LIGO. The new isolation platform provided much reduced vibration isolation at audio frequencies when compared to the isolation tables used in the HAM chambers in Initial LIGO. Figure 7-2 shows a comparison of the transmission of ground motion to motion of the HAM table for both the initial LIGO passive isolation system, and the Enhanced



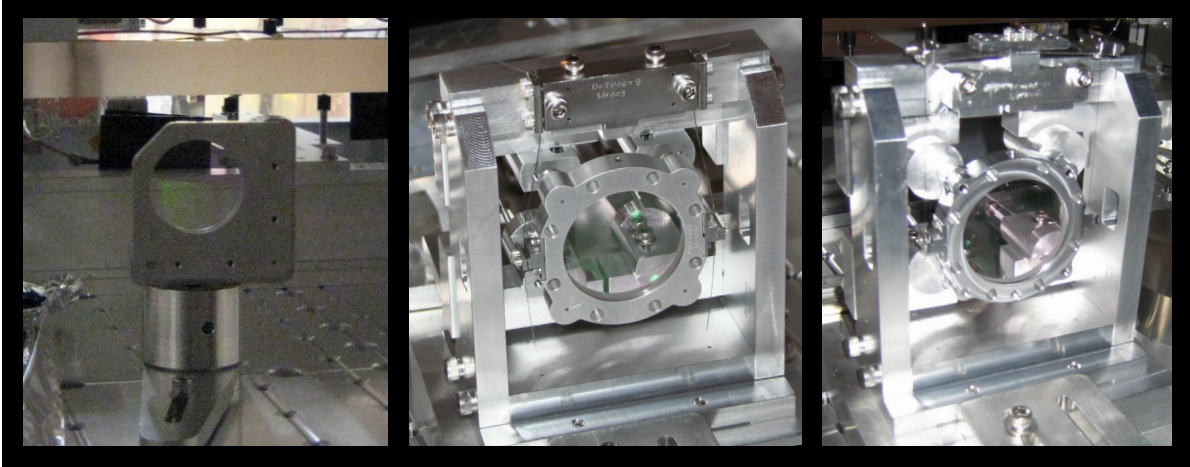


Figure 7-4: The evolution of the passive Tip Tilt. These photos show several stages in the configuration of the first mode matching/steering mirror used in HAM6. The original design was an optic mount attached to a fixed post, shown in the left panel. This was later changed (shown in center panel) to a passively suspended version, made by University of Florida, designed by M. Meyer at LIGO Livingston based on the original active Tip Tilt design. The right panel shows a further re-design where the upper suspension wire clamps are attached by blade springs to the suspension cage.

## LIGO HAM ISI.

The optical layout of the OMC chamber of Enhanced LIGO comprised three steering optics, which also behaved as a mode matching telescope, and the OMC itself. In the initial configuration, the first of these was a mirror on a fixed mount, while the other two were in a Tip-Tilt suspension system with active beam steering. Diligent work by Robert Schofield determined that some of the largest beam jitter peaks degrading the interferometer sensitivity were due to vibrations of the fixed mirror mount [72]. To rectify this situations, the fixed mirror mount was replaced with a small mirror suspension similar to the Tip Tilts but without the active steering control. Comparison of the old and new designs are shown in Figure 7-4. This new style was referred to as the passive Tip Tilt, or TT0. As seen in Figure 7-7, this was effective at removing the largest peaks, though some new peaks appeared in the 150-200Hz region.

The origin of the peaks located in the most sensitive region of the LIGO sensitivity

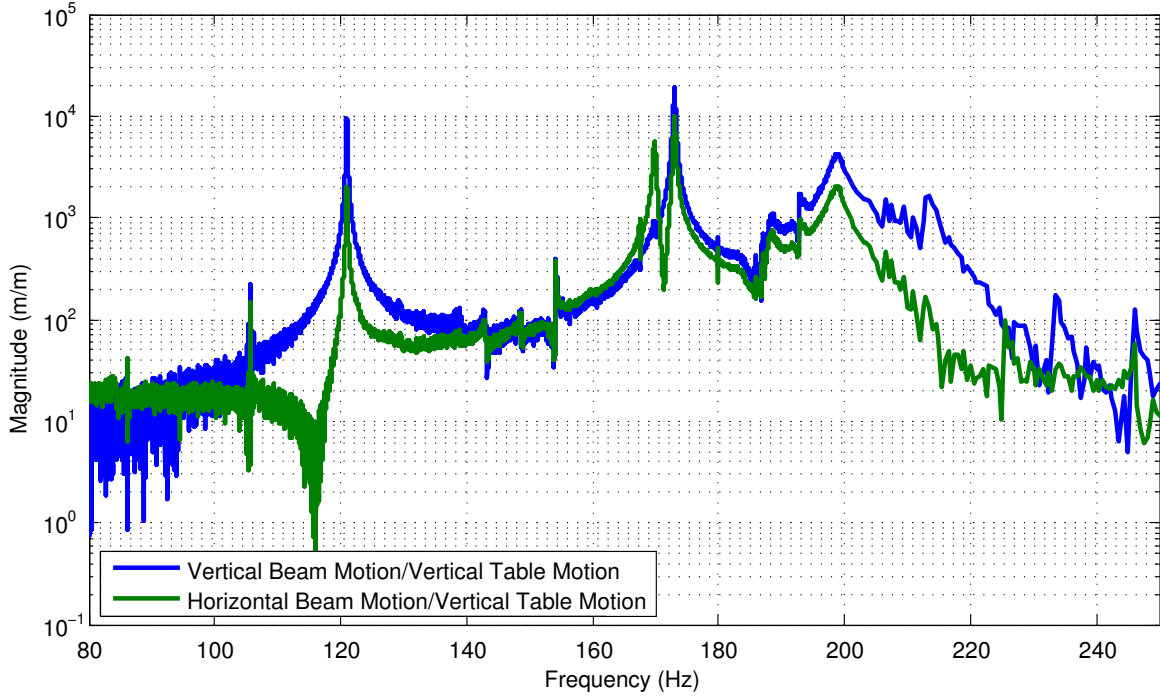


Figure 7-5: Measurement of HAM table motion coupling to beam motion. This measurement was performed while all three Tip Tilts used thick suspension wires and no blade springs. This measurement provided evidence that it was the optics on HAM6 which were causing beam jitter peaks in the sensitivity curve of the interferometer.

spectrum (“the bucket”) was finally determined by a measurement of the coupling of motion from the table to the pointing of the laser beam itself. The OMC was equipped with a pair of quadrant photodetectors (QPDs) which sampled the beam incident on the OMC. These QPDs were used to measure the response of the beam motion to motion of the ISI table, which is measured by inertial sensors built into the table. A measurement of the transfer function of table motion to beam motion may be seen in Figure 7-5. The resonances were determined to be the bounce (vertical) and roll (rotation about the beam axis) modes of the Tip Tilt optics [73]. In fact, at the resonant peaks, the motion of the beam was amplified by factors of  $10^3$  to  $10^4$  relative to the table motion!

The Tip Tilt design had originally assumed the vertical restoring force was due only to stretching tension in the wires. The vertical resonance was expected to lie near the 340Hz violin resonances of the main interferometer test mass suspensions.



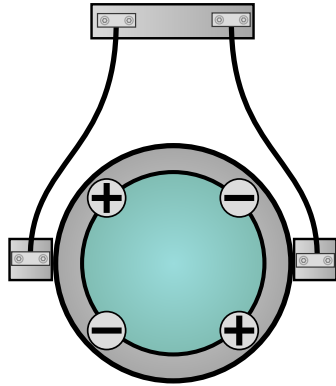


Figure 7-6: Diagram of the Tip Tilt Suspension with thick wires. The thickness of the wires caused them to hang with a curve (the curve is exaggerated in this Figure), which lowered the vertical resonance frequency relative to straight wires. Also shown is the relative polarity of the permanent magnets used for active beam steering control.

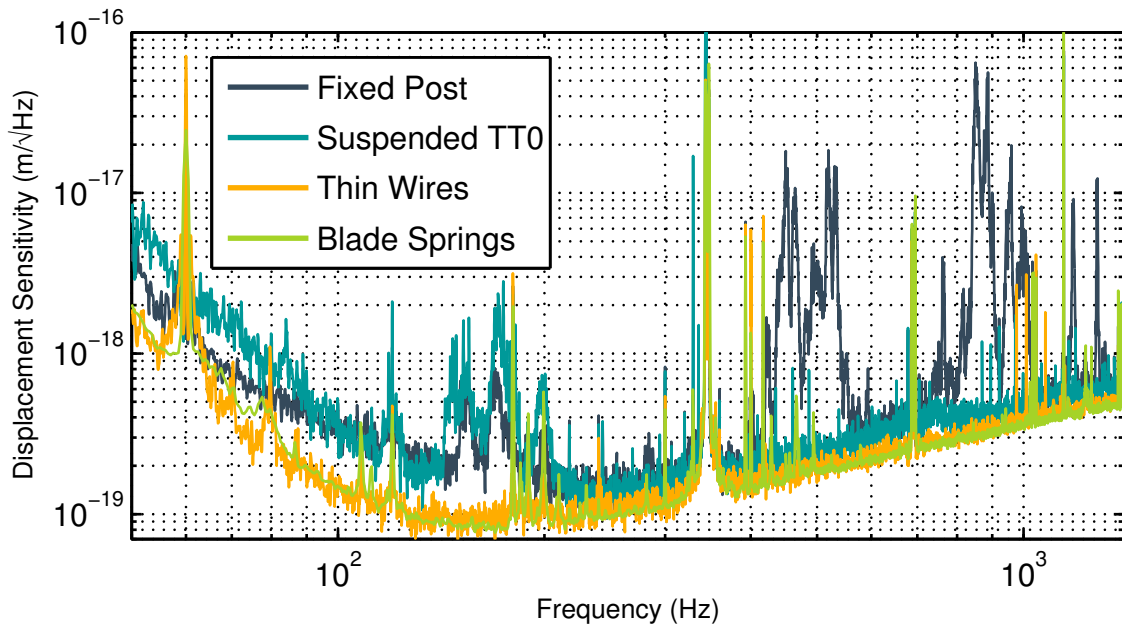


Figure 7-7: Measurement of interferometer sensitivity for different Tip Tilt designs. Changing the configuration of TT0 from a fixed post to a suspended optic removed large features in the 400-1000Hz region, but increased the noise in the 150-200Hz region. Most features were removed when all Tip Tilts were suspended by thin wires. Finally the configuration was changed again to use blade springs due to the fragility of the thin wires, this also removed the vertical resonance of TT1 near 80Hz. Changes in the background noise floor are not due to modifications of the Tip Tilts.

The wires had a diameter of  $380\mu\text{m}$  which was sufficient to cause the break off point of the suspension to be far from the wire clamp. Instead of being straight, the wires took more of an ‘S’ shape, as shown in Figure 7.6. The bend in the wire resulted in giving the wire much more yield, reducing the resonant frequencies and placing them directly in the most sensitive region of LIGO. A finite element analysis of resonances of optics suspended by curved wires was performed by Matt Evans and supported this general theory [74].

The Tip Tilt suspension was first modified by using thinner wires of diameter  $50\mu\text{m}$ . This had the desired effect of reducing the frequency of the bounce resonance to be below the sensitive measurement band [75], but could not function as a permanent solution due to the fragility of the wires.<sup>1</sup> The ultimate solution was to place the upper wire clamps at the ends of blade springs. The new Tip Tilt assembly is shown in Figure 7.4. This reduced the vertical resonances to near 20Hz [76, 77], outside of the sensitive region,<sup>2</sup> but while still allowing the use of wires with enough strength. The sensitivity of the interferometer after this change was made is shown in Figure 7.7. Some amount of high frequency acoustic coupling was re-introduced with the blade springs, likely due to strong passive damping of the vertical eigenmodes with Viton rubber [78], though it was not a limiting noise source.

Mechanical resonances of optic supports in the beam path should stay in the front of the mind of those investigating sources of beam jitter noise. Determining the precise source is certainly helped by having the luxury of an optics table equipped with position sensors and an actuation system.

---

<sup>1</sup>One of the Tip Tilts doubled as a fast beam diverter to protect the OMC photodiodes from the full stored energy of the arm cavities which exits the AS port when the interferometer loses lock. This system would put considerable force on the suspension and after several lock loss cycles, it broke one of the Tip Tilt suspension wires. The wire radius was increased to  $75\mu\text{m}$  until the blade spring design was ready for installation.

<sup>2</sup>The Tip-Tilt will be further redesigned for Advanced LIGO, where 20Hz is expected to be in the sensitive region. This is discussed in Chapter 8.



## 7.3 Magnetic field coupling and feed forward subtraction

Even after the mitigation of mechanical beam jitter on the OMC, there was still significant pollution of the LIGO sensitivity at frequencies surrounding 60Hz. 60Hz is the frequency of the AC power distribution system in the U.S.A. and is a well known source of trouble to those attempting to do precision measurement. It is not terribly troublesome if 60Hz interference into one's device is fairly narrow-band. During Enhanced LIGO commissioning however, the 60Hz line was surrounded by broad sidebands which were inferred to be caused by beam jitter. This was particularly troubling because of the importance of sensitivity to gravitational wave emission from the Crab pulsar, which, if it is a strong emitter, is expected to emit gravitational waves at 59.56Hz [8].

The Tip Tilt suspensions utilized permanent magnets affixed to the optics and coil electromagnets for active beam steering control. The polarities were alternated so that uniform ambient magnetic fields would not cause a force or torque on the optic, as shown in Figure 7-6. Robert Schofield determined that the source of the beam jitter peaks at multiples of 60Hz were in fact due to *gradients* in the ambient magnetic field at those frequencies [79]. He also suggested that the use of a magnetometer sensor outside of the vacuum chamber would provide a signal that could be applied to the Tip Tilt alignment control and cancel the effects of the ambient field [80]. In addition, the strength of the permanent dipole magnets used in the Tip Tilts was reduced.

A magnetometer was installed and a feed forward control system was implemented in the LIGO real time system for digital signal processing. The feed forward system read the digitized 3-axis magnetometer signal, performed filtering, and fed the filtered signal to the Tip Tilt pitch and yaw actuators. A diagram of the system may be seen in Figure 7-8.

To reduce the 60Hz jitter peak, the signal filtering was tuned to minimize the presence of 60Hz motion measured by the OMC QPDs. When correctly tuned, the feed forward system was able to significantly reduce the magnitude of the sidebands

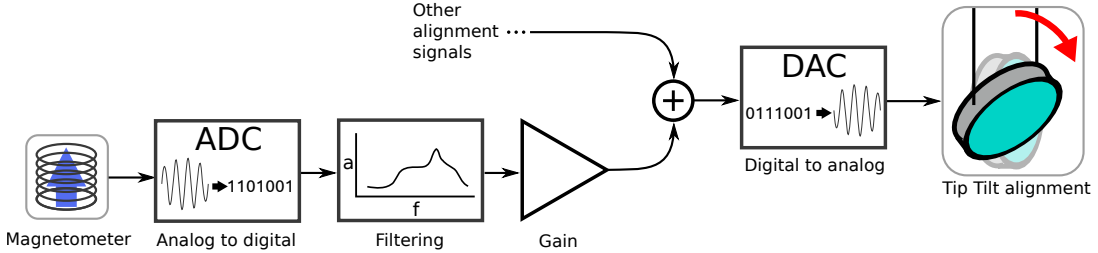


Figure 7-8: Block diagram of the magnetometer feed forward system. The signal read by an analog magnetometer is digitized and filtered. The signal is then combined with other digital alignment signals, converted to analog, and applied to the Tip Tilt alignment actuators.

around 60Hz in the LIGO sensitivity spectrum. The performance of the magnetometer feed forward system is shown in Figure 7-9.

Such a feed forward servo is beneficial whenever one has a signal which is coherent with the source of high frequency jitter noise. Because of the bilinear coupling of beam jitter, removal of even narrow, single frequency, components of beam motion can reduce broadband sources of noise in one's data. With only the magnetometer signal, it would not be possible to perform off-line subtraction of the sidebands around 60Hz from the final data stream. However, it has been shown that it is possible to combine several signals, in a nonlinear way, to subtract sources of bilinear-coupled noise from off-line data [81]. This rather impressive technique has already been shown to be well suited for reduction of beam jitter noise and has truly great potential for future interferometers.

## 7.4 The relationship of alignment control and beam jitter

As discussed in Chapter 5, a standard cavity alignment control system is designed to minimize the  $\text{TEM}_{01}$  and  $\text{TEM}_{10}$  mode content incident on the cavity. We have also just seen that any misalignment increases the linear coupling of beam jitter noise to the cavity transmission signal. This connection is manifestly clear in the case of a dither alignment servo, where beam jitter is purposely induced on the beam,



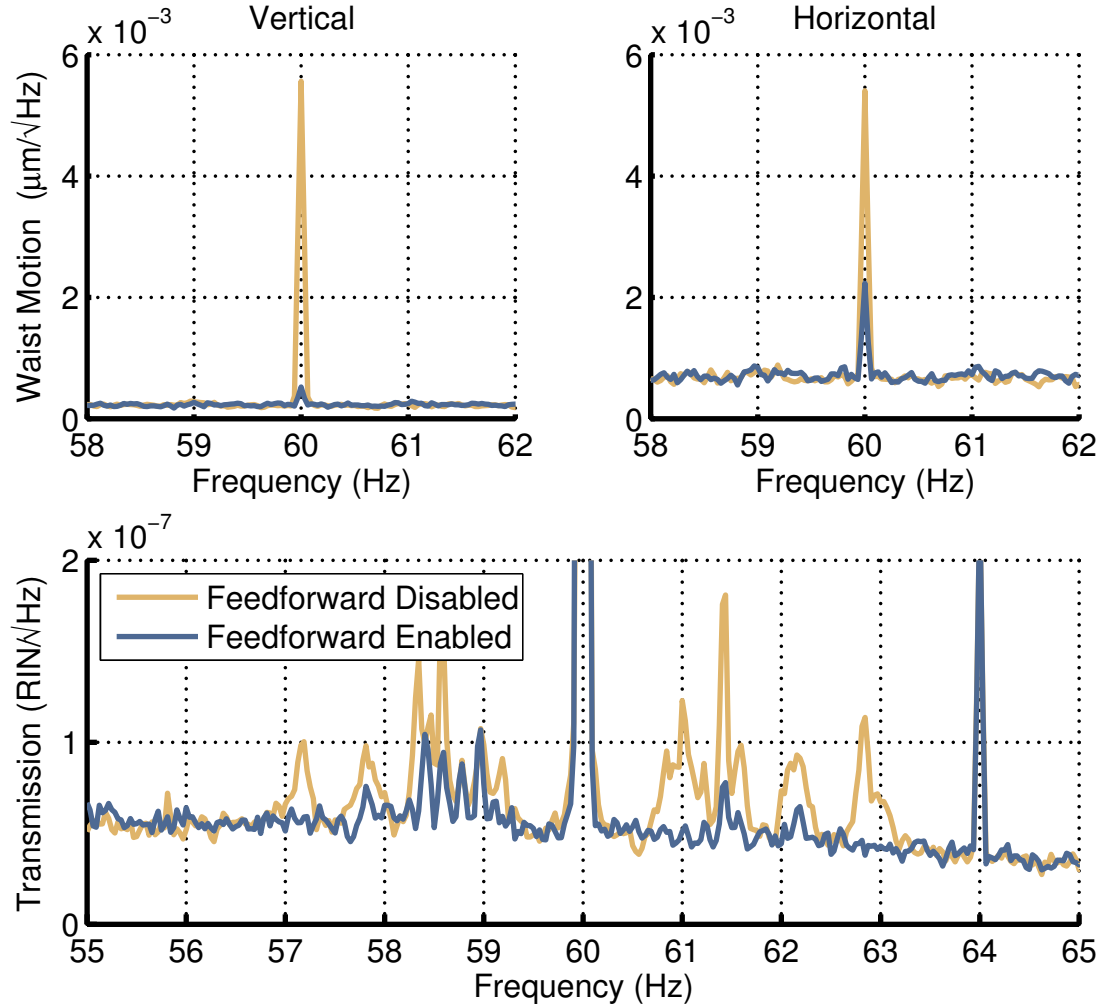


Figure 7-9: Measurement of the performance of the magnetometer feed forward system. The feed forward system was tuned to minimize the beam motion as measured by the OMC quadrant photodetectors (shown in both top panels). The beam jitter reduction leads to a reduction of the highly variable sidebands structures around the 60Hz line.

and the servo obtains optimum alignment by minimizing the coupling of the dither frequency in transmission. If the DC and low frequencies of the alignment error can be sufficiently suppressed by a control system, the beam jitter coupling is consequently reduced.

We break this relationship between alignment optimization and jitter coupling minimization when a beacon or optimal style alignment system is used as described in Section 5.2. Because the carrier frequency component is often the dominant contribution to the total power of the transmitted signal, it is usually the case that beam jitter noise originating from the carrier is dominant over other frequency components. Alignment schemes which optimize the alignment of the audio frequency signal sidebands will disregard the HOM content of the carrier beam, and thus may increase beam jitter coupling. This additional beam jitter coupling may be mitigated by control of the relative modal content of the audio sidebands and the carrier, which will be discussed in the following section.

## 7.5 Modification of the relative modal content of the carrier and audio sidebands<sup>3</sup>

After the implementation of the beacon alignment system in Enhanced LIGO, some beam jitter peaks of unknown origin remained in the sensitive region of the detector. It was discovered that the height of these peaks were controllable by modifying the beam position on the antisymmetric port alignment sensor<sup>4</sup> of the main interferometer alignment control system. We postulated that because of offsets in the readout of the interferometer alignment signals, changing the beam position would change the error point offsets of the alignment feedback system of the main interferometer. The antisymmetric port signal primarily feeds back to the differential alignment mode of the ETMs. It was thought that this led to a redistribution of the modal content of

---

<sup>3</sup>This section will satisfy as merely a record of some lore learned during Enhanced LIGO. It is not intended to provide a quantitative model, but merely act as a guide for future efforts.

<sup>4</sup>In Initial/Enhanced LIGO, this was known as WFS1.



the carrier field exiting the antisymmetric port of the interferometer relative to the fields of the audio sidebands. One could imagine that the position of a local minimum, with respect to alignment, of the carrier transmission could be moved into coincidence with the optimal alignment point of the signal fields. Attempts were made to instead directly inject offsets into the alignment error signals to produce the same effect, but they were never as successful as varying the pointing on the alignment sensor.

# Chapter 8

## Conclusion

The beginning of the second generation of large scale interferometric gravitational wave antennae has begun. A number of new interferometers are currently in various stages of construction. Advanced LIGO in the United States [82], with possibly a third site in India [83], Advanced Virgo in Italy [84], GEO-HF in Germany [85], and KAGRA in Japan [86], will comprise a worldwide network of detectors with sensitivity expected to yield several gravitational wave signals of astrophysical origin per year [5]. Achieving the maximum possible sensitivity of these detectors promises to increase the frequency of the detection of signals, and an improvement of the quality of science that can be done with them. Each one of these future detectors will employ an output mode cleaner and stands to benefit from the techniques described in this thesis. Indeed, this benefit will only increase as squeezed light injection becomes common practice among these detectors.

Many of the difficulties experienced with the output mode cleaner in Enhanced LIGO are already being addressed. Changes to the design of the OMC for Advanced LIGO include using a long range PZT for length actuation, eliminating the need for the thermal length actuator (OTAS) and removing the associated issues with small beam clearance in the cavity and thermal dependence of the cavity  $g$ -parameter [87, 88]. Also, the tombstones themselves will be polished and coated to act as the input and output couplers, without the need of separate optic to be bonded.

The modal content of the output beam of an interferometer is typically very



difficult to model, though there are reasons to believe that the amount of junk light in Advanced LIGO will be reduced compared to Enhanced LIGO. Advanced LIGO will employ stable power recycling and signal extraction cavities, so higher order modes will be suppressed [45]. For any junk light that remains, an optimal alignment scheme such as the one described in Chapter 5 will allow maximum signal transmission through the OMC.

Enhanced LIGO further cemented the importance of beam jitter noise when using an OMC. Advanced LIGO will employ much advanced seismic isolation platforms [89] and suspension systems [90] for the main interferometer test mass optics compared to Enhanced LIGO. This will lead to much reduced low frequency beam motion, and consequently its contribution to beam jitter noise. In addition, the Tip Tilts have been completely redesigned to employ blade springs from the outset, as well as to have longer suspension wires, increasing vibration isolation. In any case, commissioners of Advanced LIGO should expect beam jitter to rear its head sooner or later, and be prepared with the tools to combat it (for example, those described in Chapter 7).

One of the largest sources of output loss for the H1 interferometer in Enhanced LIGO was mode matching [40]. The use of a mode matching servo (as described in Chapter 6) to optimize the signal transmission will minimize such losses in future interferometers.

After most of the primal human needs have been met, after a person has shelter, food, and love, there is one need which will be difficult to ever fully satisfy. This is the need to understand, to understand oneself, to understand the Universe and one's place therein. Just as carpenters build shelter and farmers provide food, scientists must provide for that need of people to understand. Every theory and discovery may not feed the popular need to understand, but once in a while, a simple idea can vastly alter the state of human understanding. All materials found on Earth are the product of approximately 90 unique ingredients. Every living creature is related to every other in a single family tree. The Universe as we know it had a beginning, and it occurred around 14 billion years ago. These ideas, while shockingly profound, fit inside of a fortune cookie. They are the product of countless hours of tedium, missteps, insight,

and glory on the part of scientists. The author believes that gravitational wave astronomy, while currently in its pre-infancy, will eventually provide such new lessons and discoveries. Looking deep into space, one sees a huge wall of fire, which occurred hundreds of thousands of years after the Big Bang, through which no photon may pass unscathed. To see deeper, we will need a new messenger. Gravitational waves show promise to be our messengers, and this author is honored to be a part of the early efforts to finally grasp these elusive vibrations of space and time.





# Appendix A

## Practical calculations using matrices based on the optical vector space model

### A.1 Collapsing a tensor of several indices into a 2D matrix

The tensors in the full optical vector space model described in Chapter 4 are tensors with elements that are referenced with up to eight indices. Dealing with eight-dimensional tensors using typical mathematical software environments, such as MATLAB or Mathematica, may be possible, however a far more simple task would be to re-index the tensors into two dimensional matrices which are more easily dealt with.

For example, we want to take the elements of the free space propagator  $P$  in Equation 4.11, and reduce the number of indices.

$$\langle mn; r; p | P | kl; s; q \rangle = P_{mnrpklsq} \Rightarrow P_{ij}. \quad (\text{A.1})$$

Thus we need some function that takes four indices and produces a single collapsed



index, and there must be a one-to-one mapping of  $klsq$  to  $i$  such that a given collapsed index unambiguously determines the element in the original vector space. The result of such an exercise is to produce a formula similar to Equation 6 in Sigg and Mavalvala [56], but we will cover some details here, as well as point out an error in their formula!

One prescription for traversing the modal space is to cover the  $m + n$  orders sequentially. Starting with the  $\text{TEM}_{00}$  mode, then the  $\text{TEM}_{01}$  and  $\text{TEM}_{10}$  modes, then  $\text{TEM}_{02}$ ,  $\text{TEM}_{11}$ , and  $\text{TEM}_{20}$ , etc. One way to do this is to define a collapsed index as

$$g = (m + n)(m + n + 1)/2 + n.$$

This leads to an index that counts diagonally through the modal indices like so:

		$m$		
		0	1	2
$n$	0	0	1	3
	1	2	4	
	2	5		

$\left. \right\} g$

For the frequency index,  $r$ , one is usually concerned with symmetric upper and lower spaced sidebands where the frequency separations of paired sidebands from the carrier are given by  $\omega_{-r} = -\omega_r$  and the index traverses the range  $-(n_f - 1)/2 \leq r \leq (n_f - 1)/2$ , where  $n_f$  is the number of frequency components. The carrier is given by  $\omega_0 = 0$ . From  $r$ , we may construct an index with only positive values as follows

$$a = \begin{cases} r, & \text{if } r \geq 0, \\ r + n_f, & \text{if } r < 0. \end{cases}$$

This definition of  $a$  starts at the carrier at  $r = 0$ , then traverses the positive sidebands, before moving through the negative sidebands in reverse.

One may collapse the modal and frequency indices in the following way

$$i = \hat{a}g + a, \quad (\text{A.2})$$

where  $\hat{a}$  is the number of possible values of  $a$ , which is, in this case, the same as  $n_f$ . This collapsed index behaves in the following way for values of  $g$  and  $a$

$g$	0		1			
$a$	0	1	2	0	1	2
i	0	1	2	3	4	5

In the preceding case,  $n_f = \hat{a} = 3$ . As one can see, each increment of the value of  $g$  shifts the  $a$  index and allows it to start counting again.

The polarization index,  $p$  may be included in the same way, adding another layer of shifting to the other indices. There are only 2 polarization components, so  $\hat{p} = 2$ . And we will let  $p \in \{0, 1\}$  for the two polarization states. The total collapsed index is then

$$i = \hat{p}(\hat{a}g + a) + p = 2n_f \left[ \frac{(m+n)(m+n+1)}{2} + n \right] + 2a + p. \quad (\text{A.3})$$

This is very close to Equation 6 in Sigg and Mavalvala, though the reference is missing a factor of 2 on the  $a$  index. If one would rather choose to ignore the polarization index, Equation A.2 may be used instead.

As a final note on collapsed indices we will note that the translation of the tensor product operation in the eight dimensional representation is represented by a *Kronecker product* of matrices in the collapsed matrix space. For example, ignoring the polarization space, the three operations

$$\mathbf{G} = \mathbf{G}_{\text{modal}} \otimes \mathbf{G}_{\text{frequency}}$$

$$G_{mnkls} = G_{mnkl} \times G_{rs}$$

$$G_{ij} = \text{Kron}(G_{g_1 g_2}, G_{a_1 a_2})$$

all represent the sample tensor multiplication operation, in the abstract tensor space, in the six index component representation, and in the collapsed index matrix representation, respectively.  $\text{Kron}(\cdot, \cdot)$  is the Kronecker product, and  $i, g_1, a_1$  and  $j, g_2, a_2$  are related as in Equation A.2.



## A.2 Avoid decimal arithmetic bugs

The frequency mixing delta function in the demodulation operator, Equation 4.13, takes the difference of two frequencies and compares that to another frequency. In a numerical calculation, this can lead to bugs when the frequency values cannot be exactly represented as a binary number. To avoid this, one may allow the delta function to take the value 1 when the frequencies being compared are closer than some threshold.

## A.3 Define the free space propagator to have no phase rotation for the TEM<sub>00</sub> carrier.

It is usually desired that when modeling resonant cavities, the default behavior in the steady state is for the carrier frequency component of the laser to be resonant in the cavity. In the real world of cavities and lasers, this resonance condition requires a very careful tuning of the length of the cavity, usually in the form of a control system. In the modeled world, however, we may take a convenient shortcut to ensure that the carrier light is resonant by default in any cavity we construct.

The free space propagator operator (Equation 4.11) contains a phase rotation common to all components of the field. If one were to remove this phase rotation by construction, by letting  $\exp[i(\eta - \omega_0 \Delta z/c)] = 1$ , this would maintain the correct relative phase rotation of all the other components relative to the carrier, without rotating the carrier. In a sense this defines the ‘microscopic phase’ to be zero, and thus the TEM<sub>00</sub> carrier component is always resonant in cavities. One may still model detunings of the carrier from resonance by defining a microscopic propagator which applies the correct detuning phase to the carrier.

## A.4 Units

It is useful to choose a set of units where  $\epsilon_0 c / 2 = 1$ . This essentially chooses the field components to have units of  $\text{W}^{\frac{1}{2}}$ . This simplifies the use of Equation 4.18.

## A.5 Calculating signal to noise ratios

In the language of the vector space model, the shot noise of a full plane photodetector is

$$N = \sqrt{2\hbar\omega_0 \langle E|E \rangle}, \quad (\text{A.4})$$

where  $\omega_0$  is the absolute optical angular frequency of the carrier.

In the case of a split detector the situation is the same. As long as the pupil function is  $-1$  or  $1$  everywhere on the beam, the noise contributes incoherently and with equal weight everywhere, giving again Equation A.4. The situation of the noise for any generic pupil function is left as an exercise for the motivated reader.





# Appendix B

## Additional notes

### B.1 The control vector separation for alignment is the Gouy phase separation

A servo system which is designed to control several degrees of freedom of a system simultaneously must be able to effectively sense and control each degree of freedom independently. The degrees of freedom of the system define a phase space, and the sensors and actuators can be represented as vectors in this space. Where the components of the vectors have amplitudes proportional to the sensitivity of the sensor, or the actuation strength of the actuator, in a given degree of freedom. In order to effectively control one's system, care should be taken to ensure that these vectors sufficiently span the phase space. If any direction does not have coverage, it will either be unsensed, or uncontrolled.

In the case of the alignment of a laser beam, there are four degrees of freedom. These may be parametrized as the beam waist position and beam waist angle in the  $x$  and  $y$  directions.<sup>1</sup> For good alignment control of a laser beam using steering mirrors, for example into an optical cavity, a common piece of lore is that one must have a steering mirror ‘close’ to the alignment target, and one steering mirror ‘far’ from it. But just what exactly sets the criteria for close and far?

---

<sup>1</sup>Where  $z$  is the direction of propagation.



Let us constrain ourselves to a single plane of beam alignment, such that we are only concerned with the waist position and angle in the  $x$  direction. It can be shown that the field of the beam can be represented as the TEM<sub>00</sub> field with some small additional TEM<sub>01</sub> field added when the displacements and misalignments are small [57]. To first order in misalignment, the field can be written as

$$|E\rangle = |00\rangle + \left( \frac{\delta x}{w_0} + i \frac{\theta}{\theta_d} \right) |01\rangle \quad (\text{B.1})$$

where  $|mn\rangle$  is the TEM <sub>$mn$</sub>  eigenmode,  $\delta x$  is the beam position displacement,  $w_0$  is the beam waist radius,  $\theta$  is the beam tilt angle, and  $\theta_d = \lambda/(\pi w_0)$  is the divergence angle. Therefore we may frame the problem of controlling the beam position and angle by our ability to control the real and imaginary quadratures of the amplitude of the TEM<sub>01</sub> component. Thus a ‘good’ alignment system will be one in which the ability of the system to actuate on the real and imaginary quadratures of the TEM<sub>01</sub> field is well separated.

We will represent our alignment system as two steering mirrors labeled A and B. The beam first reflects from mirror A, travels some distance, then reflects from mirror B. We will consider a vector space of the TEM<sub>00</sub> and TEM<sub>01</sub> modes as basis vectors. From Equation 4.9 we see that, in this representation, the operator for mirror A is

$$\mathbf{M}_A \doteq \begin{bmatrix} 1 & -2i\Theta_A \\ -2i\Theta_A & 1 \end{bmatrix} \quad (\text{B.2})$$

where  $\Theta_A$  is the alignment angle of mirror A. A similar expression holds for mirror B.

Between mirrors A and B, we allow the laser to propagate some distance. Along with the propagation phase which is common to all modes, the TEM<sub>01</sub> mode experiences the additional Gouy phase  $\eta$ . The propagation operator is

$$\mathbf{P} \doteq e^{i\phi} \begin{bmatrix} 1 & 0 \\ 0 & e^{i\eta} \end{bmatrix} \quad (\text{B.3})$$

where  $\phi$  is the overall phase common to all modes.

To first order in angles and ignoring the overall phase, the operator of the entire alignment system is

$$\mathbf{M}_B \mathbf{P} \mathbf{M}_A \doteq \begin{bmatrix} 1 & -2i(\Theta_A + e^{i\eta}\Theta_B) \\ -2i(e^{i\eta}\Theta_A + \Theta_B) & e^{i\eta} \end{bmatrix}. \quad (\text{B.4})$$

If we apply this to a pure TEM<sub>00</sub> field on the input, the output field is

$$|E\rangle_{\text{out}} = |00\rangle - 2i(e^{i\eta}\Theta_A + \Theta_B)|01\rangle. \quad (\text{B.5})$$

Comparing this to Equation B.1, we see that mirror B actuates exclusively on the beam angle, while for mirror A, the amount of position or angle actuation depends on the Gouy phase propagation between the two mirrors,  $\eta$ . If  $\eta = \pi/2$ , then mirror A only actuates on position and the two actuators are completely separated in actuator phase space. In fact, the angle between the actuators in phase space is just  $\eta$ .

Intuitively, this may be understood by the fact that the TEM<sub>01</sub> mode has an extra rotation relative to the TEM<sub>00</sub> mode, this is the Gouy phase. Once one of the mirrors has actuated on the beam, we must let the quadrature that was actuated on rotate away so that we may actuate on the perpendicular quadrature. This rotation is what causes angles in the near field to rotate into positions in the far field.

The treatment of sensing is quite similar, in that case, it is the demodulation operator (Equation 4.16) which connects the TEM<sub>00</sub> and TEM<sub>01</sub> modes, and again, the Gouy phase dictates the sensor separation.

As a final thought, if one were designing an actuation system for modes of higher order than TEM<sub>01</sub>, the propagation operator matrix element for a TEM<sub>*mn*</sub> mode would be  $e^{(m+n)\eta}$ . This would cause the optimal control separation (a phase space angle of  $\pi/2$ ) to occur at  $\eta = \frac{1}{m+n}\frac{\pi}{2}$ . Thus, mode matching sensors and actuators, which operate on  $m + n = 2$  modes, must have  $\eta = \pi/4$  separation for optimal performance.



## B.2 Dither sensing is a measurement of a partial derivative

Suppose one has a sensor which measures some physical quantity  $P$ , which depends on a variable  $\theta$  which is controllable by some means of actuation. A modulation is injected into the variable  $\theta$  such that

$$\theta = \theta_0 + \alpha \sin[\omega t], \quad (\text{B.6})$$

where  $\alpha \ll 1$  is the modulation depth, and  $\omega$  is the modulation frequency. The resulting behavior of  $P$  is

$$P(\theta) = P(\theta_0 + \alpha \sin[\omega t]) \approx P(\theta_0) + \frac{\partial P}{\partial \theta}(\theta_0) \alpha \sin[\omega t] + \dots \quad (\text{B.7})$$

Thus the amplitude of the  $\omega$  frequency component, which can be determined by demodulation, is proportional to the partial derivative of the measured quantity with respect to the controlled variable. This is the basic mechanism behind dither sensing.

## B.3 Conventions for the coefficient of amplitude transmission and reflectivity of beamsplitters

Imagine a beam with complex electric field amplitude  $E_0$  striking a partially reflective boundary. The beam will be split into two resultant beams, a transmitted beam and reflected. Define the transmitted beam as a complex coefficient,  $t$ , multiplied by the incident beam. Similarly, the reflected beam will be multiplied by  $r$ . This is shown in Figure B-1a. Note: we make no assumption about the value of these coefficients. At all times we will ignore phase shifts due simply to propagation, so the  $ik\delta z$  phase is always divided out.

Imagine the time reversed process of the two resultant beams. In the phasor space of the electric field, time reversal requires the complex conjugation operation. The

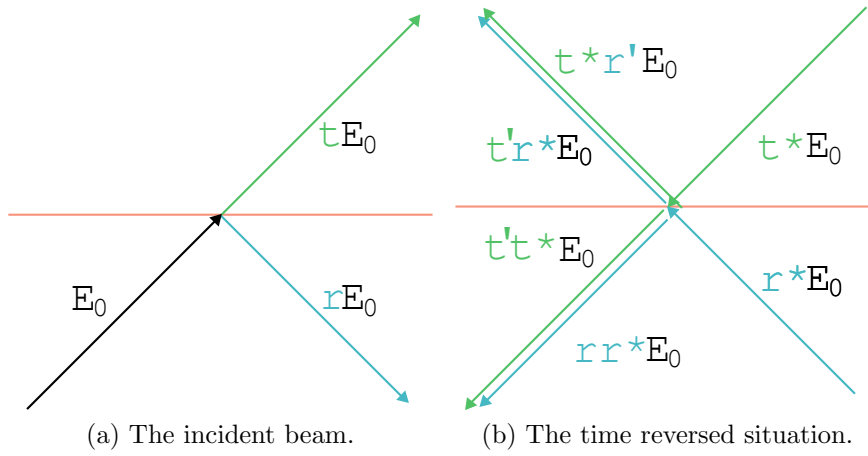


Figure B-1: Diagram of the interaction of a beam with a beamsplitter.

blue beam will be split into two beams for which we will use the same coefficients of transmission and reflection as in the case already considered, because it interacts with the boundary from the same direction. However, we will assume that the green beam, which is hitting the boundary from the other side, has different coefficients,  $t'$  and  $r'$ . This situation is shown in Figure B-1b.

Now, we make the assumption that this process obeys the principle of time reversal symmetry.<sup>2</sup> Thus the result of the second case should match the initial conditions of the first case. The two beams above the boundary should interfere destructively, while the two below should reproduce the original input beam. This gives us two equations.

$$rr^* + t't^* = 1,$$

$$t'r^* + r't^* = 0.$$

Solving for  $t$  gives

$$t = -ie^{i\phi/2}\sqrt{1 - |r|^2}, \quad (\text{B.8})$$

where  $e^{i\phi} \equiv r'/r^*$ . The two most common conventions choose  $r$  to be real and  $\phi$  to either be  $\pi$ , leading to the  $r = -r'$  with  $t$  real convention, or  $2\pi$ , leading to the  $r = r'$

---

<sup>2</sup>This also implicitly assumes there are no losses.



with  $t = i\tau$  for  $\tau$  real convention.

## B.4 A resonant cavity as a mode cleaner

This section will attempt to illuminate just how a resonant cavity can be used to ‘clean’ the mode of a laser beam.

Chapter 14 of Siegman [33] explains the mathematical peculiarities of defining resonant eigenmodes for open optical cavities like the OMC. For the sake of this discussion we will assume that, for a given cavity, one may define an orthonormal set of resonant eigenmodes. Being eigenmodes, they have the property that after one round trip in the cavity, the transverse profile of the mode is unchanged. There may be an overall scaling due to losses, and some overall phase shift which may be mode-dependent.

For cavities that use spherical mirrors, these modes are nearly the TEM modes of free space propagation, characterized by a beam waist size and position, defined by the cavity geometry.

The modes experience a phase shift due to propagation in addition to the standard  $\exp(-ikz)$  phase shift of a plane wave. If we chose the Hermite-Gaussian mode basis, the  $\text{TEM}_{mn}$  mode experiences a phase shift of  $\exp(i\eta(z)[1+m+n])$ .  $\eta(z)$  is the Gouy phase shift and is defined as

$$\eta(z) = \arctan\left(\frac{2[z - z_0]}{kw_0^2}\right), \quad (\text{B.9})$$

where  $z_0$  is the position of the beam waist,  $k$  is the wavenumber, and  $w_0$  is the beam waist radius.

A mode cleaner is a critically coupled cavity. This gives the cavity the attribute light which is centered on resonance is maximally transmitted. Perfect impedance matching ensures that no light is reflected. Light which is far from resonance (separated from resonance by many times the linewidth) is maximally reflected. Very little is transmitted, though it is not zero, for a lossless cavity with finesse  $\mathcal{F}$  at perfect

anti-resonance, the transmission is  $1/(1 + 4\mathcal{F}^2/\pi^2)$ .

The total Gouy phase shift after one cavity round trip  $\eta_{rt}$  is given by Equation 3.2. Resonance of a mode occurs when the total phase accumulated, the plane wave phase and the Gouy phase, in a round trip is a multiple of  $2\pi$ . For the TEM<sub>00</sub> mode, this is when  $\exp(i[\eta_{rt} - kp]) = 1$  (for a cavity with perimeter  $p$ ). Relative to the TEM<sub>00</sub> mode, resonance of the TEM <sub>$m n$</sub>  mode occurs when the plane wave phase shift cancels the relative Gouy phase shift, or  $\Delta(kp) = [m + n]\eta(z)$ . In terms of a frequency shift, this gives Equation 3.4. For a HOM with frequency shift  $\Delta f$ , coincidence resonance occurs when  $\Delta f$  is close to a multiple of the FSR (within a few cavity linewidths).

The mode cleaner is controlled to hold a desired mode on resonance (usually the TEM<sub>00</sub> mode), while the frequency shifts of the HOMs keep them far from resonance. In most cases the amplitude of the HOMs decreases with increasing order. There will always be coincident resonances for sufficiently high order modes, thus one must design the mode cleaner (based on knowledge of the input beam) such that the coincident modes are of sufficiently small amplitude so as not to cause problems.

Thus a mode cleaner may be used to maximally transmit the TEM<sub>00</sub> mode, while reflecting modes of higher orders.

## B.5 The second order HOMs

Various higher order modes are often visualized in terms of the intensity profile of a given pure mode. This can be useful in conveying how the intensity of different modes are distributed. Another useful way to visualize the modes is to consider the perturbation of the TEM<sub>00</sub> mode when a new mode is added. In the case of alignment, this is useful in showing that the addition of some amount of TEM<sub>01</sub> mode acts to displace the beam horizontally.

Figure B-2 shows the TEM<sub>00</sub> mode along with the three second order modes. The TEM<sub>00</sub> mode is shown in the top left panel. The top right panel shows the bull's-eye mode, or  $\frac{1}{\sqrt{2}}(|20\rangle + |02\rangle)$ . The lower left panel shows  $\frac{1}{\sqrt{2}}(|20\rangle - |02\rangle)$ , and the lower right panel shows the TEM<sub>11</sub> mode,  $|11\rangle$ .



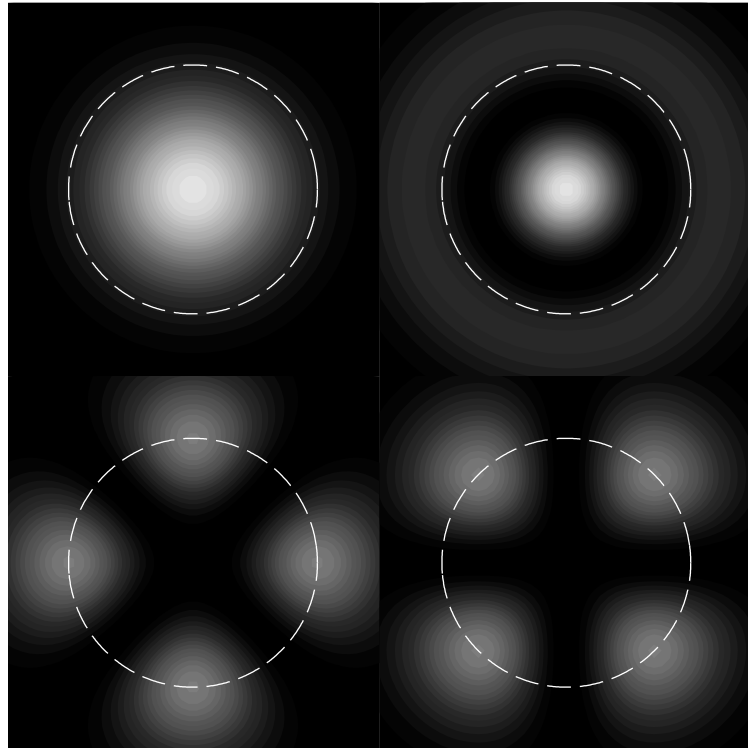


Figure B-2: Transverse intensity profile of the second order modes. The top left panel shows a pure  $\text{TEM}_{00}$  mode. The bull's-eye mode is shown in the top right panel. The lower left panel shows the astigmatic mode along the horizontal and vertical axes. The lower right panel shows the astigmatic mode along the  $45^\circ$  axes. For reference, a dashed circle is drawn to outline the beam width radius of the  $\text{TEM}_{00}$  mode.

Just as the first order modes are responsible for beam misalignments, the second order modes are responsible for mode mismatching. This can be seen by visualizing the change in the intensity profile of a beam when some small amount of second order mode perturbation is added. Figure B-3 shows the effects of the second order modes on a  $\text{TEM}_{00}$  beam. The top left panel is a pure  $\text{TEM}_{00}$  beam, for reference. The top right shows the effect of adding about 20% of the bull's-eye mode in amplitude. The center peak has been suppressed and field has been added to the outer edges of the beam. This causes the beam to spread out and have a larger beam size. The lower panels show the effects of the two astigmatic modes. The  $\frac{1}{\sqrt{2}}(|20\rangle - |02\rangle)$  mode is responsible for astigmatism along the vertical and horizontal axes, while the  $\text{TEM}_{11}$  mode is responsible for astigmatism along the axes rotated by  $45^\circ$ .

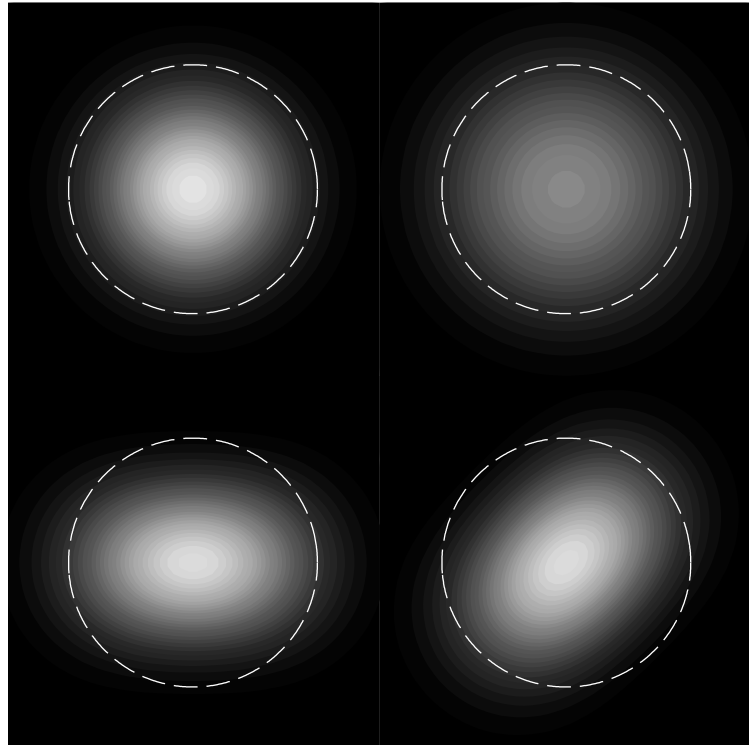


Figure B-3: The effects of second order mode perturbations on the  $\text{TEM}_{00}$  mode. A pure  $\text{TEM}_{00}$  mode is shown in the top left panel. The top right panel shows how the bull's-eye mode alters the beam radius. The two bottom panels show how the astigmatic modes modify the pure beam. For reference, a dashed circle is drawn on all panels at the beam width radius of the pure  $\text{TEM}_{00}$  mode.





# Appendix C

## Common misconceptions about laser interferometer gravitational-wave antennae

### C.1 The sensitivity/bandwidth “trade off”

There is an argument that exists in various places in the literature when considering the response of the Fabry-Perot resonant arm cavities of a gravitational wave antenna. The argument goes something like this:

- When designing an interferometer, one must choose the finesse of the arm cavities.
- An increase in the finesse leads to an increase of stored power in the arms, which increases the sensitivity to gravitational waves.
- The finesse also negatively impacts the bandwidth of the arm cavities. An increase in finesse leads to a reduction in sensitivity to gravitational waves at frequencies higher than the cavity bandwidth.
- Thus there is a trade off between sensitivity and bandwidth, and one must choose the arm cavity finesse to balance the benefits of each.



Noise sources that are frequency independent (white) at the photodetector will have a frequency dependent structure shaped as the inverse of the interferometer optical sensitivity. In other words, as the interferometer sensitivity decreases, the contribution from that noise source to limiting the ultimate measurement correspondingly increases. So sometimes the above argument is given in terms of the shape of the shot noise contribution (which is white at the photodetector) of the interferometer. In that case, the argument might say that an interferometer with a higher finesse will have a lower cavity pole, and hence, the shot noise will begin rising in frequency earlier, ultimately leading to a higher noise floor at high frequencies.

The flaw in the argument arises when one actually compares the effects of the two competing contributions to the interferometer sensitivity. This is well illustrated by considering the shot noise floor of a Michelson Interferometer with Fabry Perot arms (FPMI). The amplitude spectral density of shot noise of this interferometer, calibrated as referred to the strain measured by the interferometer is [30]

$$h_{\text{shot}}^{\text{FPMI}} = \sqrt{\frac{\pi\hbar\lambda}{cP_{\text{BS}}}} \left( \frac{\sqrt{1 + (4\pi\tau f)^2}}{4\pi\tau} \right) = h_{\text{shot}}^{\text{MI}} \times \frac{\pi\sqrt{1 + (4\mathcal{F})^2(f/\text{FSR})^2}}{2\mathcal{F}}, \quad (\text{C.1})$$

where  $\hbar$  is the reduced Planck constant,  $\lambda$  is the laser wavelength,  $c$  is the speed of light,  $P_{\text{BS}}$  is the light incident on the beam splitter,  $\tau = \frac{\mathcal{F}}{\pi\text{FSR}}$  is the light storage time of the arm cavities, FSR is the cavity free spectral range, and  $\mathcal{F}$  is the cavity finesse. The second equality shows the shot noise scaled by the shot noise in a Michelson interferometer with no cavity arms. Equation C.1 shows how the behavior of the sensitivity of the interferometer depends on the cavity finesse. The low frequency sensitivity is indeed improved with an increased finesse, the shot noise decreases. However at high frequencies, where  $f \gg \text{FSR}/4\mathcal{F}$ , the effect of the finesse cancels out, and an increase in finesse does not reduce the sensitivity of the interferometer. Figure C-1 shows how the shot noise sensitivity changes as a result of changing the arm cavity finesse. As one can see, the high frequency sensitivities are all the same. So there is no trade-off, an increase in finesse can only benefit the sensitivity, at least

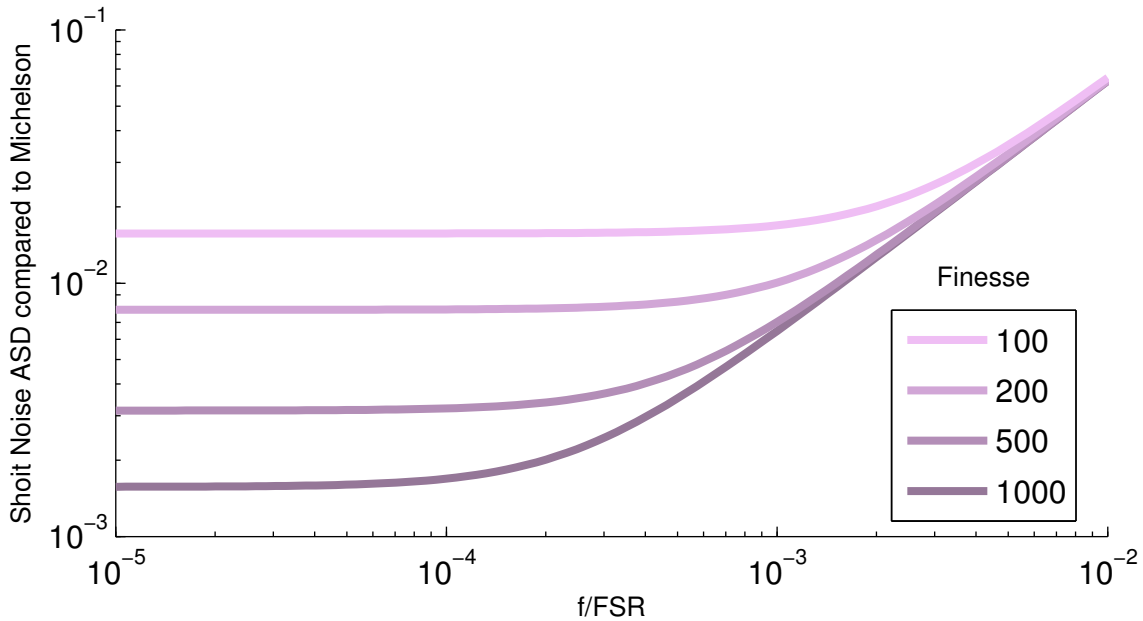


Figure C-1: The dependence of shot noise on cavity finesse of a Fabry-Perot Michelson interferometer. The shot noise is given as an amplitude spectral density scaled to the shot noise of an equivalent Michelson interferometer with no arm cavities.

in this simplified case.<sup>1</sup>

In reality, there are good reasons to limit the finesse of the arm cavities. These include difficulty of lock acquisition, the ability to deal with very large amounts of stored power in the arm, and the fact that the loss experienced in one round trip through the arm is multiplied by the number of bounces the light experiences.

The choice of the arm cavity finesse for a FPMI is usually driven by the existence of other noise sources. The finesse can be increased until other, low frequency, noise sources dominate and there is no benefit to increase the finesse further.

In the case of a FPMI, the finesse governs both the stored arm power and the bandwidth of the differential mode interferometer, or the recycling of the gravitational wave audio sidebands. The addition of a signal recycling/extraction mirror, as in Advanced LIGO, breaks this symmetry. The signal mirror can be used to modify the detector bandwidth, without changing the stored arm cavity power.

---

<sup>1</sup>This no longer is true, for example, when losses are included.



The author is not certain about where this misconception comes from. For example, it is treated correctly in the classic reference by Saulson [14]. On page 103, about the high frequency regime, he writes, “Further increase in the finesse of the arm cavities neither helps, nor in this simple case hurts, the sensitivity.”

## C.2 Why LIGO has two arms

This misconception is alluded to in Section 2.5, but is treated here more directly. People who are knowledgeable about LIGO, but are not familiar with the details of the interferometer are often surprised to learn that the main reasons driving the use of a Michelson interferometer are related to the coupling of technical noise sources, and not because of the fact that gravitational waves stretch along perpendicular axes.

A Michelson interferometer with symmetric arms bestows the experimentalist with the powerful gift of *common mode noise rejection*. Technical fluctuations of the laser amplitude and frequency tend to reflect back to the laser, not to the dark fringe of the Michelson. The added benefit of the common mode servo (Section 2.6) also can be used to reduce the laser frequency noise. Again, this is treated beautifully in Sections 10.1.4 and 12.6 of Saulson [14].

A two-armed interferometer is a significant increase in complexity, though the sensitivity benefit is mainly only a larger coverage of the sky. It is the massive reduction of noise that makes the complexity worthwhile.

## C.3 With a DARM offset, is LIGO still a null measurement?

This is not a misconception *per se*, but is an interesting point that deserves a small bit of discussion.

Saulson provides a thorough discussion about what makes an experiment ‘null’ [14, Chapter 10]. He concludes that a Michelson interferometer for gravitational wave detection is not exactly a null measurement. This is because the experimental-

ists *do* expect to detect a signal. However, he does conclude that all the virtues of null instruments do exist for a LIGO-like interferometer. The fact that the interferometer is operated on a dark fringe leads to rejection of laser noises. Additionally, the measurement is ‘chopped’ due to the phase modulation sidebands and subsequent demodulation, which move the signal away from sources of low frequency measurement noise.

As discussed in Section 2.9, Enhanced LIGO employed DC readout, as will Advanced LIGO. This technique places a small offset in the arms of the interferometer, and the measurement is not chopped, it is done at DC. What does this mean for the status of LIGO? Will it be out of the null club?

In the most simple sense, LIGO is no longer a null measurement. It is measuring small changes in the DC value of some quantity. The relative intensity noise of the carrier exiting the dark port is on the order of  $10^{-7}/\sqrt{\text{Hz}}$  at the frequencies of interest. It is no longer a chopped measurement, the laser noise must be low at audio frequencies, not only RF frequencies.

The fact is that DC readout remains very close to a dark fringe. The fractional offset is on the order of  $10^{-5}$ , only 10pm out of a wavelength of  $1\mu\text{m}$ . So most of the common mode laser noise rejection remains. Though it is the intrinsically low laser noise of modern solid state lasers that really makes DC readout possible.

However, there is a sense in which LIGO still is a null measurement. LIGO does not aim to measure static changes in the metric tensor. The Michelson interferometer, as first designed by Michelson, was looking for DC changes in the light propagation times in the two arms.<sup>2</sup> This is not true for LIGO. LIGO is looking for time dependent variations in light propagation times. The majority of the time that data are taken will be in the absence of waves of sufficient size to cause a signal. Thus the expected value, at the measurement frequencies, is still zero. So even with an offset, LIGO is not in the business of measuring a non-zero value, and checking if that is the expected value. In a sense it is measuring a value many times and seeing if the value has changed over time.

---

<sup>2</sup>Though they could modulate their signal, by rotating their interferometer.





# Abbreviation Glossary

AOM	Acousto-optic modulator
AS	Antisymmetric (port)
BPD	Bull's-eye photodetector
BS	Beamsplitter
CARM	Common arm length degree of freedom
CCD	Charge coupled device
DARM	Differential arm length degree of freedom
DC	Direct-current, for a readout scheme it is not demodulated, by contrast to an RF readout scheme
EOM	Electro-optic modulator
ETM	End test mass
FPMI	Michelson interferometer with Fabry-Perot arm cavities
FSR	Free spectral range, the separation in length or frequency between resonances of a cavity
FWHM	Full peak width at half maximum
GEO600	The 600m German-British Gravitational wave detector
GW	Gravitational wave
H1	The 4km LIGO Interferometer at Hanford



HAM	Horizontal access module, one of the two standard LIGO vacuum chamber types
HOM	Higher order mode, i.e. modes of order higher than the $\text{TEM}_{00}$ mode
HR	Highly reflective, mirror coating or mirror
HWP	Half wave plate
ISI	Internal seismic isolation system
ITM	Input test mass
KAGRA	The Kamioka Cryogenic Gravitational wave Telescope in Japan
LED	Light emitting diode
LIGO	Laser Interferometer Gravitational-wave Observatory
MI	Michelson interferometer
MICH	Michelson length degree of freedom
Nd:YAG	Neodymium-doped yttrium aluminium garnet, a common gain medium for 1064nm solid state lasers
OC	Over-coupled, an over-coupled cavity
OMC	Output mode cleaner
OTAS	OMC thermal actuator system
PBS	Polarizing beam splitter
PD	Photodetector, or photodiode
PDH	The Pound-Drever-Hall cavity reflection locking technique
PO	Pick-off (port)
PRC	Power recycling cavity length degree of freedom
PRM	Power recycling mirror
PZT	Lead zirconate titanate, a common piezoelectric material

QPD	Quadrant photodetector
QWP	Quarter wave plate
REFL	Reflection (port)
RIN	Relative intensity noise, fractional change in intensity
TDM	Thermally deformable mirror
TEM	Transverse electro-magnetic mode
ULE	Ultra Low Expansion glass
Virgo	The 3km Italian-French Gravitational wave detector
WFS	Wavefront sensor, a heterodyned QPD





# Bibliography

- [1] S.M. Carroll. *Spacetime and geometry: an introduction to general relativity*. Addison Wesley, 2004. ISBN 9780805387322. URL <http://books.google.com/books?id=1SKFQgAACAAJ>.
- [2] B.F. Schutz. *A First Course in General Relativity*. Series in physics. Cambridge University Press, 1985. ISBN 9780521277037. URL <http://books.google.com/books?id=qhDFuWbLlgQC>.
- [3] M Rakhmanov. On the round-trip time for a photon propagating in the field of a plane gravitational wave. *Classical and Quantum Gravity*, 26(15):155010, 2009. doi:[10.1088/0264-9381/26/15/155010](https://doi.org/10.1088/0264-9381/26/15/155010).
- [4] J. H. Taylor, L. A. Fowler, and P. M. McCulloch. Measurements of general relativistic effects in the binary pulsar PSR1913+16. *Nature*, 277(5696):437–440, Feb 1979. doi:[10.1038/277437a0](https://doi.org/10.1038/277437a0).
- [5] J Abadie et al. Predictions for the rates of compact binary coalescences observable by ground-based gravitational-wave detectors. *Classical and Quantum Gravity*, 27(17):173001, 2010. doi:[10.1088/0264-9381/27/17/173001](https://doi.org/10.1088/0264-9381/27/17/173001).
- [6] J. Abadie et al. Search for gravitational waves from compact binary coalescence in LIGO and Virgo data from S5 and VSR1. *Phys. Rev. D*, 82:102001, Nov 2010. doi:[10.1103/PhysRevD.82.102001](https://doi.org/10.1103/PhysRevD.82.102001).
- [7] J. Abadie et al. Search for gravitational waves from binary black hole inspiral, merger, and ringdown. *Phys. Rev. D*, 83:122005, Jun 2011. doi:[10.1103/PhysRevD.83.122005](https://doi.org/10.1103/PhysRevD.83.122005).
- [8] B. Abbott et al. Beating the spin-down limit on gravitational wave emission from the Crab pulsar. *The Astrophysical Journal Letters*, 683(1):L45, 2008. doi:[10.1086/591526](https://doi.org/10.1086/591526).
- [9] J. Abadie et al. Beating the spin-down limit on gravitational wave emission from the Vela pulsar. *The Astrophysical Journal*, 737(2):93, 2011. doi:[10.1088/0004-637X/737/2/93](https://doi.org/10.1088/0004-637X/737/2/93).
- [10] J. Abadie et al. All-sky search for gravitational-wave bursts in the first joint ligo-geo-virgo run. *Phys. Rev. D*, 81:102001, May 2010. doi:[10.1103/PhysRevD.81.102001](https://doi.org/10.1103/PhysRevD.81.102001).

- [11] The LIGO Scientific Collaboration and The Virgo Collaboration. An upper limit on the stochastic gravitational-wave background of cosmological origin. *Nature*, 460(7258):990–994, Aug 2009. ISSN 0028-0836. doi:[10.1038/nature08278](https://doi.org/10.1038/nature08278).
- [12] J. Abadie et al. Directional limits on persistent gravitational waves using LIGO S5 science data. *Phys. Rev. Lett.*, 107:271102, Dec 2011. doi:[10.1103/PhysRevLett.107.271102](https://doi.org/10.1103/PhysRevLett.107.271102).
- [13] William Press. On gravitational conductors, waveguides, and circuits. *General Relativity and Gravitation*, 11:105–109, 1979. ISSN 0001-7701. doi:[10.1007/BF00756582](https://doi.org/10.1007/BF00756582).
- [14] P.R. Saulson. *Fundamentals of Interferometric Gravitational Wave Detectors*. World Scientific, 1994. ISBN 9789810218201. URL <http://books.google.com/books?id=4JyGQgAACAAJ>.
- [15] Rana Adhikari. *Sensitivity and noise analysis of 4 km laser interferometric gravitational wave antennae*. PhD thesis, Massachusetts Institute of Technology, July 2004. URL <http://dspace.mit.edu/handle/1721.1/28646>.
- [16] Stefan W. Ballmer. *LIGO interferometer operating at design sensitivity with application to gravitational radiometry*. PhD thesis, Massachusetts Institute of Technology, May 2006. URL <http://dspace.mit.edu/handle/1721.1/36396>.
- [17] Tobin T. Fricke. *Homodyne Detection for Laser-Interferometric Gravitational Wave Detectors*. PhD thesis, Louisiana State University, October 2011. URL <http://etd.lsu.edu/docs/available/etd-11082011-115541/>.
- [18] Katherine L. Dooley. *Design and Performance of High Laser Power Interferometers for Gravitational-wave Detection*. PhD thesis, University of Florida, December 2011. URL <https://dcc.ligo.org/cgi-bin/DocDB>ShowDocument?docid=P1100125>.
- [19] Jeffrey S. Kissel. *Calibrating and Improving the Sensitivity of the LIGO Detectors*. PhD thesis, Louisiana State University, September 2010. URL <http://etd.lsu.edu/docs/available/etd-09122010-101812/>.
- [20] J. Weber. Detection and generation of gravitational waves. *Phys. Rev.*, 117: 306–313, Jan 1960. doi:[10.1103/PhysRev.117.306](https://doi.org/10.1103/PhysRev.117.306).
- [21] James L. Levine and Richard L. Garwin. New negative result for gravitational wave detection, and comparison with reported detection. *Phys. Rev. Lett.*, 33: 794–797, Sep 1974. doi:[10.1103/PhysRevLett.33.794](https://doi.org/10.1103/PhysRevLett.33.794).
- [22] J. A. Tyson. Null search for bursts of gravitational radiation. *Phys. Rev. Lett.*, 31:326–329, Jul 1973. doi:[10.1103/PhysRevLett.31.326](https://doi.org/10.1103/PhysRevLett.31.326).
- [23] J. Weber. Evidence for discovery of gravitational radiation. *Phys. Rev. Lett.*, 22: 1320–1324, Jun 1969. doi:[10.1103/PhysRevLett.22.1320](https://doi.org/10.1103/PhysRevLett.22.1320).

- [24] C. W. Misner, R. A. Breuer, D. R. Brill, P. L. Chrzanowski, H. G. Hughes, and C. M. Pereira. Gravitational synchrotron radiation in the schwarzschild geometry. *Phys. Rev. Lett.*, 28:998–1001, Apr 1972. doi:[10.1103/PhysRevLett.28.998](https://doi.org/10.1103/PhysRevLett.28.998).
- [25] G. W. Gibbons and S. W. Hawking. Theory of the detection of short bursts of gravitational radiation. *Phys. Rev. D*, 4:2191–2197, Oct 1971. doi:[10.1103/PhysRevD.4.2191](https://doi.org/10.1103/PhysRevD.4.2191).
- [26] A. Morse, W. O. Hamilton, W. W. Johnson, E. Mauceli, and M. P. McHugh. Calibration and sensitivity of resonant-mass gravitational wave detectors. *Phys. Rev. D*, 59:062002, Feb 1999. doi:[10.1103/PhysRevD.59.062002](https://doi.org/10.1103/PhysRevD.59.062002).
- [27] F. A. E. Pirani. On the physical significance of the Riemann tensor. *Acta. Phys. Polon.*, 15, 1956.
- [28] G. E. Moss, L. R. Miller, and R. L. Forward. Photon-noise-limited laser transducer for gravitational antenna. *Appl. Opt.*, 10(11):2495–2498, Nov 1971. doi:[10.1364/AO.10.002495](https://doi.org/10.1364/AO.10.002495).
- [29] Rainer Weiss. Electromagnetically coupled broadband gravitational antenna, Apr 1972. Quarterly Progress Report 105, Research Laboratory of Electronics, MIT.
- [30] The LIGO Scientific Collaboration. LIGO: the laser interferometer gravitational-wave observatory. *Rep. Prog. Phys.*, 72(7):076901, 2009. doi:[10.1088/0034-4885/72/7/076901](https://doi.org/10.1088/0034-4885/72/7/076901).
- [31] H Grote and The LIGO Scientific Collaboration. The GEO 600 status. *Classical Quant. Grav.*, 27(8):084003, 2010. doi:[10.1088/0264-9381/27/8/084003](https://doi.org/10.1088/0264-9381/27/8/084003).
- [32] The Virgo Collaboration. Virgo status. *Classical Quant. Grav.*, 25(18):184001, 2008. doi:[10.1088/0264-9381/25/18/184001](https://doi.org/10.1088/0264-9381/25/18/184001).
- [33] A.E. Siegman. *Lasers*. University Science Books, 1986. ISBN 9780935702118. URL <http://books.google.com/books?id=1BZVwUZLTkAC>.
- [34] R. W. P. Drever, J. L. Hall, F. V. Kowalski, J. Hough, G. M. Ford, A. J. Munley, and H. Ward. Laser phase and frequency stabilization using an optical resonator. *Applied Physics B: Lasers and Optics*, 31:97–105, 1983. ISSN 0946-2171. doi:[10.1007/BF00702605](https://doi.org/10.1007/BF00702605).
- [35] Malik Rakhmanov. *Dynamics of Laser Interferometric Gravitational Wave Detectors*. PhD thesis, California Institute of Technology, May 2000. URL <http://www.ligo.caltech.edu/docs/P/P000002-00.pdf>.
- [36] Peter Fritschel, Rolf Bork, Gabriela González, Nergis Mavalvala, Dale Ouiette, Haisheng Rong, Daniel Sigg, and Michael Zucker. Readout and control of a power-recycled interferometric gravitational-wave antenna. *Appl. Opt.*, 40(28):4988–4998, Oct 2001. doi:[10.1364/AO.40.004988](https://doi.org/10.1364/AO.40.004988).

- [37] Guido Mueller, Rich Abbott, Lisa Barsotti, Matthew Evans, Stefan Ballmer, Valery Frolov, Peter Fritschel, and Rana Adhikari. Advanced LIGO Length Sensing and Control Final Design. Technical Report T1000298, LIGO Laboratory, Jun 2010. URL <https://dcc.ligo.org/cgi-bin/DocDB>ShowDocument?docid=12213>.
- [38] S Hild, H Grote, J Degallaix, S Chelkowski, K Danzmann, A Freise, M Hewitson, J Hough, H Lck, M Prijatelj, K A Strain, J R Smith, and B Willke. DC-readout of a signal-recycled gravitational wave detector. *Classical and Quantum Gravity*, 26(5):055012, 2009. doi:[10.1088/0264-9381/26/5/055012](https://doi.org/10.1088/0264-9381/26/5/055012).
- [39] R L Ward, R Adhikari, B Abbott, R Abbott, D Barron, R Bork, T Fricke, V Frolov, J Heefner, A Ivanov, O Miyakawa, K McKenzie, B Slagmolen, M Smith, R Taylor, S Vass, S Waldman, and A Weinstein. DC readout experiment at the Caltech 40m prototype interferometer. *Classical and Quantum Gravity*, 25(11):114030, 2008. doi:[10.1088/0264-9381/25/11/114030](https://doi.org/10.1088/0264-9381/25/11/114030).
- [40] Tobin T. Fricke, Nicolás D. Smith-Lefebvre, Richard Abbott, Rana Adhikari, Katherine L. Dooley, Matthew Evans, Peter Fritschel, Valery V. Frolov, Keita Kawabe, Jeffrey S. Kissel, Bram J. J. Slagmolen, and Sam J. Waldman. DC readout experiment in Enhanced LIGO. *Classical and Quantum Gravity*, 29(6):065005, 2012. doi:[10.1088/0264-9381/29/6/065005](https://doi.org/10.1088/0264-9381/29/6/065005).
- [41] J. Gea-Banacloche and G. Leuchs. Squeezed states for interferometric gravitational-wave detectors. *Journal of Modern Optics*, 34(6-7):793–811, 1987. doi:[10.1080/09500348714550751](https://doi.org/10.1080/09500348714550751).
- [42] Simon Chelkowski, Henning Vahlbruch, Karsten Danzmann, and Roman Schnabel. Coherent control of broadband vacuum squeezing. *Phys. Rev. A*, 75:043814, Apr 2007. doi:[10.1103/PhysRevA.75.043814](https://doi.org/10.1103/PhysRevA.75.043814).
- [43] Sam Waldman, Peter Fritschel, and Rana Adhikari. Enhanced LIGO. Technical Report T060156, LIGO Laboratory, Nov 2009. URL <https://dcc.ligo.org/cgi-bin/DocDB>ShowDocument?docid=7384>.
- [44] Keita Kawabe. Design and Performance of the Output Mode Cleaner. Technical Report G040326, LIGO Laboratory, Aug 2004. URL <https://dcc.ligo.org/cgi-bin/DocDB>ShowDocument?docid=35413>.
- [45] Guido Mueller, Muzammil Arain, Hiro Yamamoto, and Peter Fritschel. Stable Recycling Cavities for Advanced LIGO. Technical Report T080208, LIGO Laboratory, Jun 2009. URL <https://dcc.ligo.org/cgi-bin/DocDB>ShowDocument?docid=2692>.
- [46] Sam Waldman. The Enhanced LIGO Output Mode Cleaners. Technical Report T080144, LIGO Laboratory, Sep 2009. URL <https://dcc.ligo.org/cgi-bin/DocDB>ShowDocument?docid=5416>.

- [47] Bram Slagmolen, Adam Mullavy, Rana Adhikari, and David McClelland. Tip-Tilt Mirror Specifications and Design. Technical Report T0900096, LIGO Laboratory, Mar 2009. URL <https://dcc.ligo.org/cgi-bin/DocDB>ShowDocument?docid=1029>.
- [48] N. Uehara and K. Ueda. Accurate measurement of the radius of curvature of a concave mirror and the power dependence in a high-finesse fabry—perot interferometer. *Appl. Opt.*, 34(25):5611–5619, Sep 1995. doi:[10.1364/AO.34.005611](https://doi.org/10.1364/AO.34.005611).
- [49] Matt Evans. LIGO Hanford Electronic Log, Jan 2009. URL [http://ilog.ligo-wa.caltech.edu/ilog/pub/ilog.cgi?group=detector&date\\_to\\_view=01/23/2009&anchor\\_to\\_scroll\\_to=2009:01:23:00:57:22-mevans](http://ilog.ligo-wa.caltech.edu/ilog/pub/ilog.cgi?group=detector&date_to_view=01/23/2009&anchor_to_scroll_to=2009:01:23:00:57:22-mevans).
- [50] Sam Waldman and Sheon Chua. eLIGO Hanford Output Mode Cleaner Repair. Technical Report T1100562, LIGO Laboratory, Nov 2011. URL <https://dcc.ligo.org/cgi-bin/DocDB>ShowDocument?docid=75471>.
- [51] Thomas Corbitt, Christopher Wipf, Timothy Bodiya, David Ottaway, Daniel Sigg, Nicolas Smith, Stanley Whitcomb, and Nergis Mavalvala. Optical dilution and feedback cooling of a gram-scale oscillator to 6.9 mk. *Phys. Rev. Lett.*, 99: 160801, Oct 2007. doi:[10.1103/PhysRevLett.99.160801](https://doi.org/10.1103/PhysRevLett.99.160801).
- [52] The LIGO Scientific Collaboration. A gravitational wave observatory operating beyond the quantum shot-noise limit. *Nature Physics*, 7(12):962–965, 2011. doi:[10.1038/nphys2083](https://doi.org/10.1038/nphys2083).
- [53] The LIGO Scientific Collaboration. Enhancement of the astrophysical reach of a gravitational wave observatory using squeezed states of light. in preparation.
- [54] Jean-Yves Vinet. Recycling interferometric antennas for periodic gravitational waves. *J. Phys. France*, 47(4):639–643, 1986. doi:[10.1051/jphys:01986004704063900](https://doi.org/10.1051/jphys:01986004704063900).
- [55] Yaron Hefetz, Nergis Mavalvala, and Daniel Sigg. Principles of calculating alignment signals in complex resonant optical interferometers. *J. Opt. Soc. Am. B*, 14(7):1597–1605, Jul 1997. doi:[10.1364/JOSAB.14.001597](https://doi.org/10.1364/JOSAB.14.001597).
- [56] Daniel Sigg and Nergis Mavalvala. Principles of calculating the dynamical response of misaligned complex resonant optical interferometers. *J. Opt. Soc. Am. A*, 17(9):1642–1649, Sep 2000. doi:[10.1364/JOSAA.17.001642](https://doi.org/10.1364/JOSAA.17.001642).
- [57] Dana Z. Anderson. Alignment of resonant optical cavities. *Appl. Opt.*, 23(17): 2944–2949, Sep 1984. doi:[10.1364/AO.23.002944](https://doi.org/10.1364/AO.23.002944).
- [58] K. Kawabe, N. Mio, and K. Tsubono. Automatic alignment-control system for a suspended fabry—perot cavity. *Appl. Opt.*, 33(24):5498–5505, Aug 1994. doi:[10.1364/AO.33.005498](https://doi.org/10.1364/AO.33.005498).

- [59] Matt Evans. LIGO Hanford Electronic Log, Nov 2011. URL [http://ilog.ligo-wa.caltech.edu/ilog/pub/ilog.cgi?group=detector&date\\_to\\_view=11/29/2011&anchor\\_to\\_scroll\\_to=2011:11:29:19:56:59-mevans](http://ilog.ligo-wa.caltech.edu/ilog/pub/ilog.cgi?group=detector&date_to_view=11/29/2011&anchor_to_scroll_to=2011:11:29:19:56:59-mevans).
- [60] W. Winkler, K. Danzmann, A. Rüdiger, and R. Schilling. Heating by optical absorption and the performance of interferometric gravitational-wave detectors. *Phys. Rev. A*, 44:7022–7036, Dec 1991. doi:[10.1103/PhysRevA.44.7022](https://doi.org/10.1103/PhysRevA.44.7022).
- [61] Ryan Lawrence, Michael Zucker, Peter Fritschel, Phil Marfuta, and David Shoemaker. Adaptive thermal compensation of test masses in advanced ligo. *Classical and Quantum Gravity*, 19(7):1803, 2002. doi:[10.1088/0264-9381/19/7/377](https://doi.org/10.1088/0264-9381/19/7/377).
- [62] Muzammil A. Arain, William Z. Korth, Luke F. Williams, Rodica M. Martin, Guido Mueller, D. B. Tanner, and David H. Reitze. Adaptive control of modal properties of optical beams using photothermal effects. *Opt. Express*, 18(3):2767–2781, Feb 2010. doi:[10.1364/OE.18.002767](https://doi.org/10.1364/OE.18.002767).
- [63] Y. Fan, C. Zhao, J. Degallaix, L. Ju, D. G. Blair, B. J. J. Slagmolen, D. J. Hosken, A. F. Brooks, P. J. Veitch, and J. Munch. Feedback control of thermal lensing in a high optical power cavity. *Review of Scientific Instruments*, 79(10):104501, 2008. doi:[10.1063/1.2982239](https://doi.org/10.1063/1.2982239).
- [64] Guido Mueller, Qi ze Shu, Rana Adhikari, D. B. Tanner, David Reitze, Daniel Sigg, Nergis Mavalvala, and Jordan Camp. Determination and optimization of mode matching into optical cavities by heterodyne detection. *Opt. Lett.*, 25(4):266–268, Feb 2000. doi:[10.1364/OL.25.000266](https://doi.org/10.1364/OL.25.000266).
- [65] Katherine Dooley. LLO OMC mode matching. Technical Report T0900508, LIGO Laboratory, October 2009. URL <https://dcc.ligo.org/cgi-bin/DocDB/ShowDocument?docid=6493>.
- [66] Patrick Kwee, Frank Seifert, Benno Willke, and Karsten Danzmann. Laser beam quality and pointing measurement with an optical resonator. *Review of Scientific Instruments*, 78(7):073103, 2007. doi:[10.1063/1.2754400](https://doi.org/10.1063/1.2754400).
- [67] Daniel Sigg. Modal Model Update 4 - Mode Mismatch. Technical Report T960116, LIGO Laboratory, Jul 1996. URL <https://dcc.ligo.org/cgi-bin/DocDB/ShowDocument?docid=28699>.
- [68] N. Smith-Lefebvre, S. Ballmer, M. Evans, S. Waldman, K. Kawabe, V. Frolov, and N. Mavalvala. Optimal alignment sensing of a readout mode cleaner cavity. *Opt. Lett.*, 36(22):4365–4367, Nov 2011. doi:[10.1364/OL.36.004365](https://doi.org/10.1364/OL.36.004365).
- [69] B Canuel, R Day, E Genin, P La Penna, and J Marque. Wavefront aberration compensation with a thermally deformable mirror. *Classical and Quantum Gravity*, 29(8):085012, 2012. doi:[10.1088/0264-9381/29/8/085012](https://doi.org/10.1088/0264-9381/29/8/085012).

- [70] Seiji Kawamura and Michael E. Zucker. Mirror-orientation noise in a fabry-perot interferometer gravitational wave detector. *Appl. Opt.*, 33(18):3912–3918, Jun 1994. doi:[10.1364/AO.33.003912](https://doi.org/10.1364/AO.33.003912).
- [71] Robert Schofield. LIGO Hanford Electronic Log, Jun 2009. URL [http://ilog.ligo-wa.caltech.edu/ilog/pub/ilog.cgi?group=detector&date\\_to\\_view=06/05/2009&anchor\\_to\\_scroll\\_to=2009:06:05:22:21:44-robert](http://ilog.ligo-wa.caltech.edu/ilog/pub/ilog.cgi?group=detector&date_to_view=06/05/2009&anchor_to_scroll_to=2009:06:05:22:21:44-robert).
- [72] Robert Schofield. LIGO Hanford Electronic Log, Jan 2009. URL [http://ilog.ligo-wa.caltech.edu/ilog/pub/ilog.cgi?group=detector&date\\_to\\_view=01/17/2009&anchor\\_to\\_scroll\\_to=2009:01:17:16:23:51-robert](http://ilog.ligo-wa.caltech.edu/ilog/pub/ilog.cgi?group=detector&date_to_view=01/17/2009&anchor_to_scroll_to=2009:01:17:16:23:51-robert).
- [73] Nicolas Smith. LIGO Hanford Electronic Log, Apr 2009. URL [http://ilog.ligo-wa.caltech.edu/ilog/pub/ilog.cgi?group=detector&date\\_to\\_view=04/28/2009&anchor\\_to\\_scroll\\_to=2009:04:28:12:15:36-nicolas](http://ilog.ligo-wa.caltech.edu/ilog/pub/ilog.cgi?group=detector&date_to_view=04/28/2009&anchor_to_scroll_to=2009:04:28:12:15:36-nicolas).
- [74] Matt Evans. LIGO Hanford Electronic Log, Apr 2009. URL [http://ilog.ligo-wa.caltech.edu/ilog/pub/ilog.cgi?group=detector&date\\_to\\_view=04/30/2009&anchor\\_to\\_scroll\\_to=2009:04:30:12:14:59-mevans](http://ilog.ligo-wa.caltech.edu/ilog/pub/ilog.cgi?group=detector&date_to_view=04/30/2009&anchor_to_scroll_to=2009:04:30:12:14:59-mevans).
- [75] Nicolas Smith. LIGO Hanford Electronic Log, May 2009. URL [http://ilog.ligo-wa.caltech.edu/ilog/pub/ilog.cgi?group=detector&date\\_to\\_view=05/26/2009&anchor\\_to\\_scroll\\_to=2009:05:26:20:06:14-nicolas](http://ilog.ligo-wa.caltech.edu/ilog/pub/ilog.cgi?group=detector&date_to_view=05/26/2009&anchor_to_scroll_to=2009:05:26:20:06:14-nicolas).
- [76] Koji Arai. LIGO Livingston Electronic Log, Sep 2009. URL [http://ilog.ligo-la.caltech.edu/ilog/pub/ilog.cgi?group=detector&date\\_to\\_view=09/04/2009&anchor\\_to\\_scroll\\_to=2009:09:04:11:05:07-arai](http://ilog.ligo-la.caltech.edu/ilog/pub/ilog.cgi?group=detector&date_to_view=09/04/2009&anchor_to_scroll_to=2009:09:04:11:05:07-arai).
- [77] David Yeaton-Massey. LIGO Hanford Electronic Log, Sep 2009. URL [http://ilog.ligo-wa.caltech.edu/ilog/pub/ilog.cgi?group=detector&date\\_to\\_view=09/06/2009&anchor\\_to\\_scroll\\_to=2009:09:08:09:45:09-dmass](http://ilog.ligo-wa.caltech.edu/ilog/pub/ilog.cgi?group=detector&date_to_view=09/06/2009&anchor_to_scroll_to=2009:09:08:09:45:09-dmass).
- [78] Robert Schofield. Environmental noise - related lessons from S6. Technical Report G1100330, LIGO Laboratory, Mar 2011. URL <https://dcc.ligo.org/cgi-bin/DocDB>ShowDocument?docid=40083>.
- [79] Robert Schofield. LIGO Hanford Electronic Log, Sep 2009. URL [http://ilog.ligo-wa.caltech.edu/ilog/pub/ilog.cgi?group=detector&date\\_to\\_view=09/06/2009&anchor\\_to\\_scroll\\_to=2009:09:06:10:49:13-robert](http://ilog.ligo-wa.caltech.edu/ilog/pub/ilog.cgi?group=detector&date_to_view=09/06/2009&anchor_to_scroll_to=2009:09:06:10:49:13-robert).
- [80] Robert Schofield. LIGO Hanford Electronic Log, Jul 2009. URL [http://ilog.ligo-wa.caltech.edu/ilog/pub/ilog.cgi?group=detector&date\\_to\\_view=07/10/2009&anchor\\_to\\_scroll\\_to=2009:07:10:01:08:20-robert](http://ilog.ligo-wa.caltech.edu/ilog/pub/ilog.cgi?group=detector&date_to_view=07/10/2009&anchor_to_scroll_to=2009:07:10:01:08:20-robert).
- [81] Sergei Klimenko. Regression of environmental noise in gravitational-wave detectors. Technical Report G1200462, LIGO Laboratory, Apr 2012. URL <https://dcc.ligo.org/cgi-bin/DocDB>ShowDocument?docid=90579>.

- [82] Gregory M Harry and the LIGO Scientific Collaboration. Advanced LIGO: the next generation of gravitational wave detectors. *Classical and Quantum Gravity*, 27(8):084006, 2010. doi:[10.1088/0264-9381/27/8/084006](https://doi.org/10.1088/0264-9381/27/8/084006).
- [83] Bala Iyer, Tarun Souradeep, CS Unnikrishnan, Sanjeev Dhurandhar, Sendhil Raja, and Anand Sengupta. LIGO-India, Proposal of the Consortium for Indian Initiative in Gravitational-wave Observations (IndIGO),[Public]. Technical Report M1100296, LIGO Laboratory, Nov 2011. URL <https://dcc.ligo.org/cgi-bin/DocDB>ShowDocument?docid=75988>.
- [84] The Virgo Collaboration. Advanced Virgo baseline design. Technical Report VIR027A09, Virgo Project, May 2009. URL <https://tds.ego-gw.it/ql/?c=6589>.
- [85] B Willke, P Ajith, B Allen, P Aufmuth, C Aulbert, S Babak, R Balasubramanian, B W Barr, S Berukoff, A Bunkowski, G Cagnoli, C A Cantley, M M Casey, S Chelkowski, Y Chen, D Churches, T Cokelaer, C N Colacino, D R M Crooks, C Cutler, K Danzmann, R J Dupuis, E Elliffe, C Fallnich, A Franzen, A Freise, I Gholami, S Goler, A Grant, H Grote, S Grunewald, J Harms, B Hage, G Heinzel, I S Heng, A Hepstonstall, M Heurs, M Hewitson, S Hild, J Hough, Y Itoh, G Jones, R Jones, S H Huttner, K Ktter, B Krishnan, P Kwee, H Lück, M Luna, B Machenschalk, M Malec, R A Mercer, T Meier, C Messenger, S Mohanty, K Mossavi, S Mukherjee, P Murray, G P Newton, M A Papa, M Perreurl-Lloyd, M Pitkin, M V Plissi, R Prix, V Quetschke, V Re, T Regimbau, H Rehbein, S Reid, L Ribichini, D I Robertson, N A Robertson, C Robinson, J D Romano, S Rowan, A Rüdiger, B S Sathyaprakash, R Schilling, R Schnabel, B F Schutz, F Seifert, A M Sintes, J R Smith, P H Sneddon, K A Strain, I Taylor, R Taylor, A Thüring, C Ungarelli, H Vahlbruch, A Vecchio, J Veitch, H Ward, U Weiland, H Welling, L Wen, P Williams, W Winkler, G Woan, and R Zhu. The GEO-HF project. *Classical and Quantum Gravity*, 23(8):S207, 2006. doi:[10.1088/0264-9381/23/8/S26](https://doi.org/10.1088/0264-9381/23/8/S26).
- [86] K Kuroda and the LCGT Collaboration. Status of LCGT. *Classical and Quantum Gravity*, 27(8):084004, 2010. doi:[10.1088/0264-9381/27/8/084004](https://doi.org/10.1088/0264-9381/27/8/084004).
- [87] Sam Waldman. Output Mode Cleaner Design. Technical Report T1000276, LIGO Laboratory, May 2010. URL <https://dcc.ligo.org/cgi-bin/DocDB>ShowDocument?docid=T1000276>.
- [88] Sam Waldman. Proposed changes for the Advanced LIGO Output Mode Cleaner. Technical Report T0900157, LIGO Laboratory, Apr 2009. URL <https://dcc.ligo.org/cgi-bin/DocDB>ShowDocument?docid=1702>.
- [89] R Abbott, R Adhikari, G Allen, S Cowley, E Daw, D DeBra, J Giaime, G Hammond, M Hammond, C Hardham, J How, W Hua, W Johnson, B Lantz, K Mason, R Mittleman, J Nichol, S Richman, J Rollins, D Shoemaker, G Stapef, and R Stebbins. Seismic isolation for Advanced LIGO. *Classical and Quantum Gravity*, 19(7):1591, 2002. doi:[10.1088/0264-9381/19/7/349](https://doi.org/10.1088/0264-9381/19/7/349).

- [90] N A Robertson, G Cagnoli, D R M Crooks, E Elliffe, J E Faller, P Fritschel, S Goler, A Grant, A Heptonstall, J Hough, H Lck, R Mittleman, M Perreurd-Lloyd, M V Plissi, S Rowan, D H Shoemaker, P H Sneddon, K A Strain, C I Torrie, H Ward, and P Willems. Quadruple suspension design for Advanced LIGO. *Classical and Quantum Gravity*, 19(15):4043, 2002. doi:[10.1088/0264-9381/19/15/311](https://doi.org/10.1088/0264-9381/19/15/311).